Spin-Orbit Coupling in Functionalized Graphene

Dissertation

zur Erlangung des Doktorgrades
der Naturwissenschaften (Dr. rer. nat.)
der Fakultät Physik
der Universität Regensburg

vorgelegt von

Tobias Völkl

aus Weiden i.d.Opf.

im Jahr 2020

Promotionsgesuch eingereicht am 07.07.2020

Die Arbeit wurde angeleitet von PD Dr. Jonathan Eroms und Prof. Dr. Dieter Weiss

Prüfungsausschuss: Vorsitzender: Prof. Dr. Dominique Bougeard
1. Gutachter: PD Dr. Jonathan Eroms
2. Gutachter: Prof. Dr. Jaroslav Fabian
Weiterer Prüfer: Prof. Dr. Jörg Wunderlich

Contents

List of Figures

1 Introduction

The first isolation, identification and characterization of the two dimensional material graphene in 2004 by Geim and Novoselov [1] received much attention. This was subsequently followed by the emergence of two dimensional materials as an active research field [2] and was consequently awarded with the Nobel prize in physics in 2010. However, first investigations of the important characteristics of electron mobility and spin diffusion lengths gave values which were several orders of magnitude lower than what was expected from theoretical predictions.

It was realized that these underwhelming results were due to the influence of the surroundings of the graphene sheets rather than the intrinsic properties of graphene. Indeed, the electron mobility of the earlier graphene devices was shown to be limited by the commonly used SiO_2 substrates [3]. Much higher electron mobilities could later be achieved by suspending graphene [4] or by placing graphene onto the substrate hexagonal boron nitride (hBN) [5]. While in suspended graphene strain alters the graphene properties [6], the lattice structure of hBN can significantly alter the electronic bandstructure of graphene [7].

For transport of spin polarized currents the spin lifetime is likely limited by residual atomic defects, such as attached hydrogen atoms. These defects provide a local magnetic moment as well as localized electronic states, which in combination can randomize electron spins very efficiently [8].

The large influence of the surroundings on the properties of graphene makes it very difficult to reach and investigate the intrinsic, clean state of single or bilayer graphene. However, this dependence can be seen as both a disadvantage as well as an opportunity. One might even compare this situation to the state of semiconductor research in the early 20th century. Here, the large dependence of semiconductor properties on doping resulted in seemingly random differences between almost identical samples [9]. This prompted Wolfgang Pauli to state that “One should not work on semiconductors, that is a filthy mess” [10]. However, control over these doping levels in later years was exactly what lead to the technological breakthrough of semiconductors.

Similarly, in recent years much progress has been made in intentionally altering various electronic properties of graphene by the application of adsorbates or placing graphene in contact with different materials. It has been demonstrated already in 2009 that covalently bonded hydrogen atoms have the potential to alter the electronic bandstructure of graphene and to even induce a bandgap [11], which is a prerequisite for potential use of graphene in transistor applications. Further, functionalization of graphene by covalently bonded fluorine [12–15], physisorbed metallic atoms such as copper [16], indium [17], iridium [18] or gold [18–20], and even intentionally created lattice defects such as vacancies in the graphene lattice [19, 21] have been explored.

More recently it was discovered that various properties can be induced in graphene by bringing graphene into proximity with certain material systems. With this technique, desirable properties of the substrate can be transferred to the graphene sheet [22]. These induced properties include superconductivity [23–25] and ferromagnetic ordering [26–28]. Also, by carefully controlling the relative orientation between the layers in graphene/hBN heterostructures, superlattices with nanometer sized lattice periods can be achieved [7, 29, 30]. Importantly, these effects can be induced while intrinsic properties of graphene, such as the high electron mobility or the possibility to tune the charge carrier concentration by a gate electrode, are preserved.

One aspect of graphene that is particularly intriguing to influence by functionalization is the spin orbit coupling (SOC) strength. This property is a key material parameter for possible spintronic applications, which utilize the spin as a degree of freedom for information storage or logic devices [31, 32]. The SOC-strength in pristine graphene was reported to be comparatively small [33], which in combination with the high electron mobility of graphene allows to transport spin polarized currents over distances as large as 30 µm [34]. Thus, graphene is an ideal material to transport spin encoded information. However, the small SOC-strength prevents functionalities such as the manipulation of the electron spin direction by electronic gates or the generation of spin currents through charge to spin conversion effects. Since these aspects are essential for possible spintronic applications, methods to increase the SOC in graphene are required.

In this thesis, two of these methods are explored. Applying hydrogen atoms to graphene has long been proposed as a method to increase the SOC in graphene [35]. Here, the hydrogen atoms form covalent bonds with the carbon atoms in graphene, which changes the hybridization of the carbon atoms. The corresponding mixing of electronic states from different bands is thus expected to increase the SOC in graphene [36]. Further, in the dilute limit, the addition of the light hydrogen atoms has a much smaller impact on the electronic bandstructure of graphene than heavier adatoms [33]. Experimentally, a drastically increased SOC in hydrogenated graphene indicated by the occurrence of a giant spin-Hall effect, was reported [37]. However, the employed measurement methods leave room for differing interpretation of the measured data and the occurrence of the spin-Hall effect in hydrogenated graphene is still under debate [18, 38, 39].

Alternatively, graphene can be placed in contact with materials with high SOC-strength. Here, the SOC in graphene is increased by a weak hybridization of the electronic states of the carbon atoms with the orbitals from the underlying substrate [40]. Particularly promising is the combination of graphene with transition metal dichalcogenides (TMDs). As graphene, these TMDs are layered van der Waals materials, which can be cleaved into thin layers with atomically smooth surfaces. This allows to fabricate heterostructures of graphene and TMDs with ultraclean interfaces. These heterostructures therefore offer the possibility of high mobility graphene with large induced SOC-strength.

Also, for some of these heterostructures the SOC-strength was predicted to be dependent on an applied electric field, perpendicular to the graphene plane [41]. This allows to tune the induced SOC by electric gates, which might offer a way for the realization of a spin based transistor [41, 42]. In this concept, a spin current is injected into graphene through a ferromagnetic contact and detected after a certain distance by a second ferromagnetic contact. Here, injector and detector are in an antiparallel configuration, which means that in the absence of spin relaxation, no current can pass through the device. However, inducing SOC through an electric gate leads to spin relaxation in the graphene channel and current can flow.

Thesis Outline

In this thesis, charge and spin transport measurements in hydrogenated graphene and various heterostructures containing graphene and the TMD WSe_2 are presented. This is done to characterize the magnitude and type of SOC in these systems. Consequently, the thesis starts with the theoretical background of the crystal structure and electronic bandstructure of single and bilayer graphene in chapter 2. Further, this chapter includes the theoretically predicted characteristics of the SOC for the cases of pristine graphene, hydrogenated graphene and graphene/TMD structures.

In chapter 3 important methods for the characterization of the employed graphene samples are discussed. This includes the basics of charge transport and electric gating in graphene. Also, characteristics of Raman-spectroscopy in graphene are presented, which is an essential tool for the characterization of hydrogenated graphene.

Chapter 4 is devoted to effects that are invoked by SOC, and can consequently be utilized to investigate the SOC in the examined material systems. Thus, the effects of weak localization (WL) and weak antilocalization (WAL) in graphene are examined. This is followed by a discussion of spin transport in graphene, which is influenced by SOC, mediated by various spin relaxation mechanisms. The chapter concludes with a description of the spin-Hall effect (SHE) and previous experimental reports of a possible SHE in hydrogenated graphene.

Chapters 5 and 6 represent the experimental part of the thesis. In chapter 5, SOC-effects in weakly hydrogenated graphene are investigated. To this end, the characterization of a method for hydrogenation of graphene and measurements of the WL effect and the SHE in a Hall-bar configuration are presented. This is followed by results obtained in a device geometry that employs spin selective contacts. These allow measurements of spin transport as well as a direct way to examine the SHE in this system. Then, the chapter concludes with a discussion of the experimental results.

The possibility of proximity induced SOC is examined in chapter 6. Thus, after a brief description of the sample fabrication steps, measurements in three different types of heterostructures containing single or bilayer graphene and WSe_2 are presented. In structures with single or bilayer graphene covered with WSe_2 on a SiO_2 substrate, measurements of the WAL-effect allows to characterize the SOC in these systems. Also, the dependence of the induced SOC on an applied transverse electric in these structures is investigated. This is followed by magnetotransport measurements in bilayer graphene, which is encapsulated with WSe_2 and hBN. Here, the emphasis lies on the limiting factor of the WSe_2 substrate on the electron mobility of the device.

2 Basic Properties of Graphene

In this chapter, basic properties of the materials investigated in this thesis are discussed. The crystal and band structure of single and bilayer graphene are introduced in sections 2.1 and 2.2. Then, characteristics of spin-orbit coupling for the cases of pristine graphene, hydrogenated graphene and heterostructures containing graphene and transition metal dichalcogenides, are discussed in section 2.3.

2.1 Single Layer Graphene

2.1.1 Crystal Structure

Graphene is the two dimensional allotrope of carbon arranged in a hexagonal lattice. The four valence electrons of carbon form the ground state configuration $2\mathrm{s}^2 2\mathrm{p}^2$. However, the energetically higher configuration $2\mathrm{s}^1\mathrm{p}^3$ allows the formation of hybrid orbitals by mixing of the 2s and 2p states. In molecules or solids the subsequent formation of covalent bonds can be sufficient to overcome the excitation energy.

For the case of graphene three of the four valence electrons form sp^2 hybrid orbitals. In order to maximize the overlap of the wave functions (and therefore the binding energy), these electrons form σ-bonds, which are oriented in one plane and are separated by angles of 120 °. As depicted in figure 2.1 (a), the resulting lattice is a hexagonal lattice with a basis containing two carbon atoms, also termed honeycomb lattice. These two nonequivalent sites form the sublattices A and B. The corresponding reciprocal lattice, shown in figure 2.1 (b) is also a hexagonal lattice [44, 45].

The remaining valence electron of each carbon atom, situated in the p_z-orbital perpendicular to the film plane, forms metallic π-bonds, which are delocalized. While the crystal structure and the high mechanical stability of graphene are due to the formation of the σ-bonds, its electronic properties (see section 2.1.2) are largely caused by the π-bonds [44, 45].

2.1.2 Band Structure

The band structure of graphene can be calculated using the tight-binding method. This was first done by Wallace as a starting point for the calculation of the band structure of graphite [46]. Here, the Bloch-functions $\Psi_{A,B}$ situated on sublattices A and B, are expressed as a linear combination of the atomic p_z-states $\Phi(\boldsymbol{r})$ [46, 47]:

$$\Psi_{A,B}(\boldsymbol{q},\boldsymbol{r}) = \frac{1}{\sqrt{N}} \sum_{\boldsymbol{R}_{A,B}} e^{i\boldsymbol{q}\boldsymbol{R}_{A,B}} \Phi(\boldsymbol{r}-\boldsymbol{R}_{A,B}) \tag{2.1}$$

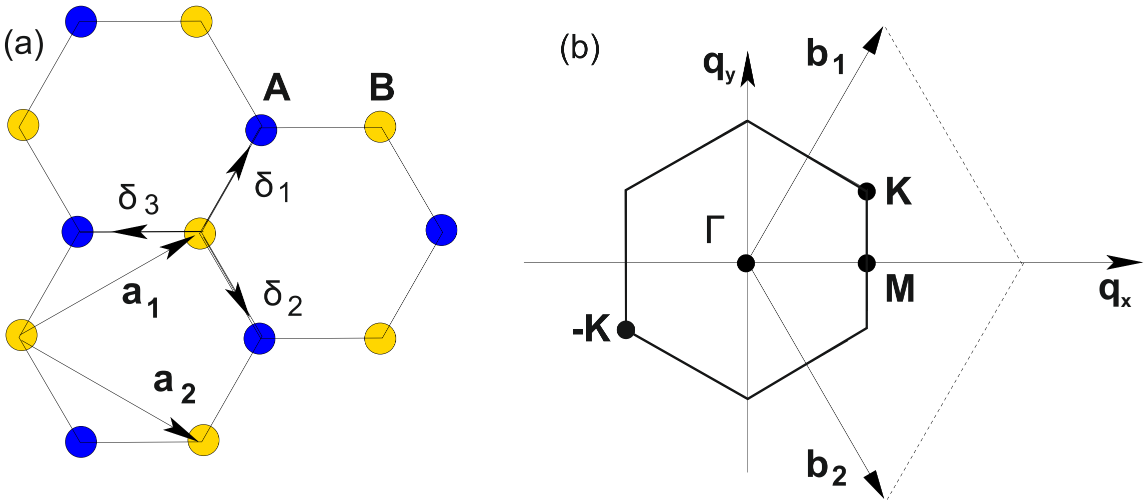

Figure 2.1: *(a) Lattice structure of graphene. The two hexagonal lattices A (blue circles) and B (yellow circles) form the honeycomb lattice. (b) Corresponding Brillouin zone. Adapted from [43].*

with $\boldsymbol{q}$ being the wave vector, N being the number of unit cells and the sum going over all atom locations $\boldsymbol{R}_{A,B}$, belonging to sublattices A or B.

Considering hopping between nearest neighbors (between atoms on the nonequivalent sublattice sites A and B in figure 2.1 (a)) only, the tight-binding Hamiltonian in the basis of the Bloch-states Ψ_A and Ψ_B reads [45]:

$$H_0(\boldsymbol{q}) = \begin{pmatrix} 0 & tS(\boldsymbol{q}) \\ tS^*(\boldsymbol{q}) & 0 \end{pmatrix} \tag{2.2}$$

with the nearest neighbor hopping parameter $t \approx 2.8\,\mathrm{eV}$ [43] and:

$$S(\boldsymbol{q}) = \sum_{\boldsymbol{\delta}} e^{i\boldsymbol{q}\boldsymbol{\delta}} = 2\exp\left(\frac{iq_x a}{2}\right)\cos\left(\frac{q_y a\sqrt{3}}{2}\right) + \exp\left(-iq_x a\right) \tag{2.3}$$

Here, the sum is over the nearest neighbors $\boldsymbol{\delta}$ (see figure 2.1 (a)) and $a = 1.42\,\text{Å}$ is the nearest neighbor distance. By solving $\det[H - E(\boldsymbol{q})] = 0$ the energy dispersion can be obtained [45, 46]:

$$E(\boldsymbol{q}) = \pm t|S(\boldsymbol{q})| = \pm t\sqrt{3 + 2\cos\left(\sqrt{3}q_y a\right) + 4\cos\left(\frac{\sqrt{3}}{2}q_y a\right)\cos\left(\frac{3}{2}q_x a\right)} \tag{2.4}$$

For the low energy range compared to the Fermi-energy, this gives a good approximation to the electronic band structure, displayed by the blue curve in figure 2.2 (a) and in figure 2.2 (b). As can be seen, the two bands (+ and − branches in equation 2.4) touch each other at the two nonequivalent points $\boldsymbol{q} = \boldsymbol{K}$ and $\boldsymbol{q} = -\boldsymbol{K}$ in figure 2.1 (b).

In pristine, undoped graphene, the Fermi energy lies directly at the intersection of these bands, and the bands therefore correspond to the valence (− branch) and

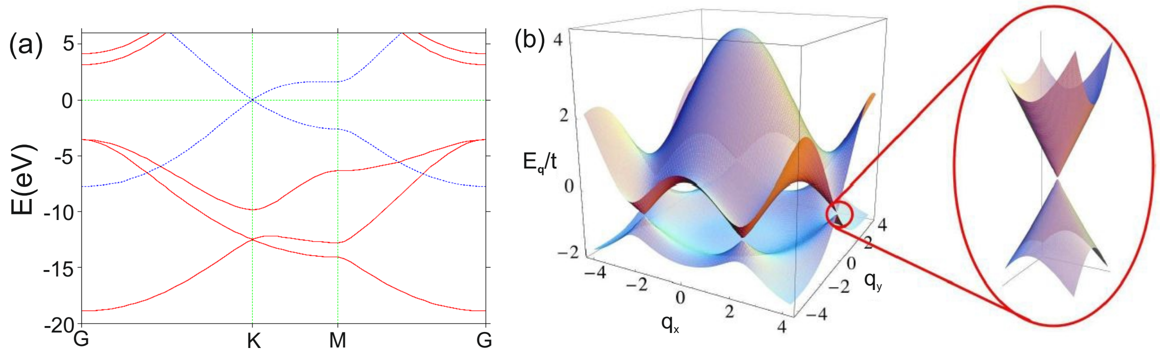

Figure 2.2: *(a) Band structure of pristine graphene. Red lines are bands comprised of σ-states and the blue lines are bands comprised of π-states. Adapted from [48]. (b) Energy spectrum of graphene with zoom-in to one of the K-points. Adapted from [43].*

conduction (+ branch) bands. Expanding equation 2.2 around the points $\boldsymbol{q} = \kappa\boldsymbol{K}$, with $\kappa = \pm 1$ being the so called valley index, gives [45]:

$$H_{\kappa\boldsymbol{K}} = \hbar v_F \begin{pmatrix} 0 & \kappa k_x - i k_y \\ \kappa k_x + i k_y & 0 \end{pmatrix} = \hbar v_F (\kappa k_x \sigma_x - k_y \sigma_y) \tag{2.5}$$

Here, $v_F = 3ta/(2\hbar) \approx 1 \cdot 10^6$ m/s [44] denotes the Fermi velocity and $\boldsymbol{k} = \boldsymbol{q} - \kappa\boldsymbol{K}$ with $|\boldsymbol{k}| \ll |\boldsymbol{K}|$. Further, the Pauli-matrices $\boldsymbol{\sigma} = (\sigma_x, \sigma_y, \sigma_z)$ are acting on the sublattice space (A, B) and the eigenvalues of $\boldsymbol{\sigma}$ are called pseudospin.

Following equation 2.5 the dispersion relation close to the Fermi energy reads:

$$E(\boldsymbol{k}) = \pm \hbar v_F |\boldsymbol{k}| \tag{2.6}$$

Due to this linear energy dispersion, as seen in the zoom-in in figure 2.2 (b), the points $\boldsymbol{q} = \kappa\boldsymbol{K}$ are termed Dirac-points or charge neutrality points (CNP).

2.2 Bilayer Graphene

2.2.1 Crystal Structure

Bilayer graphene consists of two single graphene layers that are bound by the weak van der Waals attraction. As depicted in figure 2.3 (a), there are now four nonequivalent lattice points A_1, B_1, A_2, B_2 belonging to sublattices A and B and to the layers 1 and 2.

2.2.2 Band structure

From figure 2.3 (a), it can be seen that the sites A_1 and B_2 lie exactly on top of each other, therefore giving the dominant hopping parameter $t_\perp$ between the two layers [45,

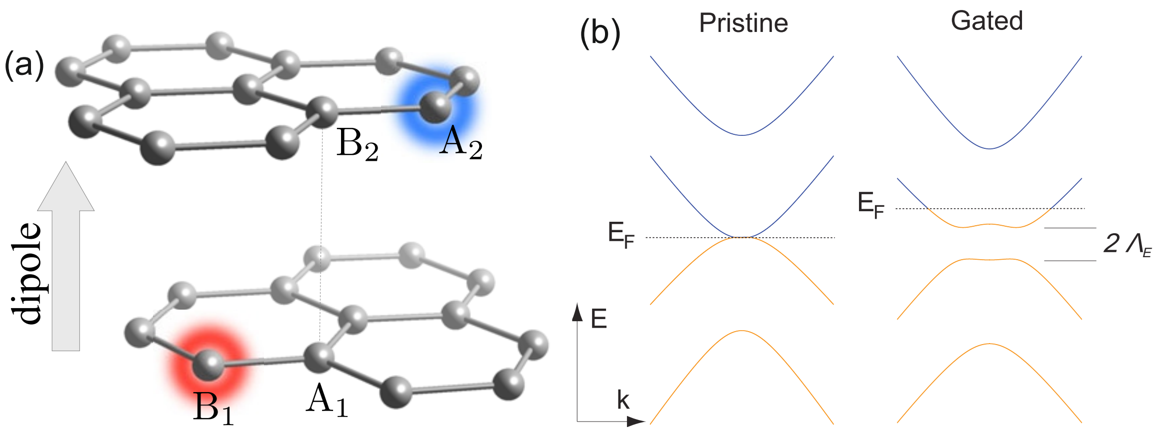

Figure 2.3: *(a) Crystal structure of bilayer graphene. Taken from [41]. (b) Band structure of bilayer graphene close to the K-points without (left) and with (right) a transverse electric field. Taken from [49].*

50]. Equivalent to equation 2.2, the Hamiltonian in the basis of p_z-states located on the sublattices A$_1$, B$_1$, B$_2$, A$_2$ (analog to equation 2.1) can be written as [45]:

$$H_0(\boldsymbol{q}) = \begin{pmatrix} 0 & tS(\boldsymbol{q}) & t_\perp & 0 \\ tS^*(\boldsymbol{q}) & 0 & 0 & 0 \\ t_\perp & 0 & 0 & tS^*(\boldsymbol{q}) \\ 0 & 0 & tS(\boldsymbol{q}) & 0 \end{pmatrix} \tag{2.7}$$

The resulting energy dispersion:

$$E(\boldsymbol{q}) = \pm\frac{t_\perp}{2} \pm \sqrt{\frac{t_\perp^2}{4} + t^2|S(\boldsymbol{q})|} \tag{2.8}$$

corresponds to 4 energy bands with two independent ± signs. These bands are depicted on the left side of figure 2.3 (b), in the vicinity of the CNP-points. The two bands closest to the Fermi energy are comprised of p_z-states located on the two lattice sites B$_1$ and A$_2$ in figure 2.3 (a) that are only weakly coupled [50, 51]. The low energy Hamiltonian close to the CNP-points in the basis of these states therefore is [45, 51, 52]:

$$H_{\kappa\boldsymbol{K}} = \frac{\hbar^2}{2m^*}\begin{pmatrix} 0 & (\kappa k_x - ik_y)^2 \\ (\kappa k_x + ik_y)^2 & 0 \end{pmatrix} \tag{2.9}$$

The energy dispersion for these two bands close to the Fermi-energy reads as:

$$E(\boldsymbol{k}) = \pm\frac{\hbar^2|\boldsymbol{k}|^2}{2m^*} \tag{2.10}$$

The two high energy bands in figure 2.3 (b) originate from states located on the lattice sites A$_1$ and B$_2$. The direct interlayer hopping between these sites causes a shift of around 400 meV from the Fermi energy. These bands can therefore be ignored when considering charge or spin transport [41].

Instead of the linear dispersion in equation 2.6, bilayer graphene shows a parabolic dispersion with a small effective mass of $m^* = t_\perp/(2v_F^2) \approx 0.054\, m_e$ [50], with m_e being the free electron mass.

Applying an external field perpendicular to the bilayer graphene lattice induces a potential energy difference $2\Lambda_E$ between the two layers. The Hamiltonian in equation 2.9 then becomes [53, 54]:

$$H_{\kappa \boldsymbol{K}} = \begin{pmatrix} \Lambda_E & \frac{\hbar^2}{2m^*}(\kappa k_x - i k_y)^2 \\ \frac{\hbar^2}{2m^*}(\kappa k_x + i k_y)^2 & -\Lambda_E \end{pmatrix} \tag{2.11}$$

The corresponding energy dispersion close to the CNP-points is depicted on the right side of figure 2.3 (b). As can be seen applying a difference in potential energy between the two layers opens an energy gap of $E_{gap} = 2\Lambda_E$ at the CNP-points [52, 55].

2.3 Spin-Orbit-Coupling

Spin-orbit-coupling (SOC) is a relativistic correction to the classical Schrödinger equation and can be described by [56]:

$$H_{SO} = \frac{\hbar}{4m_e^2c^2}(\nabla V \times \boldsymbol{p}) \cdot \boldsymbol{s} \tag{2.12}$$

with m_e being the free electron mass and $\boldsymbol{s}$ a vector with the Pauli matrices (s_x, s_y, s_z) describing the real spin as components. It reflects that an electron moving in an electric potential $V(\boldsymbol{r})$ experiences a corresponding magnetic field, acting on the spin degree of freedom. In atoms, $V(\boldsymbol{r})$ refers to the Coulomb potential of the nuclei and other electrons, while in solids $V(\boldsymbol{r})$ corresponds to the periodic crystal lattice potential. Further, other internal or external electric fields can produce additional SOC [32].

In solids SOC can influence the band structure as well as spin transport properties. However, in reality the exact crystal field $V(\boldsymbol{r})$ and therefore H_{SO} is unknown. While the specific SOC terms in the Hamiltonian can in principle be deduced by symmetry considerations, its overall value has to be calculated by numerical methods.

In the following chapter the various possible SOC terms in graphene with different symmetries are shown. For the derivation of these terms see [57, 58]. Then, SOC for the specific cases of pristine graphene, hydrogenated graphene and graphene/WSe$_2$ heterostructures is considered.

2.3.1 SOC Terms in Graphene

Including the electron spin into the consideration, the Hamiltonian from equation 2.5 describing the orbital motion for single layer graphene becomes:

$$H_{orb} = \hbar v_F(\kappa k_x \sigma_x - k_y \sigma_y)s_0 \tag{2.13}$$

now with the 4-component basis A↑, A↓, B↑, B↓, where ↑ and ↓ denotes the spin polarization in z-direction and s_0 being the identity matrix in spin space.

While the specific SOC-terms in graphene can be modeled by a tight binding approach, the parameters and therefore the magnitude of the SOC-terms are determined by density-functional theory (DFT) simulations. For the tight binding approach, spin conserving and spin flipping on-site, nearest neighbor and next-nearest neighbor hopping processes have to be taken into account. However, many of these hopping terms can be ruled out when considering the given symmetry of graphene. In turn, this means that additional SOC-terms in the overall Hamiltonian can be induced by breaking specific symmetries of the system [57].

Intrinsic SOC

Considering the symmetry of the system, it can be shown that for perfect pristine graphene, SOC can only mediate spin conserving next nearest hopping. The only allowed SOC term therefore is [57, 59]:

$$H_I = \kappa \Lambda_I \sigma_z s_z \tag{2.14}$$

This so called intrinsic SOC term was first predicted by Kane and Mele [59] and is therefore often termed Kane-Mele SOC.

Bychkov-Rashba SOC

Applying a transverse external electric field or the presence of a substrate breaks the $z/-z$ mirror symmetry as well as space inversion symmetry. Then, also spin flipping nearest neighbor hopping is allowed, which leads to the so called Bychkov-Rashba term [57, 59]:

$$H_{BR} = \Lambda_{BR}(\kappa \sigma_x s_y - \sigma_y s_x) \tag{2.15}$$

SOC due to principal plane mirror asymmetry

Breaking of the $z/-z$-mirror symmetry further allows spin flipping next-nearest neighbor hopping. This leads to the SOC term [36, 57]:

$$H_{PIA} = \Lambda_{PIA} \sigma_0 (k_x s_y - k_y s_x) a_L \tag{2.16}$$

with $a_L = \sqrt{3}a = 2.46\,\text{Å}$ being the lattice constant of graphene. Contrary to H_{BR}, H_{PIA} is also present if the $z/-z$-mirror symmetry is broken but inversion symmetry is not (this is the case for so called miniripple graphene, graphane or materials such as silicene) [57]. In that case there is a sign-difference between the terms for the different sublattices $\sigma_0 \to \sigma_z$. Due to its occurrence in different systems, H_{PIA} was termed pseudospin inversion asymmetry [36], intrinsic Rashba [60] or most fittingly principal plane mirror asymmetry induced SOC [57].

SOC due to sublattice asymmetry

Placing graphene on a substrate such as $\mathrm{WSe_2}$ can lead to a difference of the average environment of the two sublattices A and B. In this case equation 2.14 becomes sublattice dependent, giving rise to sublattice dependent factors Λ_I^A and Λ_I^B [40, 57, 61]:

$$H_I^{A/B} = \frac{\kappa}{2}[\Lambda_I^A(\sigma_z + \sigma_0) + \Lambda_I^B(\sigma_z - \sigma_0)]s_z \tag{2.17}$$

Further, the presence of the substrate induces H_{BR} as well as H_{PIA} with the lattice dependent factors Λ_{PIA}^A and Λ_{PIA}^B [40, 61]:

$$H_{PIA}^{A/B} = \frac{a_L}{2}[\Lambda_{PIA}^A(\sigma_z + \sigma_0) + \Lambda_{PIA}^B(\sigma_z - \sigma_0)](k_x s_y - k_y s_x) \tag{2.18}$$

It has to be noted that for the case of sublattice symmetry $\Lambda_I^A = \Lambda_I^B$ and $\Lambda_{PIA}^A = -\Lambda_{PIA}^B$ leading to $H_I^{A/B} = H_I$ and $H_{PIA}^{A/B} = H_{PIA}$. Further, Λ_{BR} can not be sublattice dependent, since it results from nearest neighbor hopping (therefore connecting sublattices A and B).

2.3.2 SOC in Pristine Graphene

In pristine graphene only the intrinsic SOC is present and near the K-points the effective Hamiltonian is:

$$H_{\kappa\boldsymbol{K}} = \hbar v_F(\kappa k_x \sigma_x - k_y \sigma_y)s_0 + \kappa\Lambda_I\sigma_z s_z \tag{2.19}$$

with the corresponding energy dispersion [62]:

$$E(\boldsymbol{k}) = \pm\sqrt{\Lambda_I^2 + \hbar^2 v_F^2 |\boldsymbol{k}|^2} \tag{2.20}$$

As can be seen in figure 2.4 (a) H_I induces a bandgap of $E_{gap} = 2\Lambda_I$ at the κK-points. Further, due to the presence of both time reversal and space inversion symmetry:

$$E(\boldsymbol{k},\uparrow) = E(-\boldsymbol{k},\downarrow) = E(\boldsymbol{k},\downarrow) \tag{2.21}$$

This means that both conduction and valence bands are spin degenerate. Close to the CNP-points, the conduction and valence bands therefore are built from pairs of states ($\mathrm{A}_\uparrow$, $\mathrm{B}_\downarrow$) and ($\mathrm{B}_\downarrow$, $\mathrm{A}_\uparrow$) that are split by $E_{gap} = 2\Lambda_I$ [57].

Due to the SOC induced bandgap, pristine graphene was regarded as a model system for the quantum spin-Hall effect [59] with the bulk being insulating and spin polarized conducting edge states. Further, Kane and Mele gave an estimation of $\Lambda_I \approx 100\,\mu\mathrm{eV}$, which corresponds to an experimental accessible temperature of $T = 2\Lambda_I/k_B = 2.4\,\mathrm{K}$. However, later calculations showed Λ_I to be much smaller.

SOC requires mixing of states with different magnetic quantum number (orbital momentum) and spin. However, in graphene the π-states close to the Fermi energy are comprised of p_z-states which have the same magnetic quantum number. Due to their

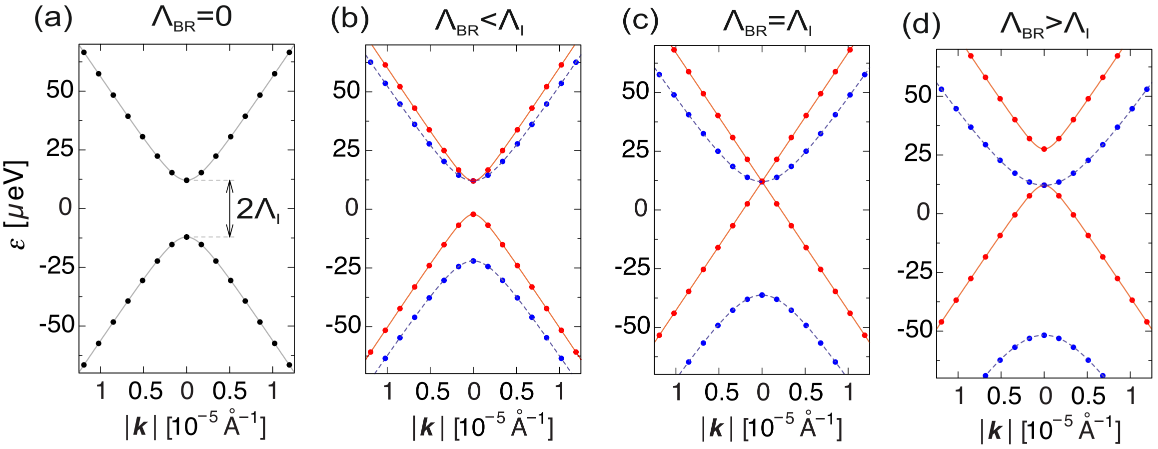

Figure 2.4: *Band-structure of pristine graphene close to the K-points for different values of Λ_I and Λ_{BR}. The red ($\eta = 1$) and blue ($\eta = -1$) curves denote different spin species. As can be seen Λ_{BR} induces spin splitting of the bands and a bandgap at $\boldsymbol{k} = 0$ can only be observed for $\Lambda_{BR} < \Lambda_I$. Adapted from [62].*

large separation in energy (see figure 2.2 (a)) compared to the SOC-strength in atomic carbon, mixing with the σ-states is greatly reduced. Tight binding studies including the π- and σ-bands predicted an intrinsic SOC-gap of only $2\Lambda_I \approx 1\,\mu\text{eV}$ [63–65]. If mixing between the p_z- and d-orbitals is also considered, the SOC was estimated to be in the range of $2\Lambda_I = 24 - 50\,\mu\text{eV}$ [62, 66, 67], which is still three orders of magnitude smaller than the SOC-strength of an isolated carbon atom $2\Lambda_C \approx 10\,\text{meV}$. This is in agreement with recent electron spin resonance measurements, performed by Sichau et al., where an intrinsic SOC in graphene of $2\lambda_I = 42\,\mu\text{eV}$ was found [68].

Applying external gate voltages by doping or charges in the substrate or capping layer can cause a perpendicular electric field. This field breaks $z/-z$-mirror symmetry and in turn introduces additional terms to equation 2.19, as described in section 2.3.1:

$$H_{\kappa\boldsymbol{K}} = H_{orb} + H_I + H_{BR} + H_{PIA} \tag{2.22}$$

with the following eigenspectrum [57]:

$$E(\boldsymbol{k}) = \eta\Lambda_{BR} \pm \sqrt{(\Lambda_I + \eta\Lambda_{BR})^2 + (\hbar v_F - \eta\Lambda_{PIA}a_L)^2|\boldsymbol{k}|^2} \tag{2.23}$$

where $\eta = \pm 1$ corresponds to different spin states (shown as red and blue in figure 2.4).

Λ_{BR} causes a spin dependent splitting of the bands of $2\Lambda_{BR}$ at the κK-points [62]. Further, Λ_{BR} reduces the band gap invoked by Λ_I and closes it for $\Lambda_{BR} \geq \Lambda_I$, as can be seen in figure 2.4 (b)-(d).

Λ_{BR} is expected to be linear with the applied electric field E and was first estimated to be $2\Lambda_{BR}/E = 0.5\,\mu\text{eV nm/V}$ [59]. Later calculations produced values of $2\Lambda_{BR}/E = 133\,\mu\text{eV nm/V}$ [63] and $2\Lambda_{BR}/E = 10\,\mu\text{eV nm/V}$ [62]. The microscopic origin of Λ_{BR} is the atomic Stark-effect, which induces mixing of π- and σ-states [62, 63, 67].

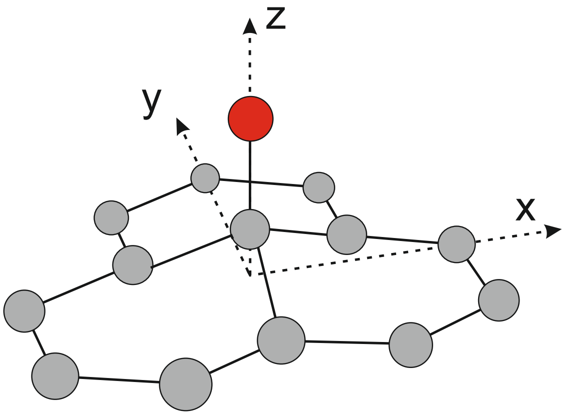

Figure 2.5: *Illustration of hydrogenated graphene. The (red) hydrogen bonds at the top-position to one of the carbon atoms in graphene. The following change from sp^2- to sp^3-hybridization leads to a local distortion of the graphene lattice. Adapted from [57].*

The existence of the Λ_{PIA}-term causes a renormalization of the Fermi velocity $v'_F = v_F - \eta\Lambda_{PIA}a_L/\hbar$ and leads to additional spin splitting for $\boldsymbol{k} \neq 0$ [58]. However for realistic values $\Lambda_{PIA} \approx \Lambda_{BR}$ and close to the κK-points with $|\boldsymbol{k}| \ll 1/a_L$ both effects can be neglected for the case of pristine graphene.

In bilayer graphene SOC was predicted to be of the same magnitude as in single layer graphene [69]. For both cases SOC is much too weak for efficient charge to spin conversion as well as spin manipulation through an electric gate. For such purposes, methods to increase SOC in graphene will be explored in the following sections.

2.3.3 SOC in Hydrogenated Graphene

As discussed in section 2.3.2, the large discrepancy of the SOC-strength in atomic carbon ($2\Lambda = 10$ meV) and pristine graphene ($2\Lambda_I = 24-50$ µeV) is due to the reduced mixing of the π- and σ-states. Atomic hydrogen has been reported to covalently bond to graphene in a way that changes the sp^2-hybridization of the carbon atoms to sp^3-hybridization [11, 48]. As shown in figure 2.5, the hydrogen atom (red in figure 2.5) bonds in the so called top position, which pulls the corresponding hydrogenated carbon atom out of plane. This leads to a local deformation of the graphene lattice which induces the required mixing of π- and σ-states [35].

In this work graphene samples, with only small concentrations of hydrogen, were investigated (amount of H/C$\approx$ 0.01 %). In this dilute case, SOC induced by the bonded hydrogen can therefore only be considered locally (in the vicinity of the bonded hydrogen atom). Theoretically, this is done by investigating a corresponding graphene supercell with one bonded hydrogen atom, where the hydrogen concentration can be controlled by adjusting the size of the supercell. Density functional theory (DFT) calculations by Gmitra et al. showed that in such a system, the local SOC-terms $\Lambda_I = -0.21$ meV, $\Lambda_{BR} = 0.33$ meV and $\Lambda_{PIA} = -0.77$ meV, according to section 2.3.1, are induced [36].

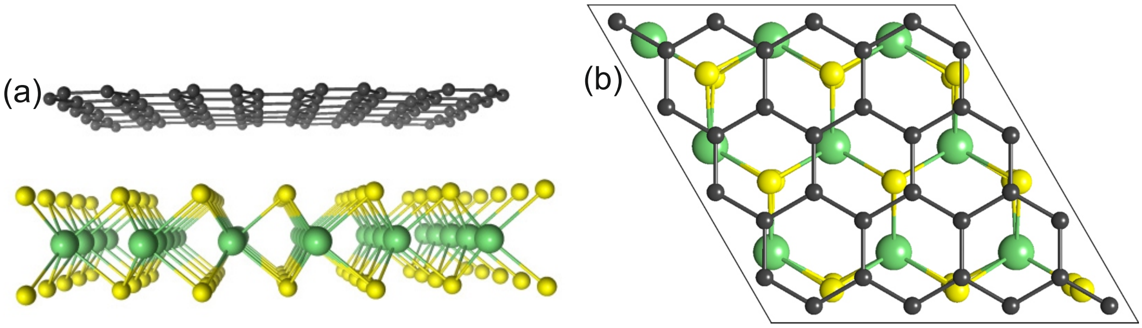

Figure 2.6: *Sketch of a* WSe_2*/graphene heterostructure in (a) side-view and (b) top-view. Here, gray denotes carbon, green tungsten and yellow selenium atoms. Taken from [61].*

2.3.4 Proximity Induced SOC in Graphene

Inducing SOC in graphene with adatoms has the disadvantage of also increasing electron scattering and therefore decreasing the electron mobility. A different method for increasing SOC in graphene is to put graphene in contact with a material with high SOC-strength. Then, weak hybridization between the graphene p_z-orbitals and the orbitals of the high SOC-substrate leads to increased global SOC in graphene [40, 61, 70].

For this, the so called transition metal dichalcogenides (TMDs) are especially suitable. Similar to graphene and hexagonal boron nitride (hBN), TMDs are layered materials and can therefore be exfoliated into two dimensional flakes. As with graphene/hBN [5, 71], a van der Waals pick-up technique can be used to fabricate graphene/TMD heterostructures with atomically smooth and clean interfaces [72, 73]. Hence, heterostructures with graphene fully encapsulated between either two TMDs or between one TMD and hBN, have shown high electron mobilities [73, 74], similar to the values found in hBN encapsulated graphene. Recently hBN/graphene/WSe_2-heterostructures have been shown to even surpass fully hBN encapsulated graphene in terms of room temperature mobility [75]. Further, detailed Raman-measurements conducted in TMD/graphene/hBN-heterostructures revealed a low amount of nanometer-scale strain and doping variations in these devices, which indicates the suitability of TMDs as high quality substrates for graphene [76].

Single Layer Graphene/WSe_2 heterostructures

In this work SOC in heterostructures containing graphene and the TMD WSe_2 are investigated. One layer of WSe_2 consists of a hexagonal lattice of tungsten (W) atoms surrounded by two hexagonal lattices of selenium (Se) atoms (see figure 2.6).

WSe_2 is a semiconductor with a direct bandgap of $E_{gap} \approx 1.7\,\text{eV}$ for the monolayer and an indirect bandgap of $E_{gap} \approx 1.2\,\text{eV}$ in the bulk [77]. Further, due to the high atomic mass of the tungsten atoms, WSe_2 shows a rather large SOC-strength of $2\Lambda_{vb} \approx 450\,\text{meV}$ in the valence and $2\Lambda_{cb} \approx -40\,\text{meV}$ in the conduction band [78].

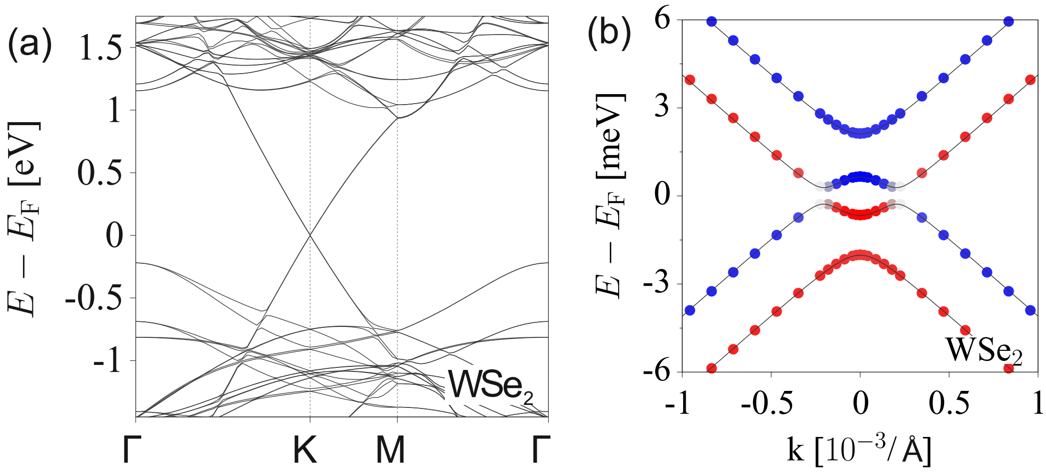

Figure 2.7: *(a) Band structure of a single layer graphene/WSe$_2$ heterostructure. (b) Zoom-in to the CNP-point in (a). Blue and red dots denote different spin orientations. Taken from [61].*

Single layer graphene on top of a WSe$_2$ monolayer is depicted in figure 2.6 from side- (a) and top-view (b). As can be seen, graphene and WSe$_2$ have different lattice constants of $a_L = 2.46$ Å for graphene and $a_L = 3.3$ Å for WSe$_2$ [78]. Due to this, atoms of sublattices A and B in graphene, on average experience a different environment, induced by the WSe$_2$ substrate [40]. Therefore, a so called staggered potential of the form $H_{st} = \Lambda_{st}\sigma_z s_0$ has to be added to the orbital Hamiltonian in equation 2.5. The presence of H_{st} leads to an orbital gap that is there even in the absence of SOC [40].

Weak mixing of the p_z-orbitals of the graphene with the d-orbitals of the W-atoms leads to an increased SOC in the graphene layer [40]. As discussed in section 2.3.1, breaking of sublattice symmetry leads to different coefficients Λ_I for the two sublattices A and B. Also, the presence of the substrate breaks $z/-z$-mirror symmetry and therefore induces the terms H_{BR} and $H_{PIA}^{A/B}$. The full low energy Hamiltonian for single layer graphene on WSe$_2$ reads:

$$H_{\kappa\boldsymbol{K}} = H_{orb} + H_{st} + H_I^{A/B} + H_{PIA}^{A/B} + H_{BR} \tag{2.24}$$

Employing DFT calculations on the supercell shown in figure 2.6 (b), Gmitra et al. obtained the values: $\Lambda_{st} = 0.54$ meV, $\Lambda_I^A = -1.22$ meV, $\Lambda_I^B = 1.16$ meV, $\Lambda_{BR} = 0.56$ meV, $\Lambda_{PIA}^A = -2.69$ meV and $\Lambda_{PIA}^B = -2.54$ meV [61].

The corresponding band structure around the Fermi-energy can be seen in figure 2.7. The linear dispersion of graphene around the CNP-points shown in figure 2.7 (a), is preserved and lies well inside the bandgap of WSe$_2$. Further, figure 2.7 (b) shows a zoom-in to the CNP-point. Here, a pronounced splitting of the spin polarized bands (blue and red dots in figure 2.7 (b)) can be observed. Further, figure 2.7 (b) reveals a band structure inversion at the CNP-point, which can lead to the occurrence of spin polarized edge states [61, 79–82].

As pointed out by Cummings et al., for the comparison with experiments it can be more convenient to write equation 2.24 as [83]:

$$H_{\kappa\boldsymbol{K}} = H_{orb} + H_{st} + H_I + H_{VZ} + H_{BR} + H_{PIA} + H_{\Delta_{PIA}} \tag{2.25}$$

with:

$$\begin{aligned} H_I &= \kappa\Lambda_I\sigma_z s_z \\ H_{VZ} &= \kappa\Lambda_{VZ}\sigma_0 s_z \\ H_{PIA} &= \Lambda_{PIA}\sigma_z(k_x s_y - k_y s_x)a_L \\ H_{\Delta_{PIA}} &= \Delta_{PIA}\sigma_0(k_x s_y - k_y s_x)a_L \end{aligned} \tag{2.26}$$

and $\Lambda_I = (\Lambda_I^A + \Lambda_I^B)/2$, $\Lambda_{VZ} = (\Lambda_I^A - \Lambda_I^B)/2$, $\Lambda_{PIA} = (\Lambda_{PIA}^A + \Lambda_{PIA}^B)/2$ and $\Delta_{PIA} = (\Lambda_{PIA}^A - \Lambda_{PIA}^B)/2$. Here, H_I is the intrinsic SOC term, also present in pristine graphene that opens a bandgap of $2\Lambda_I$ at the CNP-point. Further, in this case Λ_I is small compared to Λ_{VZ} due to the different signs of Λ_I^A and Λ_I^B. H_{VZ} causes spin-splitting between up and down spins that is opposite for the different valleys $\kappa\boldsymbol{K}$ and is therefore called valley Zeeman term [83]. As in pristine graphene, H_{PIA} leads to a renormalization of the Fermi velocity, while $H_{\Delta_{PIA}}$ also causes spin splitting for $\boldsymbol{k} \neq 0$ [57].

Since all SOC-terms in equation 2.24 depend on the average local environment of the graphene atoms of different sublattices, the relative twist angle between graphene and WSe_2 was also predicted to be of importance [84–86].

Bilayer Graphene/WSe_2 heterostructures

For heterostructures consisting of bilayer graphene and WSe_2, SOC is predicted to depend on the carrier type and an applied transverse electric field [41, 54]. As discussed in section 2.2.2, close to the CNP-points, the low energy bands in bilayer graphene are comprised of p_z-states situated on the lattice sites B_1 (marked red) and A_2 (marked blue) in figure 2.3 (a) that are not directly connected by interlayer hopping.

If bilayer graphene is in contact with WSe_2 on one side only, then the two lattice sites B_1 and A_2 experience a different average environment due to the different proximity of the two layers to the WSe_2. As discussed in section 2.2.2, the difference in potential energy between the two layers corresponds to a built in internal transverse electric field that was calculated to be $E_{int} = 0.27\,\mathrm{V/nm}$ (here, a electric field pointing from WSe_2 towards bilayer graphene is defined as positive) [41]. Then the diagonal terms in equation 2.11 lead to a population imbalance of electrons between the two layers [53]. In the case of, e.g. WSe_2 below graphene, the B_1-states are shifted down in energy and form the valence band, while the A_2-states are shifted up in energy and form the conduction band with a bandgap between them. This is shown in figure 2.8 (d) where the red circles correspond to states located on the B_1-sites and the blue circles to states located on the A_2-sites.

Since the atoms in the B_1-lattice are much closer to the WSe_2 than the atoms in the A_2-lattice, the B_1-states are also expected to experience significantly higher SOC due to proximity with WSe_2. Indeed, as shown in figure 2.8 (d), a rather large spin

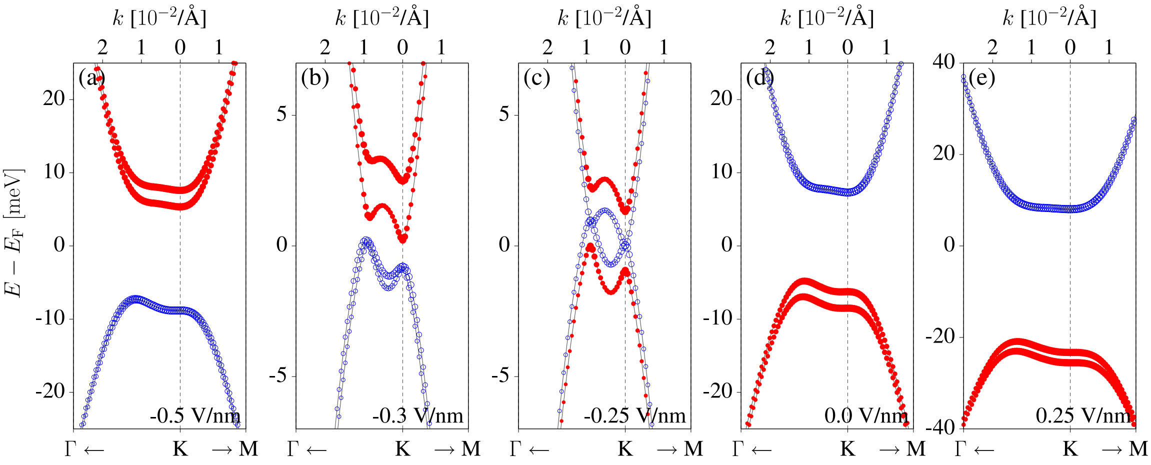

Figure 2.8: *Band structure of bilayer graphene/WSe$_2$ heterostructures at different external electric fields E_{ext} close to the CNP-point. The red and blue circles correspond to states located on the B_1 and A_2 sites in figure 2.3 (a). Taken from [41].*

splitting of 2.2 meV is observed in the valence band, while for the conduction band intrinsic SOC is expected to be close to the value of 24 μeV for pristine graphene [41].

The internal electric field can be compensated by a perpendicular external electric field E_{ext}. Applying a positive external field increases the total electric field $E_{tot} = E_{int} + E_{ext}$ which further increases the bandgap (as shown in figure 2.8 (e)) as expected for bilayer graphene (see section 2.2.2). For a negative E_{ext} the bandgap can be decreased for $E_{tot} > 0$, fully closed for $E_{tot} = 0$ (see figure 2.8 (c)) and reopened for $E_{tot} < 0$ (see figure 2.8 (b) and (a)).

Further, as can be seen in figure 2.8, for $E_{tot} < 0$ the B$_1$-states are now shifted up in energy and the A$_2$-states are shifted down in energy. Therefore, for a sufficiently large negative E_{tot} the valence band is now comprised of A$_2$-states, which experience low SOC-strength, while the conduction band is now comprised of B$_1$-states with large SOC-strength. As a result this means that at a fixed Fermi energy, either in the conduction or the valence band, SOC can essentially be switched on and off by an electric field [41].

This effect has been observed by Island et al. who employed capacitance measurements to probe the band structure of bilayer graphene/WSe$_2$ heterostructures [87]. They found a spin splitting at the CNP-points of $1.7 - 2.0$ meV that was only present in either the conduction or the valence band, depending on an applied perpendicular electric field.

However, it has to be noted that this behavior is only valid close to the CNP-points. At higher momentum $\boldsymbol{k} \neq 0$, mixing between the A$_2$ and B$_1$-states occurs due to the off-diagonal terms in equation 2.11. For a potential energy difference between the two layers $2\Lambda_E$ invoked by the transverse electric field E_{tot}, the layer polarization is given by[53, 54]:

$$g_{1,2} = \frac{1}{2} \mp \frac{\Lambda_E}{\eta\sqrt{4\Lambda_E^2 + \hbar^4 k_F^4/m^{*2}}} \tag{2.27}$$

where $\mp$ corresponds to the layers 1 and 2 and $\eta = \pm 1$ to conduction and valence bands and $k_F = \sqrt{\pi n}$ being the Fermi-momentum. Here, for $g_1 = 1$ and $g_2 = 0\,(g_1 = 0, g_2 = 1)$ the electronic states at the Fermi-energy are completely comprised of states belonging to layer 1 (2). Accordingly, at $g_1 = g_2 = 1/2$ both layers are equally populated. Therefore the SOC-strength can only be switched on and off with sufficiently large electric fields and at sufficiently low charge carrier concentrations.

3 Methods for the Characterization of Graphene Samples

For materials with potential technological relevance, not only SOC plays an important role, but also a high electron mobility is necessary. Therefore, charge transport properties are investigated in section 3.1. Further, as discussed in section 2.3.3, SOC can be induced in graphene by creating defects that locally change the atomic configuration to a sp^3-hybridization. To investigate the number of such defects, Raman-scattering can be employed and is therefore discussed in section 3.2.

3.1 Charge Transport in Graphene

Charge transport in graphene at finite charge carrier density n can be described by the Drude model. Here, the electrical conductivity is [88, 89]:

$$\sigma = \frac{ne^2\tau_p}{m^*} = ne\mu \tag{3.1}$$

with $\mu = e\tau_p/m^*$ being the charge carrier mobility and τ_p being the momentum relaxation time. Although the linear dispersion relation of graphene in equation 2.6 describes Dirac-fermions with zero rest mass, the charge carriers experience a nonzero dynamic or cyclotron mass of $m^* = m_c = \hbar k_F/v_F$, with the Fermi-wavelength $k_F = \sqrt{\pi n}$ [90]. Then, the mean free path can be calculated to be $\lambda_p = \tau_p v_F$. Further, applying the Einstein relation $\sigma = e^2 g(E_F)D$, with $g(E_F)$ being the density of states of graphene at the Fermi energy, gives the diffusion constant [91]:

$$D = \frac{v_F^2\tau_p}{2} = \frac{v_F\lambda_p}{2} = \frac{\hbar v_F\mu}{2e}\sqrt{n\pi} \tag{3.2}$$

Another important property is the elastic scattering time τ_e. In graphene it was shown that momentum relaxation is dominated by elastic scattering at long range (compared to the lattice constant a_L) scatterers [92, 93]. Thus, the momentum and elastic scattering times τ_p and τ_e are expected to be on the same order of magnitude. For graphene on SiO_2 the relation $\tau_p/\tau_e = 1.8$ was found [94]. Contrary, in graphene fully encapsulated with hBN a ratio of $\tau_p/\tau_e = 7.4$ was obtained [95]. This was attributed to the occurrence of small angle scattering, which does not affect the momentum scattering time.

Electric Field Effect in Graphene

Applying a voltage U_g between graphene and either a back- or topgate can be used to vary the charge carrier concentration and, according to equation 3.1, the conductivity of graphene [1]. In this work the graphene devices are placed onto a highly doped conducting silicon substrate covered by a 285 nm thick SiO_2 layer. If the separation between the graphene and the gate is smaller than the lateral dimension of the graphene flake, then this system can be described by the model of a simple plate capacitor. This means that the charge carrier density induced by the gate voltage U_g can be described by:

$$n = C_g \frac{(U_g - U_0)}{e} = \frac{\epsilon_0 \epsilon_r}{de}(U_g - U_0) \tag{3.3}$$

with $C_g = \epsilon_0 \epsilon_r / d$ being the gate coupling and the electric constant ϵ_0, while ϵ_r and d are the dielectric constant and the thickness of the insulating layer. Here, U_0 denotes the offset voltage, corresponding to an initial charge carrier density n_0 induced by doping by the environment.

For the case of heterostructures containing multiple dielectrics such as SiO_2, hBN or WSe_2 between gate and graphene, the gate coupling has to be modified to:

$$C_g = \left(\sum_i \frac{1}{C_i} \right)^{-1} \tag{3.4}$$

with C_i being the gate coupling of each dielectric layer.

Inducing charge carrier density in graphene by applying a gate voltage populates or depopulates the electronic states and therefore effectively shifts the Fermi energy. This is illustrated by the insets of figure 3.1, where the Fermi-energy E_F is shifted either into the conduction or valence band by applying positive or negative gate voltages. Therefore, in graphene the charge carrier type at the Fermi-energy can be changed from electron to hole-type.

Further, according to equation 3.1, the conductivity in graphene can then be controlled by applying a gate voltage with:

$$\sigma = C_g \mu (U_g - U_0) \tag{3.5}$$

Figure 3.1 shows the typical dependence of the resistivity $\rho = 1/\sigma \propto 1/U_g$ on the gate voltage in graphene. Notably the resistivity at $U_g - U_0 = 0\,\mathrm{V}$, corresponding to zero charge carrier density according to equation 3.3, shows a finite value. This behavior was shown to be caused by a spatially inhomogeneous potential landscape, which induces areas in the graphene with a nonzero density of either holes or electrons [96, 97]. Then a nonzero conductivity can be observed, despite the overall net charge carrier density being zero $n = 0$. $U_g - U_0 = 0$ is therefore termed charge neutrality point (CNP). Since these so called electron-hole puddles are caused by disorder, the width of the charge neutrality region (the induced charge carrier density range close to the CNP, where σ does not show a linear dependence on n) can also be employed to characterize the transport quality of graphene [93, 98].

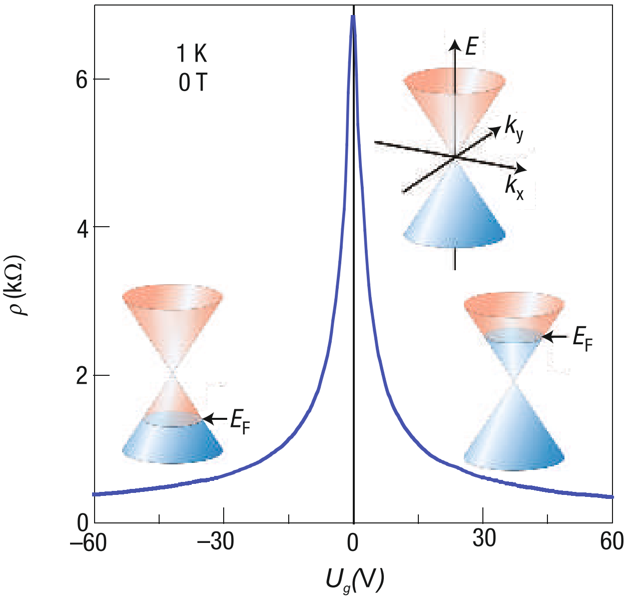

Figure 3.1: *Electric field effect in graphene. Applying a gate voltage changes the charge carrier density and therefore the resistivity of graphene. $\rho(V_g)$ shows a finite value at zero net charge carrier density. The corresponding positions of the Fermi-energy at different gate voltages are shown in the insets. Here, occupied states are shown blue, while unoccupied states are red. Taken from [2].*

Charge Carrier Density and Electric Field in Dual Gated Graphene

Employing both a back- and a topgate allows to independently control the charge carrier density as well as the external perpendicular electric field in graphene. Applying voltages between graphene and backgate U_{bg} and between graphene and topgate U_{tg} produces the bottom and top electric displacement fields [49]:

$$D_b = \frac{U_{bg} - U_{b0}}{\epsilon_0} C_b, \qquad D_t = -\frac{U_{tg} - U_{t0}}{\epsilon_0} C_t \tag{3.6}$$

Here, $C_{b,t}$ denote the gate coupling of back and topgate dielectrics and $U_{b0,t0}$ are the offset voltages due to doping by the environment.

Then, the charge carrier density n depends on the difference between D_b and D_t, while the displacement field applied to the graphene is the average of the two [49]:

$$n = \frac{D_b - D_t}{e} \epsilon_0, \qquad \bar{D} = \frac{D_b + D_t}{2} \tag{3.7}$$

By simultaneously changing U_{bg} and U_{tg} it is therefore possible to change the charge carrier density (shifting the Fermi energy) at constant electric field, or applying a variable perpendicular electric field at constant charge carrier density. Importantly, by this definition a positive $\bar{D}$ points from backgate to topgate.

3.2 Raman-Spectroscopy in Graphene

Raman-spectroscopy has long been used to study carbon systems [99, 100]. In graphene Raman measurements can be employed as a non destructive tool to investigate the number of layers, doping level and disorder [101, 102]. Relevant to this work, Raman-spectra are sensitive to the number of atomically sharp defects, such as bonded hydrogen atoms, and can therefore be used to monitor the hydrogenation process in chapter 5.

Raman scattering is an inelastic process, by which excitations in molecules or solids can be probed. For the purpose of this work monochromatic light is used to create electron-hole pairs in graphene. These can then undergo transitions by either creating or annihilating phonons. The electrons and holes can occupy and be scattered into real as well as virtual (not stationary) states, whereas transitions involving real states are resonant and therefore have a higher probability. The energy of the upon recombination emitted photons then differs from the incident photons by the energy of the involved phonons. Analysis of the spectrum of the scattered light can then be used to investigate the vibrational modes as well as the electronic states of graphene [103].

For this process both energy and momentum have to be conserved, meaning:

$$\omega_{in} = \omega_{sc} \pm \omega_{Ph} \qquad \boldsymbol{k_{in}} = \boldsymbol{k_{sc}} \pm \boldsymbol{k_{Ph}} \tag{3.8}$$

with $\omega_{in,sc}$ and $\boldsymbol{k_{in,sc}}$ being the angular frequency and wave vector of the incoming and scattered photons. Further, ω_{Ph}, $\boldsymbol{k_{Ph}}$ describe the excitation in the investigated material, with ± corresponding to the creation and annihilation of a phonon. Since the wave length of incoming and scattered photons are large compared to the lattice constant, only excitations with $\boldsymbol{k_{Ph}} \approx 0$ are allowed in this process. This leaves excitations close to the Γ-point of the phonon dispersion. However, phonon modes with $\boldsymbol{k_{Ph}} \neq 0$ are also possible if the corresponding momentum is compensated by either another phonon or by elastic scattering of the involved charge carriers [103].

In graphene the most prominent features in the Raman-spectra are the so called G-, D-, 2D (also called G' in older literature)- and D'-peaks. Examples for the corresponding transitions (multiple combinations of different real and virtual states are possible) are shown in figure 3.2. Here, an electron-hole pair is created by a photon (blue arrows). The electron-hole pair is then scattered by phonons (black arrows) or defects (green arrows) and consequently recombines upon emitting a photon (red arrows).

G-Peak

The G-peak at a wavenumber of $\nu_G \approx 1580\,\mathrm{cm}^{-1}$ in the Raman-spectrum, is caused by a transition at the Γ-point of the phonon dispersion (vertical transition in figure 3.2), satisfying equation 3.8. It corresponds to an inplane stretching of the σ-bonds and is therefore present in all sp^2 hybridized carbon forms. Further, the intensity of the G-peak is sensitive to the number of these bonds and can therefore be used to estimate the number of illuminated carbon atoms [104].

Due to electron-phonon interactions, also the phonon energy and therefore the wavenumber ν of all peaks can depend on the Fermi level position [102]. This is most pronounced for the G-peak where increased doping (both n- and p-type) leads to an increase of the peak wavenumber ν_G as well as to a decrease of the G-peak width [101,

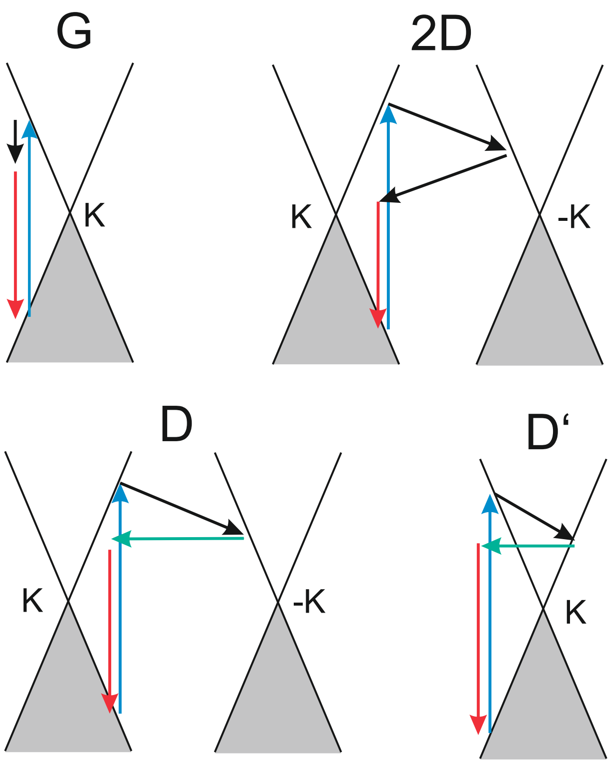

Figure 3.2: *Schematic transitions in the electron dispersion corresponding to the G-, D-, 2D- and D'-peaks in the Raman-spectrum of graphene. Scattering by phonons (black arrows) leads to a difference in energy between the incident (blue arrows) and the scattered photons (red arrows). For the occurrence of the D-and D'-peaks, elastic scattering (green arrows) has to be involved. Adapted from [103].*

105]. However, an increased G-peak linewidth can also correspond to increased disorder in defective graphene [100, 106].

2D-Peak

Contrary to the G-peak, the D- and 2D-peaks are due to a transition at the $\pm\boldsymbol{K}$ points of the phonon dispersion. This phonon mode corresponds to the breathing modes in sp^2-hybridized rings [103]. Due to the nonzero momentum of the involved phonon, a second transition is necessary to fulfill the conservation of momentum in equation 3.8. For the 2D-peak at wavenumber $\nu_{2D} \approx 2700\,\mathrm{cm}^{-1}$ the momentum of the involved phonon $\boldsymbol{k_{Ph}}$ is compensated by a second phonon with opposite momentum $-\boldsymbol{k_{Ph}}$.

The shape of the 2D-peak in the Raman-spectrum depends on the number of layers. While a single sharp 2D-peak can be observed in single layer graphene, the 2D-peak in bilayer graphene consists of four individual peaks with slightly different ν_{2D} merged together. The reason for this are the four bands in the electron dispersion of bilayer graphene shown in figure 2.3 (b) [107]. Thus, an evaluation of the shape of the 2D-peak can be employed to identify single, bilayer and few layer graphene.

As for the G-peak, the 2D-peak position depends on the Fermi-level position in graphene. However, while the G-peak only depends on the overall amount of doping, the 2D-peak position also depends on the doping type. It was reported that the 2D-peak wavenumber ν_{2D} is increased for p-type doping, while a decrease of ν_{2D} was observed for n-type doping [106]. Hence, comparing the G- and 2D-peak positions allows to determine the amount and type of doping in graphene [106, 108].

The linewidth of the 2D-peak was shown to be a sensitive tool to probe nanometer-scale strain variations in graphene [109, 110]. Scattering at these strain variations was indicated to be the dominant factor for limiting the charge carrier mobility in high quality graphene [93]. Therefore, the 2D-peak linewidth was employed to investigate possible substrates such as WSe_2, for high mobility graphene devices [76].

D-Peak

The D-peak originates from a transition with only one involved phonon and therefore occurs at a wavenumber $\nu_D \approx 1350\,\mathrm{cm}^{-1}$ that is about half of the 2D-peak. To satisfy equation 3.8, the momentum $\boldsymbol{k_{Ph}}$ of this phonon is compensated by elastic intervalley scattering (between the nonequivalent valleys $\boldsymbol{K}$ and $-\boldsymbol{K}$) of the charge carriers [103].

Intervalley scattering occurs at atomically sharp defects, such as sp^3-hybridized defects (e.g. bonded hydrogen atoms), vacancies and edges. Thus, the D-peak can not be observed in pristine graphene and the absence of a D-peak in the Raman-spectra is seen as an indication for high quality (defect free) graphene. However, the sensitivity of the D-peak intensity on the number of such defects, allows the characterization of modified graphene and graphene edges.

The occurrence of a D-peak in polycrystalline graphite was first investigated by Tuinstra and Koenig. They found the relation $L_A \propto (I_D/I_G)^{-1}$ for the relative intensity of the D-peak, where L_A denotes the average size of unperturbed carbon crystallites [100]. This relation can however not be used for randomly distributed point-like defects in graphene. Such defects were studied by Cancado et al. by investigating Ar$^+$-ion bombarded graphene samples [111]. Here, the relation:

$$L_D^2(\mathrm{nm}^2) = (1.8 \pm 0.5) \times 10^{-9} \lambda_L^4 \left(\frac{I_D}{I_G}\right)^{-1} \tag{3.9}$$

was found empirically, with λ_L being the laser wavelength (in nanometers) and L_D being the average defect distance.

The dependence of I_D/I_G (multiplied by the fourth potency of the laser excitation energy E_L^4) on L_D is shown in figure 3.3. As can be seen I_D/I_G follows equation 3.9 (black curve in figure 3.3) only in the regime of relatively low defect density. In this case the average distance between defects L_D is large and the contribution of each defect sums up independently. Then, I_D is proportional to the number of defects illuminated by the spot of the employed excitation laser and I_G is proportional to the number of illuminated carbon atoms [111]. At higher defect density L_D becomes comparable to the average distance an electron-hole pair travels before scattering with the corresponding phonon. Then, scattering at multiple defects during the Raman scattering process becomes increasingly important leading to a saturation of I_D at low L_D [111]. Further, at high defect concentration, the perturbation of the graphene lattice changes the phonon dispersion as well as the band structure of graphene [112].

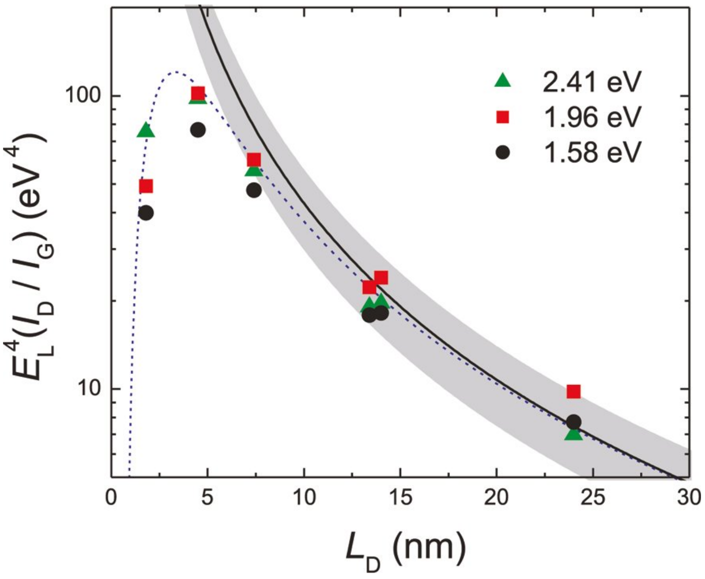

Figure 3.3: *Dependence of the relative D-peak intensity I_D/I_G on the average defect distance L_D at different laser excitation energies E_L. With increasing defect density (decreasing L_D) I_D/I_G increases for $L_D > 4$ nm and decreases at higher defect density. Equation 3.9 (solid black line) describes the experimental data in the low defect density regime. The gray shaded area marks the margin of experimental error. Taken from [111].*

This causes a broadening and a decrease of intensity of the D-peak. Consequently, as shown in figure 3.3, I_D/I_G decreases in this regime. The transition between low and high defect densities occurs at $L_D \approx v_F/\omega_D \approx 4\,\text{nm}$, with ω_D being the angular frequency of the D-peak [112].

D’-Peak

Another defect activated peak in the Raman-spectrum of graphene is the D’-peak at $\nu_{D'} \approx 1620\,\text{cm}^{-1}$. In this case, as shown in figure 3.2, the nonzero momentum of the phonon responsible for the D’-peak is compensated by elastic intravalley scattering (between states of the same valley).

Contrary to the D-peak, it was reported that the D’-peak intensity $I_{D'}$ is sensitive to the microscopic geometry and therefore to the type of atomically sharp defects. The ratio $I_D/I_{D'}$ therefore can in principle be used to differentiate between different kinds of these defects, such as sp^3-hybridized defects and vacancies [112, 113]. However, the close position of the D’- and the G-peak in the spectrum makes it difficult to accurately evaluate $I_{D'}$, since D’- and G-peak merge together even at moderate defect density. Further, since $I_{D'}$ is sensitive to the defect geometry, it is expected that possible clustering of defects, such as bonded hydrogen in this work, affects I_D and $I_{D'}$ differently, changing $I_D/I_{D'}$.

Thus, Raman-spectroscopy is a valuable tool to investigate atomically sharp defects in graphene. However, it can not reliably be employed to distinguish between the type of these defects.

4 Effects Invoked by Increased SOC in Graphene

In the following, three phenomena are discussed that arise as a consequence of SOC and therefore may be used as a sign for increased SOC. First, weak localization (WL) and antilocalization (WAL) are discussed in section 4.1. Here, relatively large SOC can influence the quantum mechanical interference of backscattered electrons. Further, SOC also leads to increased spin relaxation that can be observed with electrical spin injection and detection, as described in section 4.2. Lastly strong SOC can cause a conversion between spin to charge current (and vice versa), which will be discussed in section 4.3.

4.1 Weak Localization and Antilocalization in Graphene

4.1.1 Phase Coherence and Weak Localization

One deficiency of the semiclassical Drude-model discussed in section 3.1, is that it does not include phase coherent interactions between the charge carriers. Due to their wave-like nature scattered electrons can in principle show interference, as long as the phase coherence of the charge carriers is preserved during the scattering events. One example of such an interference effect is so called weak localization [114].

In the diffusive regime the probability for an electron to be scattered from point $\boldsymbol{R}$ to point $\boldsymbol{R'}$ can be expressed as [91, 115]:

$$P(\boldsymbol{R},\boldsymbol{R'}) = \left|\sum_i A_i\right|^2 = \sum_i |A_i|^2 + \sum_{i\neq j} A_i A_j^* \tag{4.1}$$

with A_i being the complex probability amplitude for every possible trajectory from $\boldsymbol{R}$ to $\boldsymbol{R'}$. Here, the first term on the right-hand side of equation 4.1 describes classical diffusion, while quantum interference is accounted for by the second term. Considering diffusive transport, the interference term cancels out for different start and end points $\boldsymbol{R} \neq \boldsymbol{R'}$ due to the large number of possible trajectories with different phase relation.

However, this is not the case for backscattering with $\boldsymbol{R} = \boldsymbol{R'}$. Here, for every trajectory A_i^+ there exists a time reversed path A_i^-, as depicted in figure 4.1. Due to time reversal symmetry, the probability amplitudes of these paths have to be identical

Figure 4.1: *Schematic depiction of backscattering through different scattering paths. For every scattering path A_1^+ (black solid arrows), A_2^+ (blue solid arrows), there exists a time reversed path A_1^- (black dotted arrows), A_2^- (blue dotted arrows). The scattering path A_1 encloses the area S_1 (gray region).*

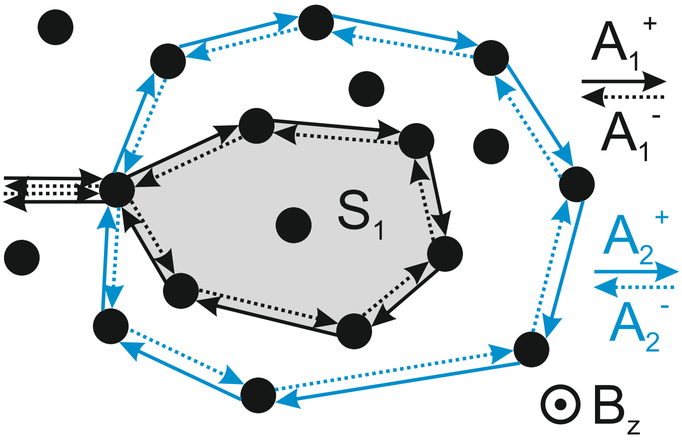

$A_i^+ = A_i^- = A_i$. The backscattering probability for a given path is therefore [91, 116–118]:

$$\left|A_i^+ + A_i^-\right|^2 = \left|A_i^+\right|^2 + \left|A_i^-\right|^2 + A_i^+ A_i^{-*} + A_i^{+*} A_i^- = 4\left|A_i\right|^2 \tag{4.2}$$

which is twice as large as the classical contribution. This increased backscattering reduces the overall conductivity and is therefore termed weak localization.

However, this is only valid for scattering paths A_i, for which the phase coherence of the charge carriers is conserved during the scattering events. The average distance over which this is the case is called phase coherence length λ_ϕ, which is related to the phase coherence time τ_ϕ by $\lambda_\phi = \sqrt{D\tau_\phi}$, with D being the diffusion constant given by equation 3.2.

τ_ϕ is limited by inelastic scattering processes such as electron-phonon and electron-electron interactions [116]. At low temperatures, where lattice vibrations are negligible in graphene, the electron-electron interaction is expected to be the dominating dephasing process in graphene [115]. Here, the random motion of the charge carriers creates a fluctuating potential, which acts as a source for inelastic scattering [118, 119]. For this process τ_ϕ is expected to be inversely proportional with temperature $\tau_\phi \propto 1/T$ [120, 121]. Further, τ_ϕ is expected to increase with increasing charge carrier density [118, 119]. It is important to note that elastic scattering at static impurities does not destroy phase coherence and therefore does not affect τ_ϕ [118].

The constructive interference of time reversed paths in equation 4.2 can be changed by applying a magnetic field perpendicular to the scattering plane. The magnetic field breaks time reversal symmetry and therefore causes an additional phase factor $A_i^\pm(B_z) = A_i e^{\pm i\phi_i^{AB}}$ that has opposite sign for A_i^+ and A_i^-. This so called Aharonov-Bohm phase is proportional to the magnetic flux $\phi_m = B_z S_i$ enclosed by the scattering path [122]:

$$\phi_i^{AB} = \frac{eB_zS_i}{\hbar} = \frac{S_i}{\lambda_B^2} \tag{4.3}$$

with the magnetic length $\lambda_B = \sqrt{(\hbar/eB)}$ and S_i being the area enclosed by the scattering path A_i. Then with an applied perpendicular magnetic field B_z, equation 4.2 becomes [118]:

$$\left|A_i^+ + A_i^-\right| = 2\left|A_i\right|^2 + 2\left|A_i\right|^2 \cos\left(\frac{2eB_zS_i}{\hbar}\right) = 2\left|A_i\right|^2 + 2\left|A_i\right|^2 \cos\left(\frac{2S_i}{\lambda_B^2}\right) \tag{4.4}$$

Therefore, the interference term oscillates with the applied magnetic field. Further, since ϕ_i^{AB} depends on the enclosed area S_i, the oscillatory contribution for the backscattered electrons also depends on the scattering path. An example for different areas enclosed by different scattering paths is shown schematically in figure 4.1.

In a diffusive system many of these paths have to be considered. Therefore, when calculating the magnetic field dependent weak localization correction to the conductivity, one has to integrate over different areas S_i. Here, the integration limits are on the order of $S_{min} \approx \lambda_e^2$, which is the smallest possible area enclosed by elastic scattering and $S_{max} \approx \lambda_\phi^2$, which describes the largest area over which phase coherence is conserved [118]. However, in the presence of a magnetic field the interference contribution of trajectories that enclose areas with $S_i > \lambda_B^2$ essentially average out and therefore do not contribute to the WL effect [91]. Consequently, the WL correction to the conductivity is reduced for magnetic fields with $\lambda_B < \lambda_\phi$ and should vanish completely for $\lambda_B < \lambda_e$. Therefore, the magnetic field dependence of the conductivity can be employed to examine characteristic scattering times of a material, as will be seen in the following sections.

4.1.2 Weak Localization and Antilocalization in Pristine Graphene

When applying the before mentioned considerations for weak localization to graphene, one has to consider the unique properties of graphene. Due to the linear bandstructure, the charge carriers in single layer graphene are chiral with the helicity operator $\boldsymbol{\sigma}\cdot\boldsymbol{p}/p$ having the eigenvalues ± 1 [115]. This means that the pseudospin (sublattice degree of freedom) direction is either parallel or antiparallel to the momentum direction, depending on the valley index and being opposite for electrons and holes. Backscattering as depicted in figure 4.1 corresponds to a semicircular rotation of the momentum direction in $\boldsymbol{k}$-space (from $\boldsymbol{k}$ to $-\boldsymbol{k}$). Due to the chirality this also corresponds to a rotation of the pseudospin direction (this is similar to the rotation of the real electron spin under the influence of SOC as will be discussed in section 4.1.3). Then, the time reversed paths in equation 4.2 both pick up a geometrical phase (or Berry phase) of $\pm\pi/2$ that is opposite in sign for the different propagation directions [123, 124]. Therefore, a phase difference between the time reversed paths of $\Delta\phi = \pi$ has to be added to equation 4.2, changing the interference from constructive to destructive. This leads to reduced backscattering and an overall enhanced conductivity, which is therefore termed weak antilocalization [125–127].

However, this is only the case if the scattering events do not change the valley index of the charge carriers. Since the chirality is opposite for the different valleys $\pm K$, the geometrical phase also depends on the valley index. Then, in the presence of intervalley scattering the acquired Berry phase essentially cancels out for scattering paths with $S_i > \lambda_{iv}^2$ with $\lambda_{iv} = \sqrt{D\tau_{iv}}$ being the intervalley scattering length. Hence, intervalley scattering reverts the interference condition to constructive interference and restores weak localization if $\tau_{iv} < \tau_\phi$ [125–128].

Further, the linear dispersion with the corresponding chiral properties of the charge carriers in graphene is only valid close to the CNP-points. At higher energy so called trigonal warping (deviation from the linear dispersion) introduces asymmetry to the dispersion relation. This breaks the effective time reversal symmetry in a single valley (while real time reversal also changes the valley index) and therefore reduces interference of the time reversed paths [127]. This effect can be accounted for by the valley conserving scattering time τ_w corresponding to this trigonal warping effect [128, 129]. Also, intravalley scattering at lattice dislocations such as ripples in graphene [130] and atomically sharp defects [127] can destroy the chiral nature of the charge carriers, which also breaks this effective single valley time reversal symmetry. These chirality breaking scattering effects are characterized by the time τ_z. Combining these two scattering mechanisms gives the scattering rate $\tau_*^{-1} = \tau_w^{-1} + \tau_z^{-1}$. Since the two different valleys have opposite chirality and trigonal warping, strong intervalley scattering can suppress these chirality breaking effects and restore WL [131].

Considering these effects, the weak localization correction to the conductivity was calculated by McCann et al. to be [128]:

$$\Delta\sigma(B) = \frac{e^2}{\pi h}\left[F\left(\frac{\tau_B^{-1}}{\tau_\phi^{-1}}\right) - F\left(\frac{\tau_B^{-1}}{\tau_\phi^{-1} + 2\tau_{iv}^{-1}}\right) - 2F\left(\frac{\tau_B^{-1}}{\tau_\phi^{-1} + \tau_{iv}^{-1} + \tau_*^{-1}}\right)\right] \tag{4.5}$$

with $F(z) = \ln(z) + \Psi(1/2 + 1/z)$, the Digamma function $\Psi(x)$ and $\tau_B^{-1} = 4eDB_z/\hbar$.

Experimentally a good fit between low field magnetoconductivity and equation 4.5 has been achieved [132, 133]. Since equation 4.5 depends on different scattering times, WL can be employed to investigate the various scattering mechanisms in graphene. In pristine single layer graphene a strongly suppressed WL effect has been observed due to short τ_* that was approaching the elastic scattering time τ_e [131, 133]. Comparing WL- with Raman-measurements in graphene on hBN showed local strain variations in graphene to be the dominant intravalley scattering mechanism limiting τ_* as well as τ_e [93, 98].

As mentioned above, WL can be restored by strong intervalley scattering. Therefore, more pronounced WL has been observed in samples with small sample width due to a higher importance of intervalley scattering at the sample boundaries [131]. Similarly, patterned graphene with an etched antidot lattice has been shown to experience WL with a small λ_{iv}, depending on the antidot-lattice period [134–136].

Another source for intervalley scattering are sp^3-hybridizing defects such as attached hydrogen-atoms (as discussed in section 3.2). Indeed, applying hydrogen to single layer graphene has been shown to produce a large WL-effect followed by a transition to strong localization at higher hydrogen exposure [137–139]. Together with Raman-spectroscopy, this makes WL an ideal tool to characterize hydrogenated graphene samples.

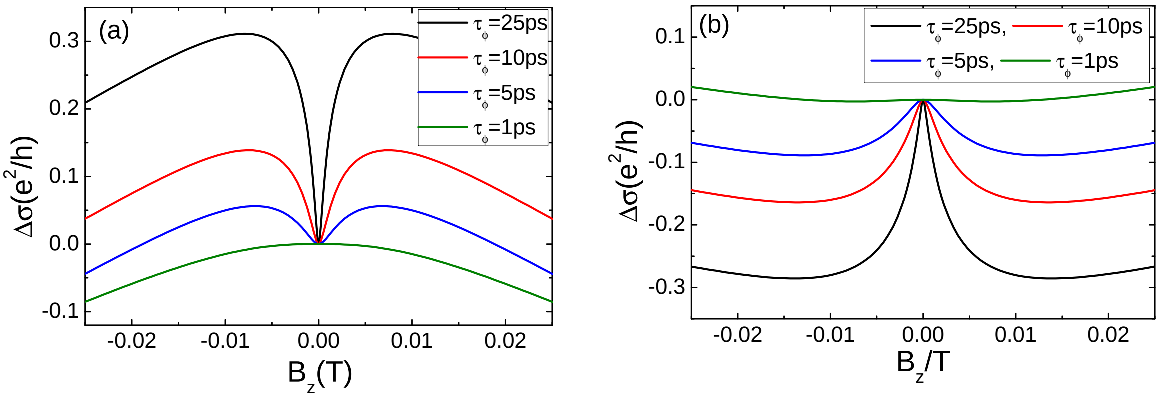

Figure 4.2: *(a) Transition from WL at long phase coherence time τ_ϕ to WAL at short τ_ϕ. Here realistic values for single layer graphene of $D = 0.05\,m^2/s$, $\tau_{iv} = 20\,ps$ and $\tau_* = 0.5\,ps$ were used in equation 4.5. (b) Decrease of WAL-peak with decreasing τ_ϕ according to equation 4.7, with $D = 0.05\,m^2/s$, $\tau_{sym} = 0.5\,ps$ and $\tau_{asy} = 5\,ps$.*

For the phase coherence time, the dependence with temperature $\tau_\phi \propto 1/T$ was found. Further, τ_ϕ has been shown to decrease with increasing charge carrier density [131, 140]. This is consistent with electron-electron interaction being the dominant dephasing effect. However, at low temperatures (or high charge carrier density) an upper limit for λ_ϕ has been found. For narrow samples this was attributed to the finite sample size as λ_ϕ approaches the sample width $\lambda_\phi \approx W$ [131]. For larger samples λ_ϕ has been shown to be limited by spin-flip scattering at magnetic impurities [141] (as will be discussed in section 4.2.4). Further, Lundeberg et al. observed a decrease of the phase coherence time when applying an inplane magnetic field [142]. This was attributed to ripples in the graphene plane. Due to these ripples, the inplane magnetic field generates an out-of plane component in the corrugated graphene. This leads to a random additional Aharonov-Bohm phase that effectively causes dephasing of time reversed paths.

The intervalley scattering length λ_{iv} was shown to be independent of temperature and charge carrier density [140]. This is since λ_{iv} corresponds to the average distance between static short range defects. Hence, by increasing temperature or decreasing charge carrier density, a transition from $\tau_\phi > \tau_{iv,*}$ to $\tau_\phi < \tau_{iv,*}$ and therefore from weak localization to weak antilocalization can be achieved. This behavior is shown in figure 4.2 (a) for typical values for single layer graphene. As can be seen the WL dip in the conductivity around $B_z = 0\,\mathrm{T}$ vanishes with decreasing phase coherence time τ_ϕ. Further, at low τ_ϕ a transition from the WL-effect at low magnetic field to the WAL-effect occurs. Experimentally, this transition has been observed by Tikhonenko et al. [143].

For the case of bilayer graphene the above considerations have to be altered by the fact that the Berry phase in bilayer graphene is twice that in single layer graphene [45]. Hence, the time reversed paths in equation 4.2 now experience a phase difference of $\Delta\phi = 2\pi$, which leads to constructive interference. As in single layer graphene, chirality breaking intravalley scattering characterized by τ_* suppresses WL, while intervalley scattering with τ_{iv} restores WL. Therefore, for bilayer graphene the weak localization correction has to be modified to [144]:

$$\Delta\sigma(B) = \frac{e^2}{\pi h}\left[F\left(\frac{\tau_B^{-1}}{\tau_\phi^{-1}}\right) - F\left(\frac{\tau_B^{-1}}{\tau_\phi^{-1} + 2\tau_{iv}^{-1}}\right) + 2F\left(\frac{\tau_B^{-1}}{\tau_\phi^{-1} + \tau_{iv}^{-1} + \tau_*^{-1}}\right)\right] \tag{4.6}$$

WL in bilayer graphene was first observed by Gorbachev et al, who found electron-electron interaction to be the dominating dephasing mechanism at low temperatures, as in single layer graphene. [145]. The same conclusion was drawn by Engels et al., who employed WL measurements to investigate bilayer graphene that was fully encapsulated between hBN [146].

4.1.3 Weak Antilocalization in Graphene with SOC

As was first calculated by Hikami et al., SOC can significantly alter the interference behavior of backscattered charge carriers [147]. In the presence of strong SOC, the electron spin is rotated when traversing scattering paths such as depicted in figure 4.1. Since this rotation is dependent on the orbital motion of the scattered electron, it is opposite for the time reversed paths A_i^+ and A_i^-. Similar to the chirality argument for graphene in section 4.1.2, rotation of the real electron spin results in an acquired phase of the wave function. Equivalent to the pseudospin in single layer graphene, a 2π rotation of the real spin changes the sign of the electron wave function (corresponding to an acquired phase of π) [43, 148]. Therefore, an additional phase difference has to be added to equation 4.2, when calculating the interference of time reversed backscattered electron waves.

For the case of strong SOC with $\tau_{SO} \ll \tau_\phi$, where τ_{SO} is the spin-orbit scattering time (which will be discussed in more detail in section 4.2.3), the spin states of the backscattered waves are completely randomized. However, since the spin rotation is opposite for time reversed paths, it can be shown that the average interference term leads to destructive interference, reducing the backscattering probability to half of the classical contribution [118, 147, 148].

In graphene this SOC induced WAL-effect also depends on the type of SOC. While SOC that is symmetric in the the $z/-z$-direction leads only to a reduction of the WL-correction, the presence of $z/-z$-mirror symmetry breaking SOC causes WAL behavior. Assuming strong intervalley scattering, McCann and Falko calculated the low magnetic field range conductivity correction for graphene with SOC [149]:

$$\Delta\sigma(B) = -\frac{e^2}{2\pi h}\left[F\left(\frac{\tau_B^{-1}}{\tau_\phi^{-1}}\right) - F\left(\frac{\tau_B^{-1}}{\tau_\phi^{-1} + 2\tau_{asy}^{-1}}\right) - 2F\left(\frac{\tau_B^{-1}}{\tau_\phi^{-1} + \tau_{asy}^{-1} + \tau_{sym}^{-1}}\right)\right] \tag{4.7}$$

Here, τ_{sym} is the spin-orbit scattering time corresponding to SOC that is symmetric in the $z/-z$-direction, while τ_{asy} accounts for asymmetric SOC. The overall spin-orbit scattering time corresponds to $\tau_{SO}^{-1} = \tau_{sym}^{-1} + \tau_{asy}^{-1}$. It has to be noted that equation 4.7 is only valid for $\tau_{iv} < \tau_{\phi,sym,asy}$. However, as will be discussed in section 6.2.3, for

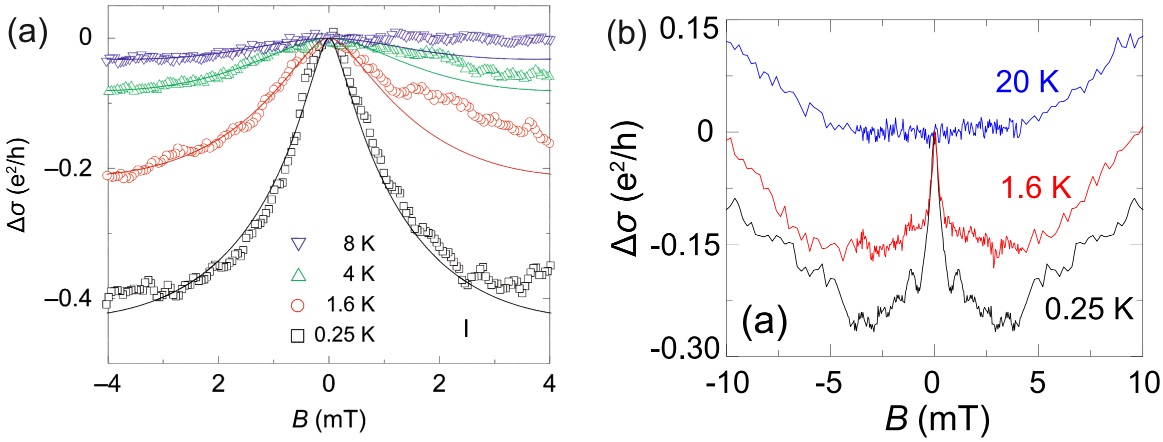

Figure 4.3: *Correction to the conductivity due to the WAL-effect in graphene/TMD structures. (a) WAL in graphene, placed onto* WS_2*. Taken from [152]. (b) WAL in graphene, placed onto* WSe_2*. Taken from [153]. In both systems, a decay of the WAL-peak with increasing temperature, can be observed due to the decrease of* τ_ϕ*.*

graphene/TMD heterostructures this is not necessarily the case. Then, a more elaborate formula has to be applied that captures the various scattering times discussed in this chapter [150].

Figure 4.2 (b) shows the magnetic field dependent WAL-correction according to equation 4.7 for different τ_ϕ. As can be seen, the low magnetic field peak in the conductivity vanishes with decreasing phase coherence time (increasing temperature). Therefore, the case of SOC induced WAL in single layer graphene can be distinguished from the chirality induced WAL without SOC by their opposite temperature dependence.

The occurrence of a WAL-peak in the conductivity at low temperatures is therefore a clear indication for increased SOC in graphene. Further, since equation 4.7 depends on the different spin-orbit scattering times τ_{sym} and τ_{asy}, WAL can be employed to investigate the strength of different kinds of SOCs in graphene. The dependence of τ_{sym} and τ_{asy} on the SOC-strength will be discussed in section 4.2.

In recent years, WAL was employed to investigate interface induced SOC in graphene, both before and after the experiments in chapter 6 were conducted and published in [151]. SOC induced WAL in graphene/TMD heterostructures was first observed by Wang et al. for single layer graphene placed onto bulk WS_2[152]. They further observed WAL in both single, bilayer and trilayer graphene placed onto WSe_2 and MoS_2 [153]. Measurements from these publications are shown in figure 4.3 (a) for a system, where graphene was placed onto WS_2 and figure 4.3 (b) for graphene placed onto WSe_2. Here, a clear peak in the conductivity around $B = 0\,\mathrm{T}$, in accordance with the WAL-effect, can be observed in both systems. Further, this peak diminishes rapidly with increasing temperature, which is a clear sign of the decay of the phase coherence time in these samples (see figure 4.2 (b) for comparison).

Yang et al. observed WAL in both single and bilayer graphene covered with bulk

WS_2[154] as well as CVD grown monolayer WSe_2 and MoS_2[155]. Employing both a top- and a backgate for the case of single layer graphene below bulk WS_2, a weak dependence of the WAL feature (and therefore of the induced SOC-strength) on a transverse electric field has been observed [154, 156].

Wakamura et al. found a substantially higher WAL-effect induced in single layer graphene when using CVD grown monolayer WS_2, WSe_2 and MoS_2 as compared to bulk TMDs [157, 158]. This was attributed to a larger effective contact area between graphene and the TMD. The more flexible monolayer TMDs could arguably compensate surface corrugations such as ripples in graphene. However, due to the different sample fabrication between monolayer and bulk TMD samples other potential sources for the reduced SOC in the bulk case, such as contaminations between the layers and a difference in the environment of the heterostructures, can not be ruled out.

Investigations of WAL in bilayer graphene encapsulated by two bulk layers of WS_2, performed by Afzal et al. showed only a weak dependence on an applied perpendicular electric field [159]. This is not surprising, since due to the presence of WS_2 on both sides of graphene, no large difference in SOC-strength between the two graphene layers, as discussed in section 2.3.4, is expected.

WAL in WSe_2/single layer graphene/hBN-heterostructures was investigated by Zihlmann et al. [160, 161]. Due to the high mobility in these samples (as will be shown in chapter 6), WAL was investigated only close to the CNP, to remain in the diffusive regime. Here, no dependence of the spin orbit scattering times on an applied electric field were found within their margin of error. Further, a decrease of the phase coherence time with an applied inplane magnetic field was found. This was attributed to increased dephasing at ripples in graphene, according to [142].

Overall, employing the TMDs containing tungsten (WS_2 and WSe_2) showed smaller spin-orbit scattering times (resulting in a larger WAL-peak in the conductivity), indicating a larger induced SOC-strength than by using MoS_2 [153, 155, 158]. This is due to the higher mass of tungsten compared to molybdenum and consequently larger induced SOC-strength, which is consistent with theoretical predictions [61].

4.2 Spin Transport in Graphene

4.2.1 Electrical Spin Injection and Detection

Another approach to investigate the SOC of a material is to examine the transport properties of an injected spin current. In graphene the most accessible method for creating and detecting such a spin current is to employ electrical spin injection and detection by a ferromagnetic material. For a more detailed theoretical description of electrical spin injection, spin transport, spin dynamics and spin relaxation mechanisms see [31, 32, 162].

Other methods for creating a spin current in graphene include spin pumping by excitation of a ferromagnet close to the ferromagnetic resonance [163–166], optical spin injection with circularly polarized light through an adjacent TMD monolayer [167, 168] and spin injection through the spin-Hall effect (which will be discussed in section 4.3). Further, detection of a spin accumulation in graphene can be achieved by employing contacts with high SOC (Pd or Pt), which convert the spin current to a charge current through the inverse spin-Hall effect in these contact materials [164, 166, 169].

Electrical Spin Injection by a Ferromagnet

To achieve electrical spin injection, a ferromagnetic material (F-region) is placed in contact with a nonmagnetic material, such as graphene (N-region) and a current is driven through the F/N-interface. According to the Mott two current model (which is valid if the spin relaxation length in a material is larger than the mean free path), electric current carried by charge carriers with different spin orientations can be considered independently [170, 171].

Due to exchange interaction, the density of states g at the Fermi energy of a ferromagnet is different for charge carriers with spin either parallel or antiparallel to the magnetization direction (here denoted ↓ and ↑), meaning $g_\uparrow(E_F) \neq g_\downarrow(E_F)$ [172]. Therefore, the different spin species experience different conductivities $\sigma_\uparrow \neq \sigma_\downarrow$. While the overall conductivity is given by the sum of the two spin dependent conductivities $\sigma = \sigma_\uparrow + \sigma_\downarrow$, a spin conductivity can be defined as $\sigma_s = \sigma_\uparrow - \sigma_\downarrow$. Then, a nonzero conductance polarization $P_\sigma = \sigma_s/\sigma \neq 0$ can be found in a ferromagnet.

Further, the presence of a bias voltage across a device gives rise to space and spin dependent quasi-chemical potentials $\tilde{\mu}(x)_{\uparrow,\downarrow}$. Analog to the conductivity, the overall and spin quasi-chemical potentials are $\tilde{\mu}(x) = \frac{1}{2}(\tilde{\mu}_\uparrow(x) + \tilde{\mu}_\downarrow(x))$ and $\tilde{\mu}_s(x) = \frac{1}{2}(\tilde{\mu}_\uparrow(x) - \tilde{\mu}_\downarrow(x))$. Then, with $j_{\uparrow,\downarrow} = \sigma_{\uparrow,\downarrow}\nabla\tilde{\mu}_{\uparrow,\downarrow}(x)$ follow the charge and spin current densities [32]:

$$j = j_\uparrow + j_\downarrow = \sigma\nabla\tilde{\mu}(x) + \sigma_s\nabla\tilde{\mu}_s(x) \tag{4.8}$$

$$j_s = j_\uparrow - j_\downarrow = \sigma_s\nabla\tilde{\mu}(x) + \sigma\nabla\tilde{\mu}_s(x) \tag{4.9}$$

As discussed above, the two spin species in a ferromagnet have different conductivities, meaning $\sigma_{s,F} \neq 0$. Hence, an applied bias voltage causes a charge as well as a spin current.

Applying a current between a ferromagnet and a nonmagnetic conductor, such as graphene, therefore creates a nonequilibrium imbalance between ↑- and ↓-spins at the interface. This corresponds to a nonzero $\tilde{\mu}_{s,N}(0)$, which is thus termed spin accumulation (here, $x = 0$ corresponds to the F/N-interface with $x < 0$ denoting the ferromagnetic and $x > 0$ the nonmagnetic region). Since $\sigma_{s,N} = 0$, the spin accumulation $\tilde{\mu}_{s,N}(0)$ in the nonmagnet then causes a spin current $j_{s,N} = \sigma_N\nabla\tilde{\mu}_{s,N}(0)$, according to equation 4.9 [32].

Spin Injection Efficiency and Conductivity Mismatch Problem

It can be shown that the spin accumulation at the interface is [32]:

$$\tilde{\mu}_{s,N}(0) = -jP_jR_N \tag{4.10}$$

Here, $R_N = \frac{\lambda_{s,N}}{\sigma_N}$ is the effective resistance of the nonmagnetic region with $\lambda_{s,N}$ being the spin diffusion length (which will be discussed in the following sections). Therefore, the spin accumulation $\tilde{\mu}_{s,N}(0)$ is proportional to the spin polarization $P_j = j_s/j$ of the current through the F/N interface, which is also termed spin injection efficiency.

For a F/N-junction the spin injection efficiency is given by [32]:

$$P_j = \frac{R_F}{R_F + R_N} P_{\sigma,F} \tag{4.11}$$

Since for a metallic ferromagnet and a semiconducting nonmagnet $R_F = \frac{\lambda_{s,F}}{\sigma_F} \ll R_N$ and therefore $P_j \approx \frac{R_F}{R_N} P_{\sigma,F} \ll P_{\sigma,F}$, the spin injection efficiency is greatly reduced. This is known as the conductivity mismatch problem. One possible solution for this is to introduce a high resistance interlayer between the ferromagnet and the nonmagnet. This can be achieved by using a very thin insulator, which acts as a tunnel barrier between the two materials. Then, the spin injection efficiency becomes [32]:

$$P_j = \frac{R_F P_{\sigma,F} + R_c P_\Sigma}{R_F + R_c + R_N} \tag{4.12}$$

with R_c being the contact resistance and P_Σ being the conductance spin polarization of the tunnel barrier. For a high resistance tunnel barrier with $R_c \gg R_F, R_N$, the spin injection efficiency then is $P_j \approx P_\Sigma$. Hence, in this case P_j is entirely dependent on the contact spin polarization P_Σ.

Since tunneling through a tunnel barrier is dependent on the density of states at the Fermi energy of the materials on both sides of the barrier, which is spin dependent in a ferromagnet, a nonzero contact spin polarization can be found $P_\Sigma \neq 0$ [173].

Electrical Spin Detection by a Ferromagnet

Inversely to electrical spin injection, a spin accumulation in a nonmagnet can be detected by an adjacent ferromagnetic electrode. Here, in the presence of a highly resistive tunnel barrier, $\mu_{s,N}(x_0)$ in the nonmagnet induces a drop in electrical potential at the contact to a ferromagnet at $x = x_0$ of [32]:

$$U = -P_j \tilde{\mu}_{s,N}(x_0) \tag{4.13}$$

Therefore, a spin accumulation in a nonmagnetic material can be investigated by an electrical potential induced in an adjacent ferromagnetic contact.

4.2.2 Spin Transport and Spin Dynamics

As discussed in the previous sections, a spin accumulation $\tilde{\mu}_s(0)$ can be created in graphene by driving a current through a ferromagnetic contact. Then, the evolution of the spin accumulation can be probed after a distance x_0 as $\tilde{\mu}_s(x_0)$ by a second ferromagnetic contact. The dependence of $\tilde{\mu}_s$ on the distance and on an external magnetic field can then be used to examine material properties such as SOC.

A spin accumulation $\tilde{\mu}_s$ corresponds to a nonequilibrium difference of the charge carrier densities of the two spin species. This spin density is denoted as $s = n_\uparrow - n_\downarrow$ and depends on the spin accumulation as [32]:

$$s = s_0 + 4e\tilde{\mu}_s \frac{g_\uparrow(E_F)g_\downarrow(E_F)}{g(E_F)} \tag{4.14}$$

Since in a nonmagnet the equilibrium spin density $s_0 = 0$ as well as $g_\uparrow(E_F) = g_\downarrow(E_F)$, the spin density is proportional to the spin accumulation:

$$s = 4e\tilde{\mu}_s g(E_F) \tag{4.15}$$

In the above considerations the polarization of the spin density (and therefore the spin accumulation) was given by the magnetization direction of the injecting and detecting ferromagnetic contacts. Applying an external magnetic field leads to a rotation of the injected spin density $\boldsymbol{s}$. In a diffusive system the evolution of $\boldsymbol{s}$ then follows the Bloch-Torrey equation [32, 174]:

$$\frac{\partial \boldsymbol{s}}{\partial t} = \boldsymbol{s} \times \boldsymbol{\omega_L} + D\nabla^2 \boldsymbol{s} - \frac{\boldsymbol{s}}{\tau_s} \tag{4.16}$$

with the Larmor frequency $\boldsymbol{\omega_L} = \gamma \boldsymbol{B}$ and the gyromagnetic ratio γ. Here, the first term on the right hand side of equation 4.16 describes precession of the spins under the applied magnetic field and the second term denotes diffusion of the spin density. Spin relaxation, meaning the loss of nonequilibrium spin polarization after a certain time is accounted for by the third term in equation 4.16. It has to be noted that in general the spin relaxation time can also depend on the orientation of the spin density, meaning e.g. different spin relaxation times for inplane and out-of plane spins. Sources of spin relaxation in graphene will be discussed in the following section.

Solving the steady state condition $\frac{\partial s}{\partial t} = 0$ of equation 4.16 without a magnetic field gives [32]:

$$\boldsymbol{\tilde{\mu}_s}(x) = \boldsymbol{\tilde{\mu}_s}(0)e^{-x/\lambda_s} \tag{4.17}$$

meaning that the spin accumulation at $x = 0$ decreases exponentially with the spin relaxation length that is given by $\lambda_s = \sqrt{D_s \tau_s}$. In graphene it was found that the spin diffusion constant D_s is equal to the charge diffusion constant $D_s = D$ [175–177].

Nonlocal spin valve

Experimentally spin transport can be studied by employing the so called nonlocal spin valve device setup [178], shown in figure 4.4 (a). Here, a current is applied between contacts 1 and 2 and a voltage is measured between contacts 3 and 4. Contacts 2 and 3 are ferromagnetic with a high resistance tunnel barrier (blue area in figure 4.4 (a)) to overcome the conductivity mismatch problem, described in section 4.2.

Applying a charge current I between contacts 1 and 2 causes a spin accumulation below contact 2 that diffuses in both directions. The resulting spin accumulation

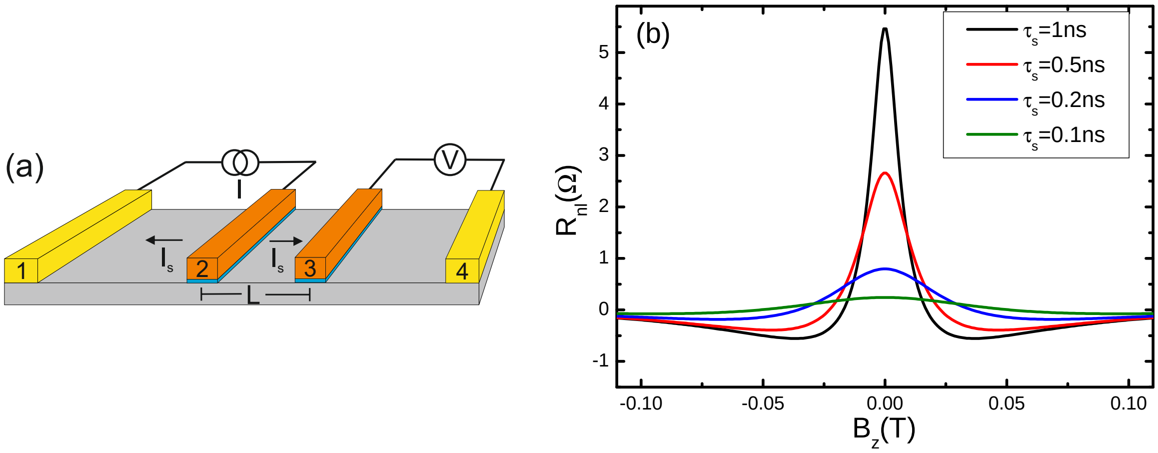

Figure 4.4: *(a) Scheme of nonlocal spin valve configuration. Ferromagnetic contacts 2 and 3 with high resistance tunnel barrier (blue area) act as spin injector and detector. Importantly, this configuration allows to separate charge current I and spin current I_s. (b) Magnetic field dependence of nonlocal resistance according to equation 4.20 for different spin lifetimes τ_s.*

beneath contact 3 then induces the nonlocal voltage. In this geometry the detector contacts are outside of the current path, which allows to separate the charge current I and spin current I_s. This minimizes spurious effects such as magnetoresistance of the ferromagnetic contacts [179]. To prevent any spin dependent signal to be caused by the outer contacts, contacts 1 and 4 are usually either far away from contacts 2 and 3 (compared to the spin diffusion length λ_s) or are made from a nonmagnetic material.

For a geometry with channel width W and for the case that the injector and detector have parallel magnetization, the nonlocal resistance can be found by combining equations 4.10, 4.13 and 4.17:

$$R_{nl} = \frac{U_{nl}}{I} = \frac{P_j^2 \lambda_s}{2W\sigma} e^{-L/\lambda_s} \tag{4.18}$$

Here, it is assumed that the injector and detector, separated by the distance L, have the same spin injection efficiency $P_j^{inj} = P_j^{det} = P_j$.

In experiments the relative orientation of the magnetization of injector and detector contacts can be changed from parallel to antiparallel, which changes the sign of the nonlocal resistance $R_{nl}^{par} = -R_{nl}^{anti}$. Then a jump in the nonlocal resistance of:

$$\Delta R_{nl} = R_{nl}^{par} - R_{nl}^{anti} = 2R_{nl} \tag{4.19}$$

can be observed.

Hanle effect

According to equation 4.16, applying a magnetic field perpendicular to the polarization of the injected spins induces a precession of the spins. The dependence of the spin accumulation on the magnetic field is termed Hanle effect.

Similar to the considerations for weak localization in section 4.1, different possible paths between injector and detector with travel times t, resulting in precession angles $\omega_L t$, have to be considered. In the nonlocal geometry shown in figure 4.4 (a) the nonlocal resistance in the presence of a magnetic field perpendicular to the contact magnetization therefore becomes [32]:

$$R_{nl}(\omega_L) = R_{nl}(0) \int_0^\infty \mathrm{d}t \frac{1}{\sqrt{4\pi Dt}} e^{-L^2/4Dt} \cos(\omega_L t) e^{-t/\tau_s} \tag{4.20}$$

Here, the first term of the integral $\frac{1}{\sqrt{4\pi Dt}} e^{-L^2/4Dt}$ denotes the probability of an injected spin to reach the detector at distance L after the time t due to diffusion. The second term $\cos(\omega_L t)$ is due to spin precession in the magnetic field and the detector electrode being sensitive to the projection of the spin polarization onto the contact magnetization direction. Spin relaxation with the spin lifetime τ_s is taken into account by the last term e^{-t/τ_s}, which effectively removes paths, much longer than $\lambda_s = \sqrt{D\tau_s}$.

Qualitatively, longer spin lifetimes lead to a higher $R_{nl}(0)$ due to the longer spin diffusion length. Further, longer spin lifetimes produce narrower curves as shown in figure 4.4 (b), since paths with longer travel times and therefore larger precession angles $\omega_L t$ have to be considered. Hence, these measurements can be employed to extract the material dependent spin relaxation time τ_s.

4.2.3 Spin Relaxation Mechanisms in Graphene

As discussed in the previous section, spin transport over long distance is limited by the finite spin relaxation time τ_s (and therefore λ_s). In graphene several possible sources for spin relaxation have been discussed in the past.

Most relevant for this work are spin relaxation mechanisms that arise due to the presence of SOC. These mechanisms also relate the spin-orbit scattering times discussed in section 4.1.3 to the corresponding SOC parameters of the material. This means that the discussed spin orbit scattering times τ_{sym} and τ_{asy} are determined by spin relaxation mechanisms that are invoked by symmetric and asymmetric SOC regarding the $z/-z$-direction, respectively. Contrary to that, τ_{sym} and τ_{asy} are not affected by non SOC related spin relaxation mechanisms, which will also be discussed in this chapter.

Elliott-Yafet Mechanism

One spin relaxation mechanism in graphene, which is a consequence of SOC, is the so called Elliott-Yafet mechanism [180, 181]. An illustration of this spin relaxation type is sketched in figure 4.5 (a).

In the presence of SOC, states with a specific spin orientation are not well defined anymore. This means that the eigenstates of the charge carriers with a specific spin direction contain an admixture of states with opposite spin direction. Then, even spin independent scattering events have a small probability to flip the electron spins. The

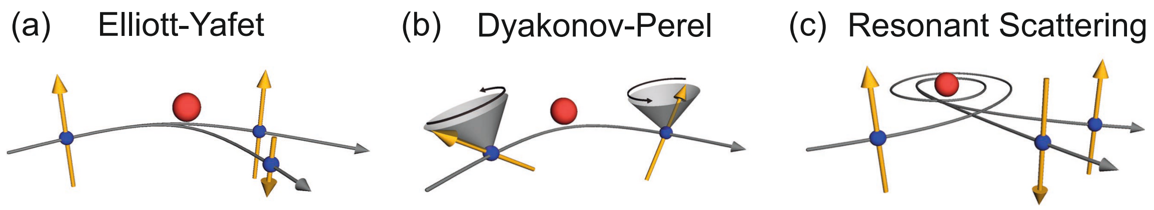

Figure 4.5: *Sketch of the most prominent spin relaxation mechanisms in graphene. (a) The Elliott-Yafet mechanism describes how scattering of electrons in the presence of SOC has a probability to flip the electron spin. (b) For the Dyakonov-Perel mechanism the spins precess in an effective magnetic field invoked by SOC. The direction of precession changes with every scattering event. (c) Resonant Scattering at magnetic moments leads to a randomization of the spins. Taken from [33].*

spin relaxation rate is therefore expected to be proportional to the rate of momentum scattering τ_p^{-1}.

It has been shown that in graphene, the spin relaxation rate due to the Elliott-Yafet mechanism is [182, 183]:

$$\tau_{s,EY}^{-1} \approx \frac{4\Lambda^2}{E_F^2}\tau_p^{-1} \tag{4.21}$$

which is independent of the specific scattering potentials and therefore of the type of scattering [183].

Elliott-Yafet spin relaxation can be caused by intrinsic as well as symmetry breaking SOC. However, intrinsic SOC only affects inplane spins giving $\tau_{s,xy}^{-1} \approx \frac{4\Lambda_I^2}{E_F^2}\tau_p^{-1}$, while $\tau_{s,z}^{-1} \rightarrow 0$ [184].

A related source of spin relaxation is Elliott-Yafet spin-flip scattering at impurities which themselves locally induce SOC. These impurities include attached heavy atoms or covalently bonded atoms such as hydrogen. In this case, equation 4.21 is no longer valid. Instead, the rate of spin relaxation by these kind of impurities is expected to be proportional to the impurity density $\tau_{s,EY}^{-1} \propto n_{imp}$ [183].

Dyakonov-Perel Mechanism

The other important spin relaxation mechanism invoked by SOC in graphene is the so called Dyakonov-Perel mechanism [185], which is illustrated in figure 4.5 (b).

As discussed in section 2.3, SOC that corresponds to breaking of inversion symmetry leads to a splitting of the energy bands with different spin polarization. Therefore the symmetry breaking SOC terms can be written as [83]:

$$H_{asy} = \frac{1}{2}\hbar\boldsymbol{\omega}_{eff}(\boldsymbol{k}) \cdot \boldsymbol{s} \tag{4.22}$$

which can be viewed as the Hamiltonian of a spin in a magnetic field. Here, $\boldsymbol{\omega_{eff}}$ is the precession frequency, corresponding to an effective internal magnetic field invoked by SOC. For spins that are not collinear with this effective magnetic field, a precession of the spins is induced.

Importantly, the direction of the effective magnetic field, with an average precession frequency $\overline{\omega_{eff}}$, is dependent on the momentum direction. This means that the precession axis changes with each scattering event. Therefore, the spins acquire an average precession angle of $\delta\varphi = \overline{\omega_{eff}}\tau_p$ before randomly changing the precession direction by a scattering event. After $N = t/\tau_p$ scattering events the standard deviation of the accumulated phase is $\varphi = \delta\varphi\sqrt{N} = \overline{\omega_{eff}}\sqrt{\tau_p t}$. The spin relaxation time is then defined as the time $t = \tau_{s,DP}$ when $\varphi = 1$, giving $\tau_{s,DP}^{-1} = \overline{\omega_{eff}}^2\tau_p$ [32, 185].

Dyakonov-Perel spin relaxation occurs only in systems with broken inversion symmetry. For Bychkov-Rashba SOC, the effective magnetic field lies in the graphene plane. Therefore, spin relaxation rates produced by the Dyakonov-Perel mechanism are different for inplane and out-of plane spins, given by [83, 182]:

$$\tau_{s,z}^{-1} = \frac{4\Lambda_{BR}^2}{\hbar^2}\tau_p, \qquad \tau_{s,xy}^{-1} = \frac{2\Lambda_{BR}^2}{\hbar^2}\tau_p = \tau_{s,z}^{-1}/2 \tag{4.23}$$

Notably, the spin relaxation rate due to the Dyakonov-Perel mechanism is proportional to the momentum scattering time τ_p. This is inverse to the relation from the Elliot-Yafet mechanism in equation 4.21. The reason for this difference is that the rotation of the spins occurs during scattering events for the Elliott-Yafet mechanism and between scattering events for the Dyakonov-Perel mechanism. In experiments, the dependence of the spin lifetime on τ_p can therefore be used to identify the dominant relaxation mechanism in graphene.

Resonant Scattering at Magnetic Impurities

Point-like defects in graphene such as vacancies or covalently bonded hydrogen atoms have been predicted [186–188] and shown experimentally [19, 189, 190] to produce local magnetic moments. During scattering at these impurities, electron spins precess around the magnetic moments which randomizes the electron spins and therefore leads to spin relaxation.

Intuitively, this effect would be expected to be very small in pristine graphene due to the scarcity of such point-like defects. However, as shown by Kochan et al., this spin relaxation mechanism is greatly enhanced if resonant scattering at these impurities is considered [8]. It has been predicted that e.g. covalently bonded hydrogen atoms induce localized electron states close to the CNP of graphene [191, 192]. If the Fermi-energy in graphene coincides with these states, the time the electrons spend in the vicinity of the impurities during scattering and therefore the interaction of the electron spin with the impurity magnetic moment is greatly increased (as sketched in figure 4.5 (c)).

Further, for this mechanism broadening of the resonance levels due to charge inhomogeneities in graphene(electron-hole puddles) and temperature has to be taken into account. This results in a different charge carrier density dependence of the spin relaxation rates for single layer [8] and bilayer graphene [193].

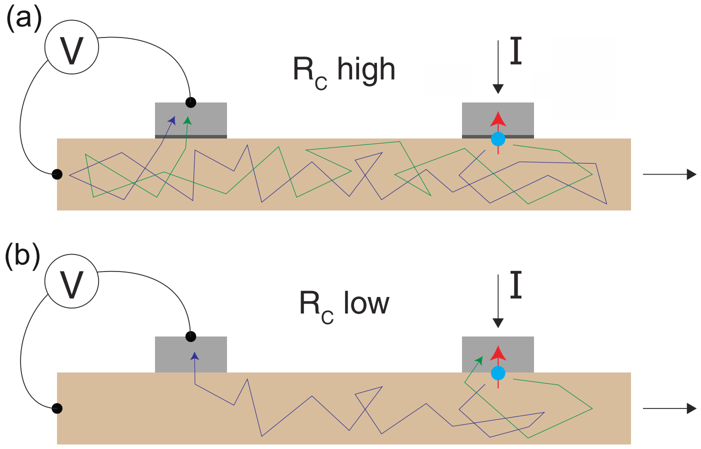

Figure 4.6: *Schematic depiction of the influence of low resistive tunneling contacts. For low contact resistance R_c in (b), the injection and detection contacts act as spin sinks. Therefore, compared to the case with high R_c in (a), the average traveling time of the injected spins is lower, which mimics a lower spin lifetime in spin injection experiments. Taken from [197].*

Other Possible Mechanisms

Hyperfine interaction of the electron spins with the nuclei is expected to be insignificant in graphene, since 99 % of natural occurring carbon atoms lack a nuclear spin [45]. Further, even in CVD graphene made entirely out of nuclear spin bearing ^{13}C-isotopes, no significant effect on spin transport of the nuclear spins could be found [194].

As pointed out by Van Tuan et al., in the presence of SOC, spin and pseudospin degrees of freedom can not be treated independently [195] (since the SOC terms in section 2.3.1 and therefore the corresponding eigenstates depend on both spin and pseudospin). This coupling can be induced by physisorbed adatoms, such as heavy metals that do not introduce significant intervalley scattering. However, concentrations of these impurities around 0.05 % are necessary to reproduce experimentally observed spin lifetimes, which is unrealistically high for the case of pristine graphene.

4.2.4 Spin Relaxation in Pristine Graphene, Hydrogenated Graphene and Graphene/TMD-Heterostructures

Pristine Graphene

Electrical spin injection and detection in graphene was first shown by Tombros et al. [196]. Here, employing the nonlocal spin-valve geometry described in section 4.2.2, Hanle-curves corresponding to spin lifetimes around $\tau_{s,xy} \approx 100$ ps have been observed. It was later realized that this low observed spin lifetime is due to poor quality of the employed AlO$_x$ tunnel barrier [197].

As discussed in section 4.2, a low contact resistance between graphene and the ferromagnetic contacts reduces the efficiency of spin injection and detection. However, as was pointed out by Maasen et al., for insufficiently resistive tunnel barriers, the ferromagnetic contacts also act as spin sinks. As depicted in figure 4.6, this predominantly removes injected electron spins with long traveling time and therefore has a similar effect on the shape of the Hanle-curves as increased spin relaxation [197, 198]. Thus, employing Hanle-measurements with low resistance tunnel barriers underestimates the observed spin lifetime [199]. Further, direct contact between graphene and the ferromagnetic material, e.g. caused by the presence of pinholes in the tunnel barrier, can also result in increased spin relaxation due to hybridization of graphene states with the ferromagnet material. Experimentally, a strong increase in the observed spin lifetimes with increasing contact resistance has been shown by Volmer et al. [200–203].

Substantially higher spin lifetimes on the order of $\tau_{s,xy} = 1-10$ ns could be observed by employing tunnel barriers made out of MgO [204–208], TiO_x [34, 209] or ultrathin hBN layers [210, 211]. However, due to the weak SOC in pristine graphene the conventionally discussed Elliott-Yafet and Dyakonov-Perel spin relaxation mechanism would result in spin lifetimes that are two orders of magnitude larger [182]. Therefore, extrinsic influences are expected to dominate spin relaxation in pristine graphene. Van Tuan et al. calculated spin relaxation due to a weak Rashba SOC in the presence of electron hole puddles due to inhomogeneities in the substrate. Here, the resulting spin lifetimes are on the same order of magnitude as the experimentally observed values [212]. However, the expected different behavior of the spin lifetimes in graphene on SiO_2 and hBN substrates is in disagreement with experimental results.

Therefore, scattering at magnetic impurities appears to be the dominant source of spin relaxation. Due to the enhancement of this type of spin relaxation by resonant scattering discussed in section 4.2.3, only very low concentrations of magnetic impurities are necessary to reproduce experimental results. Thus, good agreement with experiments for both single [8] and bilayer graphene [193] has been achieved for a concentration $n_{imp} < 0.0001\,\%$ of magnetic impurities that induce resonant scattering. Such an amount seems realistic as impurities that induce energy dissipation at a resonant energy have been found even in ultraclean graphene by using nanoscale thermal imaging [213].

One method to distinguish between different spin relaxation mechanisms is to examine the anisotropy between the out-of plane and inplane spin lifetimes $\zeta = \tau_{s,z}/\tau_{s,xy}$ by employing Hanle-measurements involving different spin polarizations. First results by Tombros et al. are limited by the small overall observed spin lifetimes, which are due to the employed AlO_x tunnel barrier, as discussed above [214]. For graphene on SiO_2, Raes et al. found $\zeta = 1$, which indicates magnetic moments to be the dominant mechanism for spin relaxation [215]. A value of $\zeta = 0.8$ obtained by Ringer et al. point towards the spin lifetimes being limited by a combination of scattering at magnetic moments and spin relaxation at Rashba fields induced by either the substrate or heavy atoms, which would correspond to $\zeta = 0.5$ [216]. Similarly for graphene encapsulated with hBN $\zeta = 0.75$ was observed, which could be decreased to $\zeta = 0.65$ by applying an out-of plane electric field, in accordance with spin relaxation by Bychkov-Rashba SOC [209].

Hydrogenated Graphene

As discussed in section 2.3.3, functionalization of graphene with covalently bonded hydrogen is expected to locally increase SOC. Further, the attached hydrogen atoms also act as resonant scatterers while inducing magnetic moments. Theoretical calculations show that spin relaxation by these magnetic moments is much more efficient than due to the enhanced SOC-strength [217]. Therefore, a decrease of spin lifetimes in hydrogenated graphene can not be taken as a sign of increased SOC.

Experimentally the effect of hydrogenation on spin relaxation was studied by Wojtaszek et al. [218, 219]. Here, an increase of the spin lifetime with hydrogenation was observed, which is in contrast to the expected mechanism of spin relaxation due to magnetic moments. However, since in this study AlO_x was employed as the tunnel barrier material, it is likely that the observed spin lifetimes are limited by the tunnel barrier quality. Therefore, the increase in the observed spin lifetime can be attributed to the change of the tunnel barrier resistance upon hydrogenation (see supplementary of [218]), similar to the behavior shown in [200].

Graphene/TMD-Heterostructures

For graphene/TMD heterostructures the strong induced SOC is expected to dominate spin relaxation over extrinsic effects. Here, Cummings et al. predicted spin relaxation to follow the Dyakonov-Perel mechanism [83]. As discussed in section 4.2.3, SOC that leads to a splitting of spin polarized bands can be written as an effective internal magnetic field. For the Graphene/TMD case described in equation 2.25, this means [83]:

$$H_{\kappa\boldsymbol{K}} = H_{orb} + \frac{1}{2}\hbar\boldsymbol{\omega}_{eff}(\boldsymbol{k}) \cdot \boldsymbol{s} \tag{4.24}$$

with:

$$\begin{aligned} \hbar\omega_x &= -2(ak\Delta_{PIA} \pm \Lambda_{BR})\sin(\theta) \\ \hbar\omega_y &= 2(ak\Delta_{PIA} \pm \Lambda_{BR})\cos(\theta) \\ \hbar\omega_z &= 2\kappa\Lambda_{VZ} \end{aligned} \tag{4.25}$$

Here, θ is the direction of k with respect to k_x and ± corresponds to the conduction and valence bands. This effective SOC-field is depicted by the red and blue arrows in figure 4.7 for different valleys $\pm\boldsymbol{K}$.

For the Dyakonov-Perel mechanism, the spin relaxation rates are proportional to a correlation time, which is a time scale on which the magnetic field changes direction. The inplane components of the effective field ω_x and ω_y in equation 4.25 correlate with the momentum scattering time τ_p, as θ changes with momentum scattering. Therefore, due to precession around this field, spin relaxation for out-of plane spins follows the expected behavior from the Dyakonov-Perel mechanism [83]:

$$\tau_{s,z}^{-1} = \frac{4(ak\Delta_{PIA} \pm \Lambda_{BR})^2}{\hbar^2}\tau_p = \tau_{asy}^{-1} \tag{4.26}$$

Contrary to that, the valley Zeeman term corresponds to a constant out-of plane effective field that has opposite direction for different valleys. Hence, the relevant correlation time for this term is the intervalley scattering time τ_{iv}. For spin relaxation

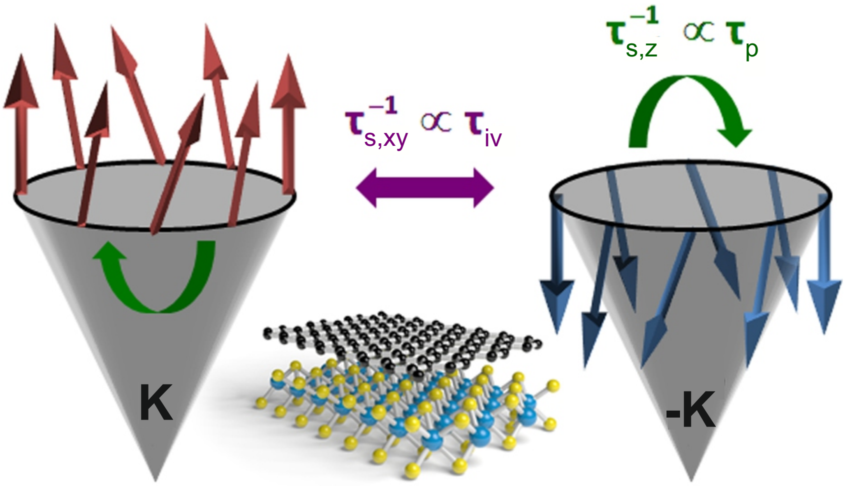

Figure 4.7: *The effective SOC-field (red and blue arrows) consists of an inplane part due to the asymmetric SOC and an out-of plane valley Zeeman part. While the inplane contribution depends on the momentum direction, the out-of plane field is constant with momentum but reverses sign between different valleys* $\pm\boldsymbol{K}$*. Therefore, the corresponding correlation times for the Dyakonov-Perel mechanism are the momentum scattering time* τ_p *for out-of plane spins and the intervalley scattering time* τ_{iv} *for inplane spins. Adapted from [83].*

of inplane spins, precession around both the inplane and out-of plane effective fields is relevant, which gives [83]:

$$\tau_{s,xy}^{-1} = \frac{4\Lambda_{VZ}^2}{\hbar^2}\tau_{iv} + \frac{\tau_{s,z}^{-1}}{2} = \tau_{sym}^{-1} + \tau_{asy}^{-1}/2 \tag{4.27}$$

The dependence of inplane and out-of plane spin relaxation on different time scales, illustrated in figure 4.7, leads to a large anisotropy of the corresponding spin lifetimes, given by [83]:

$$\zeta = \frac{\tau_{s,z}}{\tau_{s,xy}} = \left(\frac{\Lambda_{VZ}}{\Lambda_{BR}}\right)^2 \left(\frac{\tau_{iv}}{\tau_p}\right) + \frac{1}{2} \tag{4.28}$$

Spin transport experiments in graphene/MoSe$_2$ [220] and in graphene/WSe$_2$ (see supplementary of [220]) have been reported by Ghiasi et al. [220]. Here, Hanle measurements with different magnetic field directions were used to probe both inplane and out-of plane spin lifetimes. The obtained values of $\tau_{s,xy} = 3.5$ ps and $\tau_{s,z} = 40$ ps for graphene/MoSe$_2$ and $\tau_{s,xy} = 11$ ps and $\tau_{s,z} = 450$ ps for graphene/WSe$_2$. These large anisotropies of $\zeta_{MoSe_2} = 11$ and $\zeta_{WSe_2} = 40$ between inplane and out-of plane spin lifetimes are consistent with their expected dependence on different timescales. Similar measurements by Benitez et al. in graphene/WS$_2$ and graphene/MoS$_2$ provided spin lifetime anisotropies around $\zeta = 10$ [221, 222]. Further, even higher anisotropy values of $\zeta = 40 - 70$ have been found in bilayer graphene/WS$_2$ heterostructures [223].

The anisotropy observed in these spin transport experiments is comparable to the ratios between τ_{asy}/τ_{sym} found in weak antilocalization measurements in graphene/TMD-structures (see section 4.1.3). However, the spin lifetimes found in spin transport are about an order of magnitude higher than in weak antilocalization. The reason for this discrepancy is so far unclear.

4.3 Spin-Hall Effect

4.3.1 Phenomenological Description

Another consequence of strong SOC in a system are effects that lead to a conversion from charge to spin currents (and vice versa). The most prominent example of these effects is the so called spin-Hall effect (SHE) (and its inverse counterpart, the ISHE), which was first predicted by Dyakonov and Perel [224]. Phenomenologically this coupling can be described by the modified drift-diffusion equations [225, 226]:

$$\boldsymbol{j} = \boldsymbol{j}^0 + e\alpha_{SH}\mu(\boldsymbol{E} \times \boldsymbol{s}) + e\alpha_{SH}D(\nabla \times \boldsymbol{s}) \tag{4.29}$$

$$j^s_{ij} = j^{s,0}_{ij} - \hbar\alpha_{SH}\epsilon_{ijk}\left(\mu n E_k + D\frac{\partial n}{\partial x_k}\right) \tag{4.30}$$

where ϵ_{ijk} denotes the Levi-Civita symbol, $\boldsymbol{s}$ is the spin density, defined in section 4.2.2 and $\boldsymbol{j}^0$ and $j^{s,0}_{ij}$ denote the current and spin current densities without SOC. Here, j^s_{ij} describes a spin current with direction i and spin polarization j.

According to equation 4.30, the drift and diffusion parts of an electrical current generate a spin current. The strength of this effect, which corresponds to the SHE, is given by the so called spin-Hall angle α_{SH}. The ISHE, represented by the $e\alpha_{SH}D(\nabla \times \boldsymbol{s})$ term in equation 4.29, is caused by diffusion of an inhomogeneous spin density. Importantly for both effects the direction of the induced spin current, the spin current polarization and the charge current direction are all perpendicular to each other. The $e\alpha_{SH}\mu(\boldsymbol{E} \times \boldsymbol{s})$ term in equation 4.29 describes how an existing spin polarization creates a charge current through an electric field. This effect is termed the anomalous Hall-effect and can be neglected in the scope of this work.

The consequence of the SHE is depicted schematically in figure 4.8 (a). Applying a charge current through a sample will create a spin current with polarization and current direction perpendicular to the charge current direction. In a two dimensional finite sample this will result in an accumulation of out-of plane spins at the sample boundary. This accumulation causes spin diffusion away from the boundary, which counteracts the spin current from the SHE and leads to an equilibrium spin density.

The microscopic mechanisms that cause the SHE are divided into intrinsic and extrinsic mechanisms. In the context of weakly hydrogenated graphene the most relevant is the extrinsic skew scattering mechanism [227], which is analog to so called Mott scattering of electrons at atomic nuclei [228]. As illustrated in figure 4.8 (b), an electron that is scattered by a charged impurity due to SOC experiences an effective magnetic field, which depends on the orbital motion of the electron and therefore on

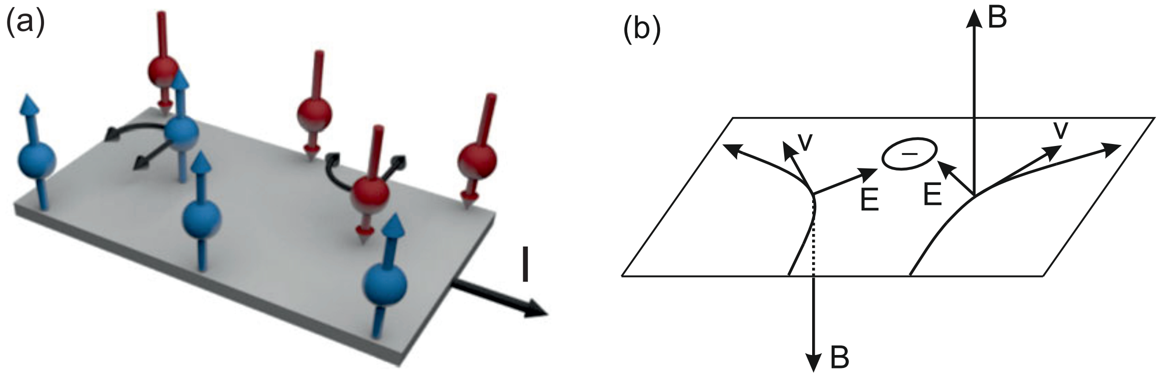

Figure 4.8: *(a) Sketch of the SHE. A charge current generates a perpendicular spin current, with the spin polarization of the spin current being perpendicular to both the charge and spin current directions. In a finite sample, this leads to an accumulation of electrons with spin up (blue) on one side of the sample and of spin down electrons (red) on the other side. Taken from [225]. (b) Illustration of the skew scattering mechanism as a source of the SHE. In the presence of SOC, an electron that is scattered by an electric charge experiences an effective magnetic field. This field is dependent on the orbital motion of the electron and acts on the electron spin. Adapted from [226].*

the scattering angle. This effective field acts on the electron spin through the Zeeman interaction, which results in a gradient of the Zeeman energy and therefore in a spin dependent force. Due to this, the scattering direction becomes weakly dependent on the spin of the scattered electron, resulting in a spin current, as described by equation 4.30.

4.3.2 SHE in Functionalized Graphene

Measurement of the SHE by the H-bar method

Measurements in hydrogenated graphene that were interpreted as stemming from the SHE were reported by Balakrishnan et al. [37, 229]. For this, they employed the so called H-bar scheme that was first proposed by Hankiewicz et al. in the context of the SHE [230]. As depicted schematically in figure 4.9 (a), this method utilizes a conjunction of the SHE and the ISHE. A charge current in one arm of a Hall-bar induces a spin current in the middle branch of the Hall-bar. Then, due to the ISHE the spin current generates a charge current in the second arm of the Hall-bar, which in an open circuit induces a nonlocal voltage.

Figure 4.9 (b) shows the corresponding nonlocal resistance ($R_{nl} = V_{nl}/I_D$ in figure 4.9 (a)) in dependence of the charge carrier density in pristine (blue curve) and hydrogenated graphene (red curve). Here, the nonlocal resistance in pristine graphene can be explained by the ohmic contribution of the current path, which follows the expected behavior shown by the gray curve in figure 4.9 (b). Contrary to that, a much higher nonlocal resistance was found in hydrogenated graphene. This was attributed

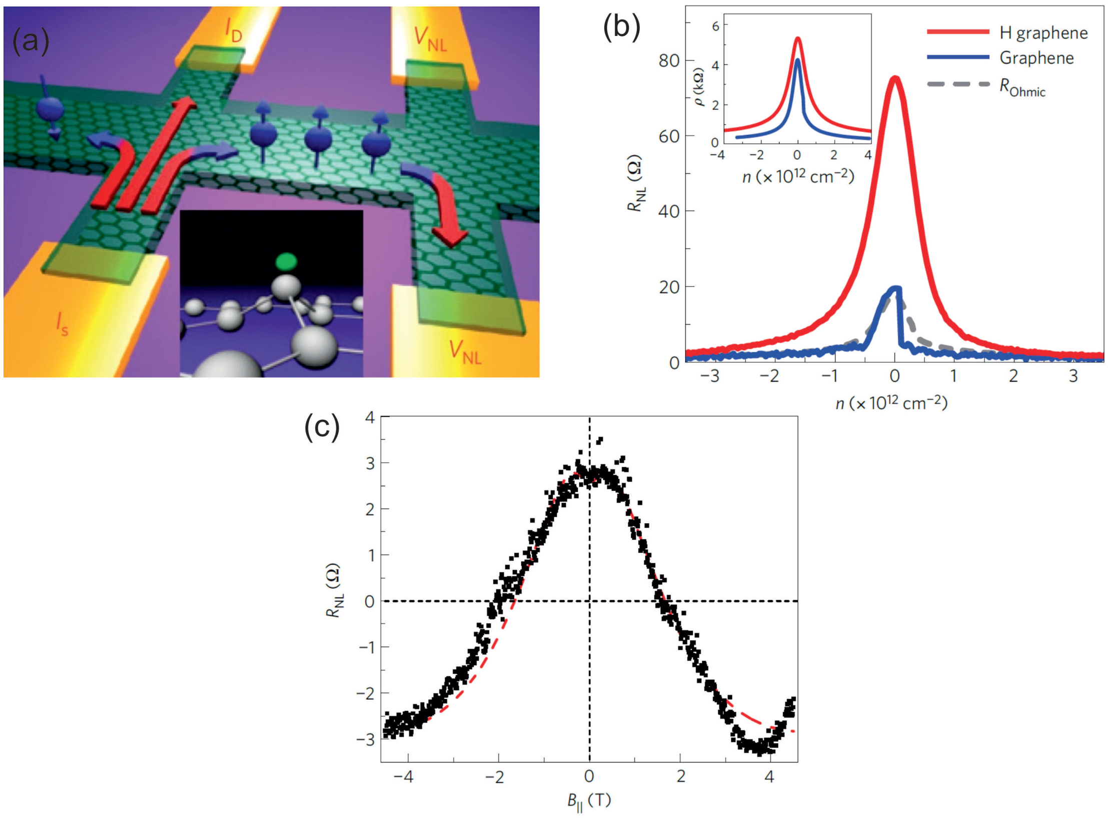

Figure 4.9: *(a) Schematic picture of the H-bar method for detecting the SHE. Through a combination of SHE and ISHE, a charge current in one arm of a Hall-bar can induce a nonlocal voltage in the other arm of the Hall-bar. (b) Comparison of nonlocal resistance in pristine (blue curve) and hydrogenated (red curve) graphene. The inset shows the resistivity of the corresponding samples. (c) Dependence of the nonlocal resistance (of a different sample than in (b)) on an inplane magnetic field. This behavior was attributed to spin precession. Taken from [229].*

to the combination of the SHE and ISHE, as discussed above. In this case the nonlocal resistance is expected to follow [231]:

$$R_{nl} = \frac{1}{2}\alpha_{SH}^2 \rho \frac{W}{\lambda_s} e^{-L/\lambda_s} \tag{4.31}$$

with W being the width of the Hall-bar and L being the distance between the injector and detector arms in figure 4.9 (a). As shown in figure 4.9 (b), Balakrishnan et al. observed a maximum of the nonlocal signal at the charge neutrality point. Assuming the SHE as the origin of this signal gives with equation 4.31 a spin-Hall angle of $\alpha_{SH} = 0.58$. This value is an order of magnitude larger than what is typically observed in heavy metals such as platinum or palladium, which are regarded as systems that show a particularly large SHE [225].

To infer on the origin of the observed nonlocal resistance, the dependence on an inplane magnetic field was investigated, which is shown in figure 4.9 (c). A spin current in the middle branch of the Hall-bar, which is generated by the SHE, has a spin polarization in out-of plane direction. Correspondingly, only a spin current with out-of plane polarization can generate a nonlocal voltage through the ISHE in graphene. Therefore, similar to the Hanle effect described in section 4.2.2, applying an inplane magnetic field leads to spin precession around the magnetic field and therefore to an oscillatory behavior of the nonlocal signal. According to Abanin et al., the nonlocal resistance is then expected to follow [231]:

$$R_{nl}(B_{||}) = \frac{1}{2}\alpha_{SH}^2 \rho W \mathrm{Re}\left\{ \frac{\sqrt{1+i\omega_L\tau_s}}{\lambda_s} \times \exp\left[-\frac{\sqrt{1+i\omega_L\tau_s}}{\lambda_s} L \right] \right\} \tag{4.32}$$

This dependence of the nonlocal resistance is depicted in figure 4.9 (c), with the red line corresponding to equation 4.32. However, it has to be noted that the measurement from figure 4.9 (c) is from a different sample than in figure 4.9 (b), where no magnetic field dependence has been shown. Further, in figure 4.9 (c) a background contribution was subtracted (see supplementary of [229] and [37]), which means that only a part of the nonlocal resistance shows the dependence on an inplane magnetic field, which is expected from the SHE/ISHE mechanism.

There has been much debate on whether the interpretation of the SHE as the origin of the nonlocal resistances is correct. Ferreira et al. calculated the effect of skew scattering in graphene in the presence of resonant scatterers, such as hydrogen atoms [227]. Although this resonant skew scattering mechanism can qualitatively reproduce the experimental results, with a maximum of the spin-Hall angle around the charge neutrality point, the magnitude of the predicted SHE is an order of magnitude lower, even for a greatly overestimated SOC-strength of $\Lambda_I = 25\,\mathrm{meV}$. Also, very similar results, meaning a large nonlocal resistance with a maximum at the charge neutrality point and a dependence on an inplane magnetic field, have been reported by the same group as in [229] for graphene decorated with heavy metals [232], fluorinated graphene [233] and graphene/TMD heterostructures [234]. While in all these systems an increased SOC can be expected, it seems unlikely that these very different systems (with regard to the origin and type of SOC) show the same behavior for the order of magnitude of the spin-Hall angle, position of the resonantly enhanced skew scattering mechanism with respect to charge carrier density, spin relaxation length and magnetic field range on which the nonlocal signal oscillates.

Moreover, investigations from Kaverzin and van Wees in hydrogenated graphene, are in disagreement with the SHE interpretation of the nonlocal signals [38]. As in [229], a large nonlocal resistance was found here. However, analysis of this signal with equation 4.31 results in an even more unrealistically high spin-Hall angle of $\alpha_{SH} = 1.5$. Further, contrary to [229], no dependence of this signal on an applied inplane magnetic field could be observed. This is shown in figure 4.10, where a large peak in the backgate dependent nonlocal resistance can be seen (red curve). However, by applying an inplane magnetic field of up to $B_{||} = 7\,\mathrm{T}$ (blue curve), no noticeable effect on this nonlocal signal can be observed.

These results indicate a non spin related origin of the nonlocal signal. Similar results (large nonlocal resistance without any inplane magnetic field dependence) have

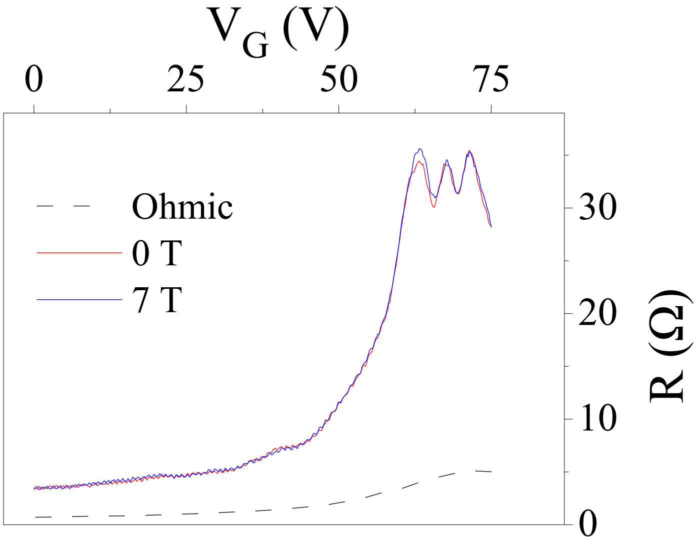

Figure 4.10: *The nonlocal resistance (red curve) measured in hydrogenated graphene far exceeds the expected ohmic contribution (black dashed curve). Upon applying an inplane magnetic field of $B_{||} = 7\,T$ (blue curve), no substantial change in the nonlocal resistance can be observed. This is a clear indication that the nonlocal signal is caused by a non spin related origin. Taken from [38].*

been found by Wang et al. in graphene decorated with heavy metals [18]. Contrary, Park et al. observed an inplane magnetic field dependence of a nonlocal resistance in graphene decorated with gold clusters [235]. However, this dependence could only be observed at a specific charge carrier density far away from the charge neutrality point and at low temperature.

A possible non spin related explanation for the inplane magnetic field dependence at low temperature could be interference effects, such as universal conductance fluctuations or weak localization. As shown in section 4.1, these effects are strongly dependent on a small out-of plane magnetic field, which can arise due to small misalignment of the sample plane with regard to the inplane magnetic field. Zihlmann observed such an inplane magnetic field dependence of the nonlocal resistance in hBN/graphene/WSe$_2$, which was identical to the dependence on an out-of plane magnetic field with much smaller magnitude [161]. Here, the alignment angle of 2.8 °extracted from this comparison was confirmed by independent measurements.

Measurement of the SHE by employing spin selective contacts

The discrepancy of the reported results of hydrogenated and otherwise functionalized graphene requires further investigation by a more definitive method for detection of the SHE/ISHE. Such a method can be to employ ferromagnetic contacts to generate a spin polarization as described in section 4.2.1. Then, a nonlocal voltage arising from a charge current induced by the ISHE can be detected by nonmagnetic contacts. This scheme, which will be discussed in more detail in section 5.3, was used by Valenzuela et al. for detection of the ISHE in aluminum wires [236].

Very recently (after publication of the results presented in chapters 5 and 6), this method has been employed to investigate spin to charge conversion effects in graphene/TMD heterostructures. Safeer et al. found an ISHE in few layer graphene/MoS$_2$ with a spin-Hall angle of $\alpha_{SH} = -0.045$ [237]. Further, in graphene/WS$_2$ both an ISHE as well as the occurrence of a spin galvanic effect were observed independently by Ghiasi et al. [238] and Benitez et al. [239]. These results are consistent with theoretical predictions for the SHE [240] and the spin galvanic effect [241] in graphene/TMD structures.

5 SOC-Effects in Weakly Hydrogenated Graphene

Hydrogenation has long been viewed as a promising possibility to alter the electronic properties of pristine graphene by functionalization [11]. Among these properties, hydrogenation has been proposed to increase the very weak SOC in graphene [35]. Consequently, reports of a giant SHE in hydrogenated graphene have received much attention [229]. However, the SHE interpretation of these measurements has been challenged by more recent experiments, which gave conflicting results in the same sample setup [38].

To solve this controversy, in this chapter, effects induced by potentially increased SOC in hydrogenated graphene are investigated. For this, first a reliable method for hydrogenation is required. Thus, plasma hydrogenation is explored in section 5.1. Here, the graphene samples were fabricated by Franz Vilsmeier and Thomas Ebnet, in the course of their Bachelor's theses [242, 243]. Further, for characterization of the samples, Raman-spectra were taken by Philipp Nagler and Tobias Korn in the group of Christian Schüller.

With this technique, a hydrogenated graphene sample in a Hall-bar configuration was fabricated and examined in section 5.2. This sample layout allows charge transport measurements for sample characterization and investigation of possible weak localization and weak antilocalization effects. Further, as discussed in section 4.3.2, this sample setup can be used to investigate nonlocal transport as a result of a possible SHE.

Additionally, a sample, which combines spin selective ferromagnetic contacts and non spin selective nonmagnetic contacts, is investigated in section 5.3. Employing the spin selective contacts, spin transport measurements in a nonlocal spin valve geometry can be performed. Further, the combination of both contact types provides an unambiguous method to examine a possible SHE in this sample.

Then, the observations concerning the occurrence of a SHE in hydrogenated graphene are discussed in section 5.4. The main results of this chapter have been published in [244].

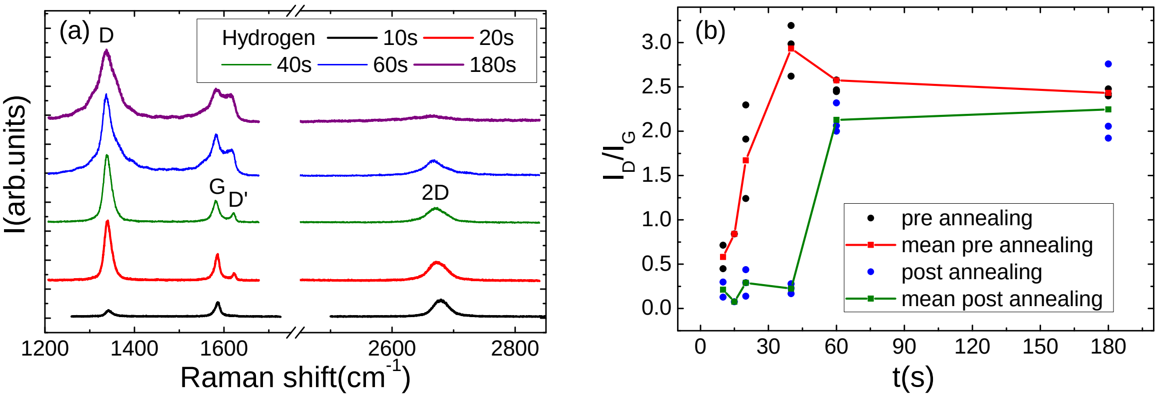

Figure 5.1: *(a) Raman-spectra of hydrogenated graphene samples for varying plasma exposure times. For increasing exposure time an increase of the D- and D'-peak intensities as well as a decrease of the 2D-peak intensity can be observed. This behavior indicates the creation of atomically sharp defects, such as bonded hydrogen atoms. (b) Evolution of the ratio between D- and G-peak intensities I_D/I_G with increasing plasma exposure time before (red curve) and after annealing at $T = 320$ °C. For low exposure times $t \leq 40$ s, annealing almost fully restores $I_D/I_G = 0$, as for pristine graphene.*

5.1 Hydrogenation of Graphene

Plasma Hydrogenation

For hydrogenation of graphene, both Balakrishnan et al. [229] and Kaverzin and van Wees [38] covered the graphene with a hydrogen silsesquioxane (HSQ)-resist, followed by electron-beam exposure (see [245]). However, as will be discussed by the end of this section, this method has severe limitations.

Therefore, in this section, hydrogenation by exposing exfoliated graphene to a hydrogen plasma in a reactive ion etching chamber (RIE) is explored. For this, a recipe developed by Wojtaszek et al. [246] was followed with a hydrogen plasma pressure of 40 mTorr, 30 sccm gas flow and 2 W power. Importantly, the power, which is the lowest value possible where plasma ignition occurs in the employed system, leads to a low acceleration bias voltage. This is expected to minimize lattice defects in graphene [21].

For investigation of the hydrogenation process, the samples were exposed to the plasma for various durations and then Raman-spectra were taken, which are shown in figure 5.1 (a). As discussed in section 3.2, the occurrence of the G and the 2D-peak is typical for graphene. With increasing plasma hydrogenation time, both a D- and a D'-peak arise. These peaks indicate the creation of atomically sharp defects. Further, for long exposure times, a decrease of the 2D-peak intensity can be observed.

The evolution of the ratio between the D- and the G-peak intensities I_D/I_G with increasing plasma exposure time is shown by the red curve in figure 5.1 (b). According to equation 3.9, for short plasma exposure times, I_D/I_G is proportional to the defect density and shows a maximum of around $I_D/I_G = 3$ for an exposure time of $t = 40$ s.

For longer exposure time, the average distance between defects becomes smaller than the distance an electron-hole pair, created in the Raman process, travels during its lifetime [111]. Then scattering at multiple defects has to be considered, which leads to a saturation of the D-peak intensity. Further, at high defect densities an alteration of the graphene band structure occurs, which reduces possible transitions [101]. Due to the 2D-peak being double resonant, it is more sensitive to this than the G- and the D-peaks. Thus, a decrease of the 2D-peak intensity in figure 5.1 (b) can be observed. Since such a high defect density also corresponds to a large amount of scattering and therefore very low electron mobility, only the lower defect density regime is relevant for the measurements in the following sections.

Importantly, the D-peak in the Raman-spectra only indicates the occurrence of atomically sharp defects, but does not reveal the type of such defects. The green curve of figure 5.1 (b) therefore shows the I_D/I_G ratios of the same samples after annealing in vacuum for one hour at $T = 320\,°\mathrm{C}$. As can be seen, for the experimentally relevant defect density range with exposure time $t \leq 40\,\mathrm{s}$ annealing almost fully removes the defects. This excludes lattice defects such as vacancies to be the origin of the observed D-peak, since the annealing temperature is too low to restore defects in the graphene lattice [247]. Since for $t > 40\,\mathrm{s}$, I_D/I_G could not be restored, it is likely that prolonged plasma exposure times generate a significant amount of lattice defects. This can possibly be caused by heating of the samples during the exposure process or by etching of the carbon atoms by hydrogen under formation of $\mathrm{CH_2}$, which might take place after the saturation of the hydrogen coverage of graphene is reached [248].

Comparison with Deuterium

Although lattice defects can be excluded to be the origin of the observed D-peak in the Raman-spectra, it is possible that this peak is due to defect sources other than hydrogen, such as contaminations in the RIE-chamber. Hence, to further determine the defect type, the same plasma process was repeated with deuterium instead of hydrogen.

Figure 5.2 (a) shows the corresponding Raman-spectra for different plasma exposure times. Compared to the hydrogenation process in figure 5.1 (a), deuterium seems to induce slightly more defects than hydrogen plasma exposure. This can be seen clearly by the faster decrease of the 2D-peak intensity in figure 5.2 (a). Possible explanations for this are a higher reactivity of deuterium due to a slightly increased binding energy [249], or an increased creation of lattice defects due to the higher mass of deuterium.

Further, graphene was exposed to either hydrogen or deuterium for $t = 20\,\mathrm{s}$ and annealed for 1 hour in vacuum at different temperatures. Figure 5.2 (b) shows the resulting I_D/I_G ratios, divided by their corresponding values before annealing. As can be seen, the attached deuterium (red dots in figure 5.2 (b)) is more stable with annealing temperature than hydrogen (black dots). The same behavior was observed for desorption of deuterium and hydrogen bonded to graphite surfaces [250]. This can be attributed to a slightly increased binding energy due to the difference in zero-point

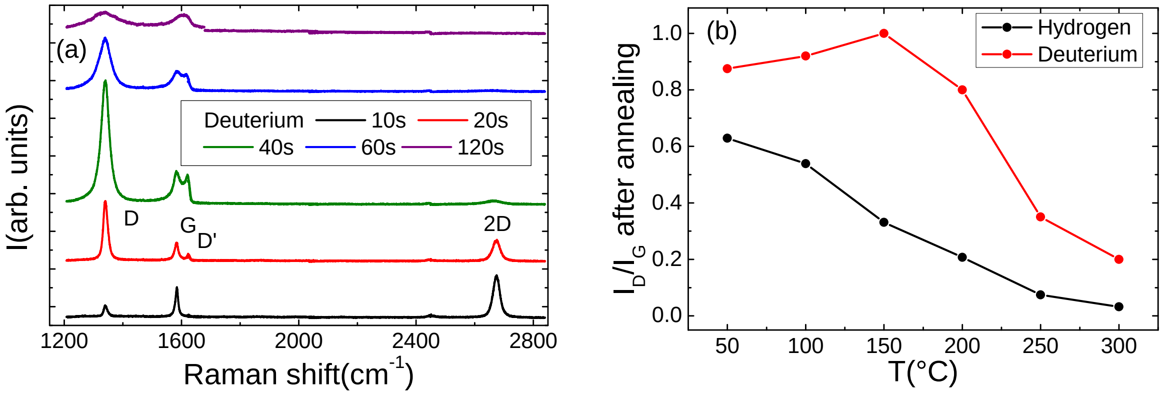

Figure 5.2: *(a) Raman-spectra for different exposure times with deuterium plasma. Compared to the hydrogenated case, a slightly increased reactivity with deuterium can be observed, as seen by the rapidly decreasing 2D-peak. (b) Relative I_D/I_G ratios for samples exposed to $t = 20\,s$ of hydrogen (black dots) or deuterium (red dots) plasma, after annealing for 1 h at various temperatures. The attached deuterium atoms are more stable with annealing temperature, confirming that the defects created during the plasma process are hydrogen (deuterium) atoms.*

energy between bonded hydrogen and deuterium [249]. Additionally, the higher mass of the deuterium compared to the hydrogen leads to a lower attempt frequency, which hinders desorption [250].

Importantly, this different desorption behavior unambiguously shows that the created defects observed as the D-peak in the Raman-spectra are indeed bonded hydrogen (deuterium) atoms, since any other kind of defect created during the hydrogen or deuterium exposure process would show the same dependence on annealing temperature.

Effect of Resist Residues

The low stability of the bonded hydrogen with respect to temperature is problematic for the sample fabrication process, since electron beam lithography (EBL) requires bake out of the EBL resist. Employing hydrogenation as the first sample fabrication step therefore results in desorption of a significant portion of the hydrogen coverage after several required EBL steps.

Using hydrogenation as the last step in sample production, however is restricted due to residues stemming from the EBL resists. The influence of such residues on the hydrogenation properties is shown in figure 5.3. Here, the black curve shows the Raman-spectrum of pristine graphene, which was exposed for $t = 20\,\mathrm{s}$ to hydrogen plasma. This spectrum gives a ratio between D- and G-peak of $I_D/I_G = 1.8$. The red (blue) curve in figure 5.3 depicts the spectrum for graphene with the same hydrogen plasma exposure time, after coating and subsequent removal of PMMA (CSAR)-resist. As can be seen, residues from these resists prevent efficient hydrogenation, resulting in a much smaller peak ratio of $I_D/I_G = 0.63$ ($I_D/I_G = 0.56$). Even an additional

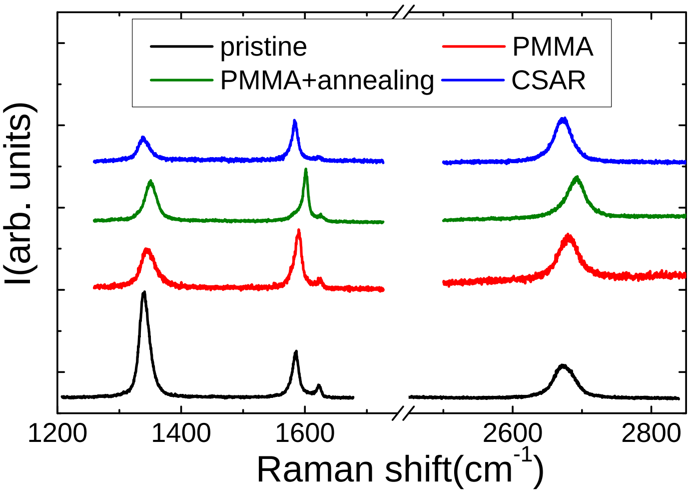

Figure 5.3: *Effect of resist residues on the hydrogenation properties. Hydrogenation of pristine graphene (black curve) results in a significantly higher D-peak intensity than for graphene that was previously coated with PMMA (red curve) or CSAR (blue curve). Annealing after resist removal produced only slightly better results.*

annealing step at 320 °C for 1 h in vacuum and 30 min in forming gas after resist removal, could not produce significantly better results as seen in the green curve in figure 5.3. Here, annealing increased the peak ratio to $I_D/I_G = 0.73$ as well as resulting in a blue shift in the peak position, likely caused by increased doping of graphene by the substrate [251].

These results suggest that resist residues that cannot be easily removed [252] restrict the hydrogenation process. Further, it is expected that these residues lead to an inhomogeneous hydrogen coverage. Thus, for the samples discussed in sections 5.2 and 5.3, hydrogenation was done as a first step in the sample production process.

Issues with Hydrogenation of Graphene by applying HSQ

As discussed before, in both the investigations of the SHE in hydrogenated graphene, hydrogenation was done by coating graphene with HSQ resist and then exposing it to a controlled electron beam dose [38, 229]. Ryu et al. showed an increase in the D-peak intensity in the Raman-spectrum with electron dose for HSQ covered graphene, while observing a decrease of the Si-H peak of the HSQ [245]. They therefore argue the generated defects indicated by the arising D-peak to be covalently bonded hydrogen atoms. A similar process was also reported by overexposing PMMA-resist instead of HSQ [253].

However, this method has several disadvantages compared to the plasma hydrogenation process discussed in this section. First, the exposed HSQ film can not be removed without destroying the underlying graphene. Therefore, hydrogenation with this method can only be employed as a last step in the sample fabrication process. However, as shown in figure 5.3, resist residues from previous fabrication steps prevent efficient hydrogenation and likely cause an inhomogeneous hydrogen coverage.

Further, both in our measurements and in the measurements by Kaverzin and van Wees (see figure 4.10), a high p-type doping was always observed in samples produced by this method. Figure 5.4 (a) shows the Raman-spectrum of a graphene sample, for which hydrogenation was done by the HSQ-method. Here, the corresponding peak

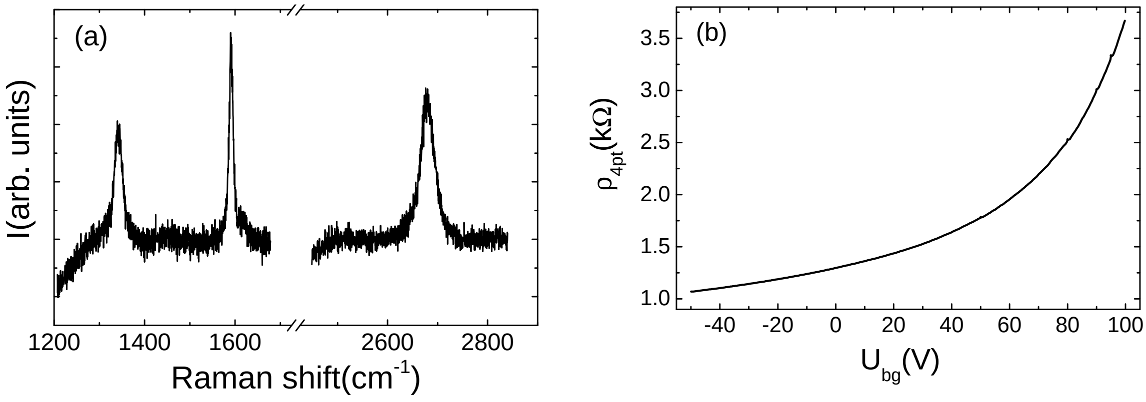

Figure 5.4: *(a) Raman-spectrum of a graphene sample, for which hydrogenation was done by e-beam exposure of HSQ resist. The observed peak ratio of $I_D/I_G = 0.56$ is comparable to the samples, hydrogenated by plasma exposure. (b) Backgate voltage dependent resistivity for the same sample. The high doping in this sample, with a position of the CNP at $U_{CNP} > 100$ V, puts the CNP out of experimental reach.*

ratio of $I_D/I_G = 0.56$ is comparable to the values from the samples investigated in sections 5.2 and 5.3, produced with the plasma hydrogenation method. As can be seen from the backgate dependence of the resistivity in figure 5.4 (b), a very high doping in this sample, resulting in a position of the CNP at $U_{CNP} > 100\,\text{V}$, which is out of reach of the experiment, can be observed. This is problematic, since as discussed in section 4.3.2, a possible very large SHE is only expected close to the CNP [227]. The high p-type doping in HSQ treated graphene is surprising, since a much weaker n-type doping in hydrogenated graphene was reported, when hydrogenation was done by employing an atomic hydrogen beam in an UHV environment [254] as well as for plasma hydrogenated graphene [255]. However, Matis et al. also observed strong p-type doping in the presence of additional adsorbates, such as water [255].

Additionally, it is not entirely clear that the defects produced by the HSQ method, which can be observed as the D-peak in the Raman-spectra, are solely bonded hydrogen atoms. Annealing of graphene, hydrogenated with the HSQ-method, has been shown to decrease the D-peak intensity, which indicates that the observed defects are not stemming from lattice defects [245]. However, the fact that the exposed HSQ can not be removed and the much higher doping observed in samples produced by this method compared to the plasma hydrogenation method, makes it likely that the exposure of the HSQ film has additional uncontrollable effects on graphene, other than hydrogenation.

5.2 Measurements in Hall-Bar Configuration

To examine charge transport properties, weak localization and the SHE with the nonlocal H-bar method in hydrogenated graphene, the sample depicted in figure 5.5 (a) was fabricated. For this, exfoliated graphene was exposed for $t = 20\,\text{s}$ to hydrogen

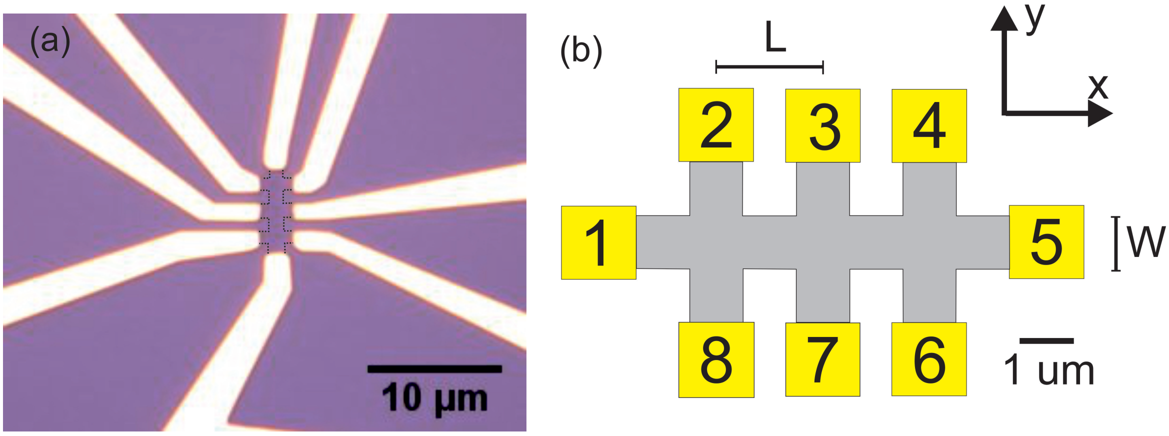

Figure 5.5: *Optical microscope (a) and schematic (b) picture of a Hall-bar sample. The graphene in (a) is marked by the dotted line.*

plasma, as described in the previous section. Then, reactive ion etching with oxygen plasma was used to define the Hall-bar shape, depicted schematically in figure 5.5 (b). Afterwards, 0.5 nm Cr and 60 nm Au were deposited for contacts.

5.2.1 Sample Characterization

Raman measurements (not shown here), taken of this sample after sample fabrication and measurements reveal a D- to G-peak ratio of $I_D/I_G = 0.43$. With equation 3.9, an excitation wavelength for the Raman measurements of $\lambda_L = 532\,\mathrm{nm}$ and $n_D(cm^{-2}) = 10^{14}/(\pi L_D^2)$ [111], this gives a defect density of $n_D = 9.5 \cdot 10^{10}/\mathrm{cm}^2$. Therefore, a corresponding hydrogen coverage (bonded hydrogen atoms per carbon atoms in graphene) of 0.0025 % can be extracted.

Here, the observed value of $I_D/I_G = 0.43$ is much lower than for the same hydrogenation recipe, employed in section 5.1, since hydrogenation was done as the first step in the sample fabrication process, which results in desorption of a part of the hydrogen coverage during the subsequent fabrication steps. However, this was preferred over using hydrogenation as the last step, since this is expected to result in a more inhomogeneous hydrogen coverage due to resist residues, as discussed in section 5.1.

Figure 5.6 shows the backgate dependent four-point resistivity of the sample depicted in figure 5.5, at the temperatures $T = 185\,\mathrm{K}$ (black curve) and $T = 1.7\,\mathrm{K}$ (red curve). As for all other measurements presented in this thesis, measurements were taken at an AC-frequency of 13 Hz. Here, a p-type doping with the position of the CNP at $U_{CNP} = 26\,\mathrm{V}$ can be observed. Further, using equation 3.5, mobilities of $\mu_h = 1400\,\mathrm{cm}^2/\mathrm{Vs}$ ($\mu_h = 1500\,\mathrm{cm}^2/\mathrm{Vs}$) for the hole side and $\mu_{el} = 1800\,\mathrm{cm}^2/\mathrm{Vs}$ ($\mu_{el} = 2000\,\mathrm{cm}^2/\mathrm{Vs}$) for the electron side at T=185 K (T=1.7 K) can be evaluated. Both doping and the relatively low mobilities are likely caused by the presence of the bonded hydrogen atoms. Such a decrease in mobility in the limit of weak hydrogenation is in accordance with previous reports [246, 256].

Figure 5.6: *Backgate dependent four-point resistivity of H-bar sample at T=185 K (black curve) and T=1.7 K (red curve). This gives a position of the charge neutrality point at* $U_{CNP} = 26$ *V indicating p-type doping and a mobility about* $\mu = 1600\ cm^2/Vs$.

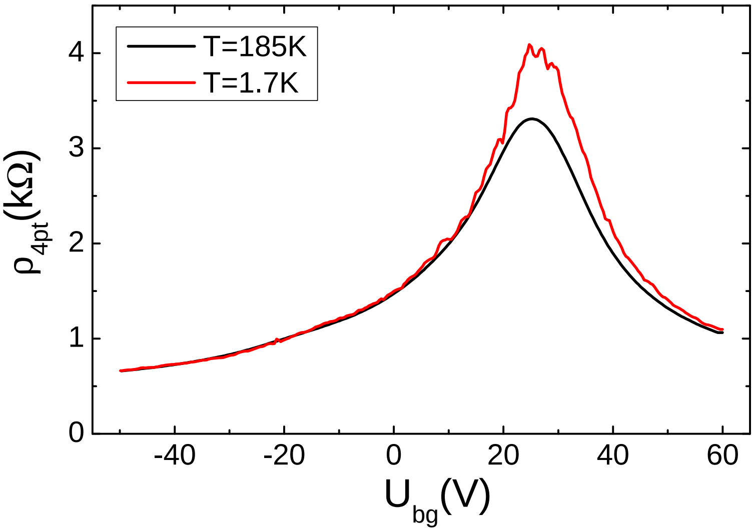

5.2.2 Weak Localization Measurements

As discussed in section 4.1, measurement of the weak localization effect can give insight into both the scattering mechanisms and potentially the strength and type of SOC in graphene samples. Figure 5.7 (a) shows measurements of the weak localization effect in the sample depicted in figure 5.5. For this, the dependence of the conductivity, measured in a four-point configuration, on an out-of plane magnetic field was taken close to the CNP (black curve in figure 5.7 (a)) as well as at $U_{bg} - U_{CNP} \approx \pm 30$ V on the hole (blue curve) and electron (green curve) sides at $T = 1.7$ K. Here, a parabolic background, which is due to positive magnetoresistance, was subtracted. Further, to suppress universal conductance fluctuations (UCF), which are prevalent at the CNP, for the black curve in figure 5.7 (a) an average over 14 curves at slightly different backgate voltages was taken (see section 6.2 for details on this procedure).

The red curves in figure 5.7 (a) represent fits of the data with equation 4.5 for the WL effect in single layer graphene. At higher charge carrier densities, values of $\tau_\phi = 10.1$ ps ($\tau_\phi = 11.8$ ps) and $\tau_i = 0.99$ ps ($\tau_i = 0.68$ ps) could be obtained for $U_{bg} - U_{CNP} = -30$ V ($U_{bg} - U_{CNP} = 30$ V). Here, the intervalley scattering length of $L_{iv} = 111$ nm ($L_{iv} = 112$ nm), which follows from the intervalley scattering time as $L_{iv} = \sqrt{D\tau_{iv}}$ (with D being obtained from equation 3.2), is lower than what is typically observed in pristine graphene [131]. This is due to strongly increased intervalley scattering at the bonded hydrogen atoms, which is in accordance with the arising D-peak in the Raman-spectrum.

Fitting the curve close to the CNP gives $\tau_\phi = 4.4$ ps and $\tau_i = 0.13$ ps, which corresponds to an intervalley scattering length of $L_{iv} = 34$ nm. The lower value of τ_ϕ close to the CNP compared to higher carrier density, is commonly observed in graphene [140] and can be explained by electron-electron interaction as the dominant mechanism for phase decoherence (see section 4.1.1). However, since the intervalley scattering length is a measure for the average distance between atomically sharp defects in graphene, L_{iv} was reported to be independent of charge carrier density in pristine

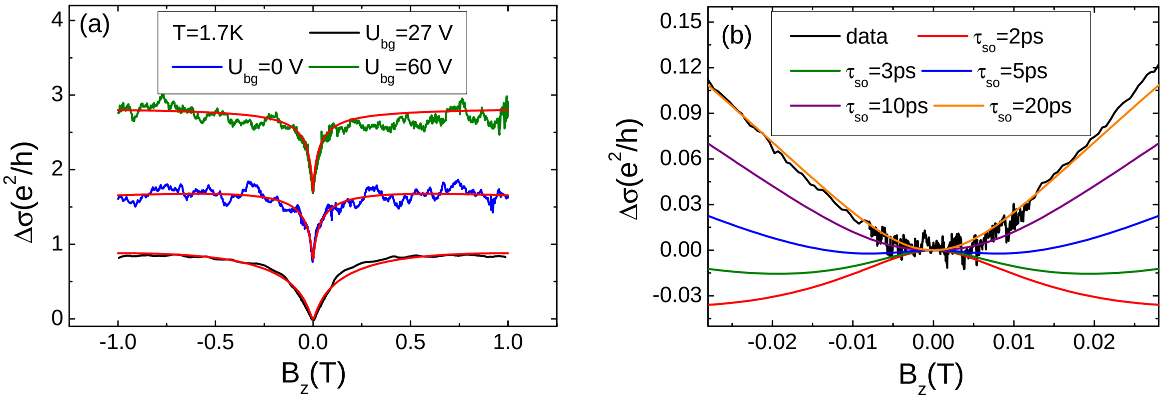

Figure 5.7: *(a) Correction to the conductivity due to the WL effect at T=1.7 K. The curves were taken close to the CNP (black curve) and at $U_{bg} - U_{CNP} \approx -30$V (blue curve) as well as $U_{bg} - U_{CNP} \approx 30$V (green curve). The red curves represent fits to the experimental data, according to equation 4.5 for WL in graphene. (b) Zoom-in to the black curve in (a) around $B_z = 0$ T. No WAL-peak as indicated by the simulated curves for various τ_{SO}, can be observed.*

graphene [140]. The lower intervalley scattering length close to the CNP, can therefore be an indication of an increased scattering cross section of the bonded hydrogen atoms due to resonant scattering, close to the CNP [191, 257].

As discussed in section 4.1.3, increased SOC in graphene due to the addition of the hydrogen atoms, can possibly result in a WAL correction to the conductivity. Figure 5.7 (b) shows a zoom-in to the black curve in figure 5.7 (a). Further, several curves with different SOC scattering times τ_{SO}, predicted from equation 4.7, are depicted in figure 5.7 (b). Here, a completely asymmetric spin-orbit coupling was assumed ($\tau_{SO} = \tau_{asy}$) and the phase coherence time $\tau_\phi = 4.4$ ps from the weak localization fit was taken. As can be seen, no WAL-peak in the conductivity around zero magnetic field can be observed. From this, a lower bound of $\tau_{SO} > 20$ ps in this sample can be obtained.

5.2.3 Nonlocal H-bar Method

Following [38, 229], the possibility of an arising SHE was investigated by employing the H-bar method, described in section 4.3.2. To this end, a charge current was applied between contacts 2 and 8 in figure 5.5 (b) and a nonlocal voltage is measured between contacts 3 and 7 and between contacts 4 and 6, respectively. The resulting nonlocal resistances in dependence of the applied backgate voltage are depicted in figure 5.8 at the corresponding distances from the current path of $L = 2\,\mu$m (figure 5.8 (a)) and $L = 4\ \mu$m (figure 5.8 (b)). Here, by decreasing the temperature from $T = 185$ K (black curves in figures 5.8 (a) and (b)) to $T = 1.7$ K (green curves in figures 5.8 (a) and (b)) a slight increase in the nonlocal resistance close to the CNP can be observed.

In this measurement configuration a small ohmic contribution to the nonlocal re-

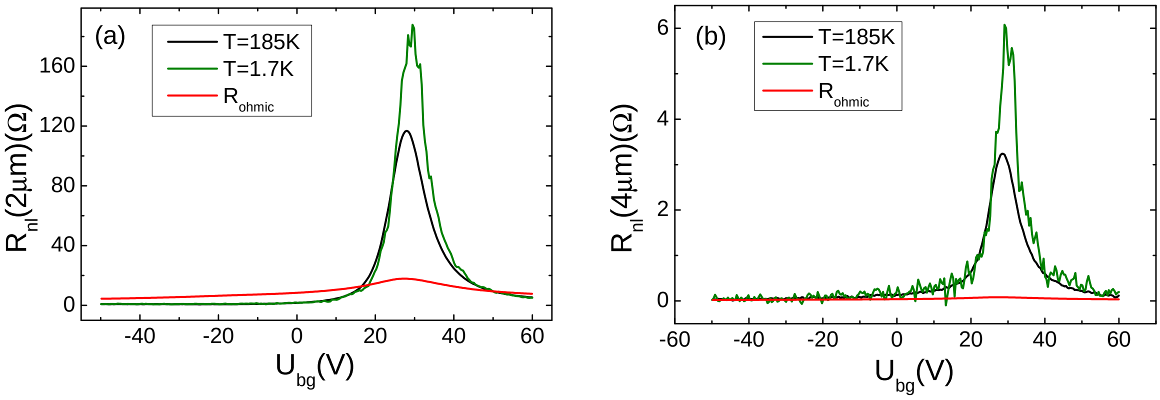

Figure 5.8: *Backgate voltage dependence of the nonlocal resistance at $L = 2\,\mu m$ (figure (a)) and $L = 4\,\mu m$ (figure (b)) distance from the current path. Close to the CNP, the nonlocal resistance, both at $T = 185\,K$ (black curves) and at $T = 1.7\,K$ (green curves), far exceeds the expected ohmic contribution (red curves).*

sistance is expected. This contribution, which is depicted as the red curves in figures 5.8 (a) and (b), is given by $R_{ohmic} = R_{2pt} \cdot G$. Here, R_{2pt} is the two-point resistance between contacts 2 and 8 and G is a geometry factor, which was determined by a finite element simulation done with COMSOL. From this, it can be seen that the measured nonlocal resistances close to the CNP by far exceed the signal, expected from a purely ohmic behavior. Further, the nonlocal resistance at distance $L = 2\,\mu\text{m}$ at high charge carrier concentration is lower than the ohmic contribution which means that the effective nonlocal resistance $R'_{nl} = R_{nl} - R_{ohmic}$ in this range is negative. A negative nonlocal resistance was also observed by Mihajlovic et al. in mesoscopic gold hall bars, which was explained by a quasiballistic effect, which however persists to a lesser degree in the diffusive regime and is caused by direct transmission of charge carriers from lead 2 into lead 7 in figure 5.5 (b) [258].

As discussed in section 4.3.2, this large nonlocal signal at the CNP might be caused by an interplay of the SHE and the ISHE. Then, the nonlocal resistance is expected to follow equation 4.31 with regard to the distance L from the current path. From this, by comparing the nonlocal resistances at the distances $L = 2\,\mu\text{m}$ and $L = 4\,\mu\text{m}$, a decay length in the range of $\lambda = 510 - 565\,\text{nm}$ can be obtained. Further, at the CNP, this relation gives a spin-Hall angle of $\alpha_{SH} = 1.3$ for $T = 185\,\text{K}$ and $\alpha_{SH} = 1.6$ for $T = 1.7\,\text{K}$. These values are unrealistically high for a possible SHE and are comparable to the value of $\alpha_{SH} = 1.5$, which was obtained by Kaverzin and van Wees [38].

For the case of the SHE as the origin of the observed nonlocal resistance, the nonlocal signal should also be sensitive to an inplane magnetic field, as this would cause Larmor-precession of the generated spin current. Figures 5.9 (a) and (b) depict the influence of such a magnetic field in x- (black curves) and y-direction (red curves), following the coordinate system in figure 5.5 (b). As can be seen from this, for both distances from the current path no dependence of the nonlocal resistance on the inplane magnetic fields can be observed.

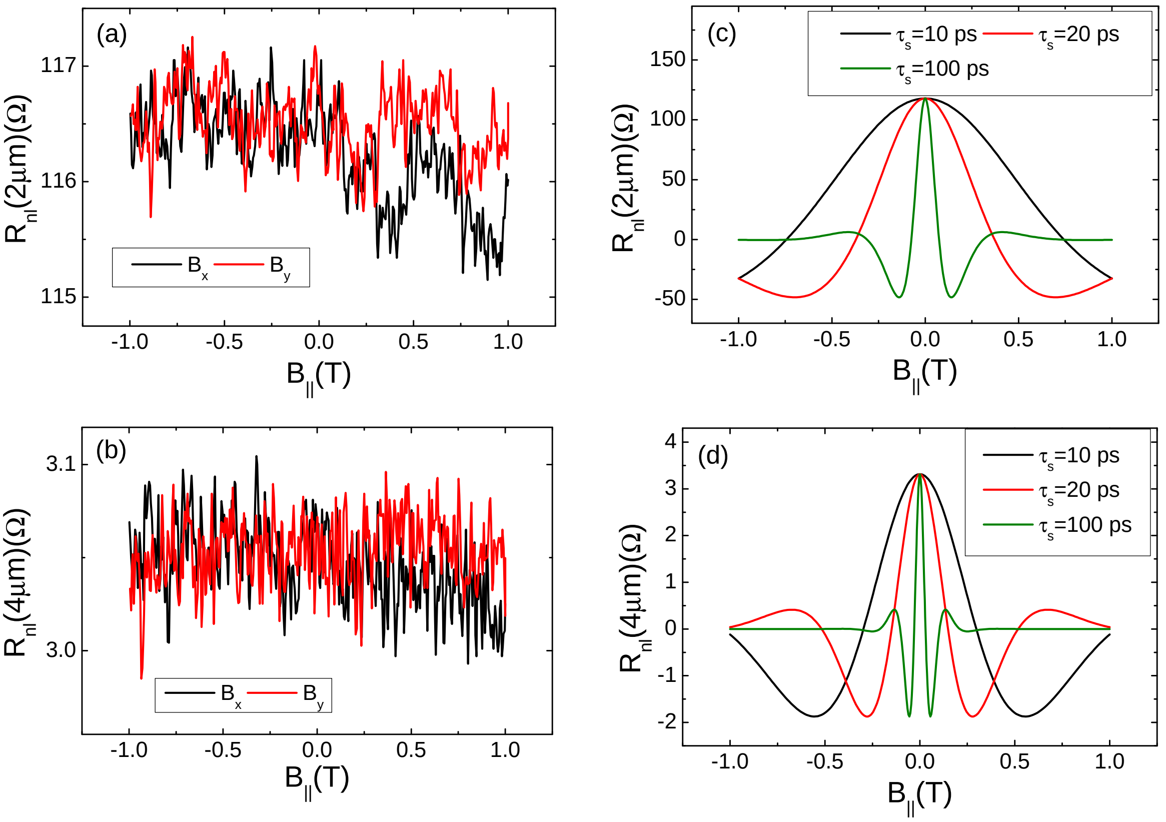

Figure 5.9: *(a) and (b) Dependence of the nonlocal resistance on an inplane magnetic field in x- (black curves) and y-direction (red curves) at the two different current paths, as for figure 5.8, at* $T = 185\,K$*. No significant effect of such a field on* R_{nl} *can be observed. (c) and (d) Expected inplane magnetic field dependence, according to equation 4.32 for different spin lifetimes* τ_s *in a realistic range. For the employed magnetic field range, a significant effect of the field on the nonlocal resistance should be observable.*

Following the SHE interpretation of the nonlocal signals, figures 5.9 (c) and (d) show the expected behavior of the nonlocal resistances at the two distances from the current path, according to equation 4.32. Here, for different spin lifetimes, a complete decay of the nonlocal signal is expected in the employed magnetic field range. The considered spin lifetimes are in a realistic range, as the absence of WAL close to the CNP shows $\tau_{SO} > 20\,\text{ps}$. A smaller spin lifetime in this sample can in principle be caused by non SOC related spin relaxation mechanisms. However, as will be shown in section 5.3.2, $\tau_s > 100\,\text{ps}$ can be found by spin injection experiments in a comparable sample. The absence of an inplane magnetic field dependence in figures 5.9 (a) and (b) of this signal is therefore a clear indication for a non spin related origin of the nonlocal resistance. A discussion of possible origins for this nonlocal signal will be given in section 5.4.

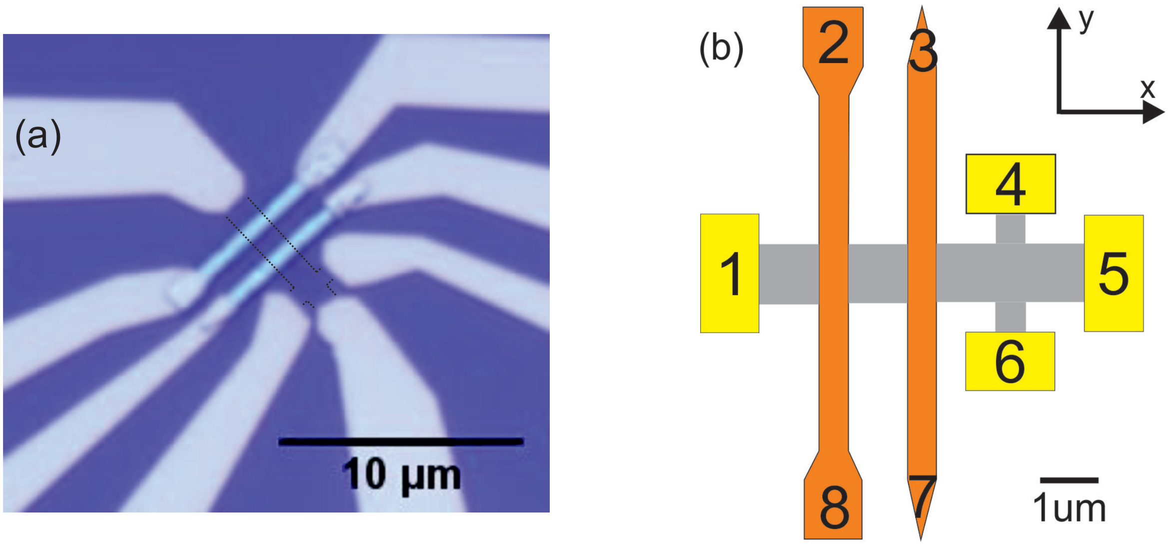

Figure 5.10: *Optical microscope (a) and schematic (b) picture of a sample utilizing ferromagnetic spin selective contacts, shown as the orange stripes in (b). The different shape of these stripes results in a different coercive field, with regard to a magnetic field in y-direction, of the two stripes. The graphene in (a) is marked by the dotted line.*

5.3 Measurements Employing Spin Selective Contacts

One shortcoming of the H-bar method is the rather indirect way a possible SHE/ISHE is examined, since for this method a charge current is applied and a resulting voltage drop due to a charge accumulation is detected. This makes this method very susceptible for possible non spin related mechanisms (see the discussion in section 5.4.2).

Therefore, to resolve the controversy regarding the giant SHE in hydrogenated graphene, a more direct way that utilizes spin selective contacts is required. To this end, the sample depicted in figure 5.10 was fabricated. Here, as for the sample in section 5.2, exfoliated graphene was hydrogenated for $t = 20\,\mathrm{s}$. Then, contacts for spin injection were fabricated (orange stripes in figure 5.10 (b)).

As discussed in section 4.2.1, to avoid the conductivity mismatch problem, a thin tunnel barrier between the ferromagnetic contact and the graphene is required. For this, 1.2 nm MgO were deposited, which was followed by 50 nm of ferromagnetic Co. Afterwards, the stripes were capped by 10 nm Au, which protects the Co stripes from oxidizing. For these spin selective contacts, all materials were deposited using e-beam (for MgO and Co) or thermal deposition (for Au) in an ultra high vacuum (UHV) system with a base pressure of $p < 10^{-10}\,\mathrm{mbar}$. Spin injection contacts, produced by the same method and in the same UHV-system, were also employed by Ringer et al. [216, 259]. More details about the fabrication process of theses spin selective contacts can be found in [260].

Following the deposition of the spin injection contacts, 0.5 nm Cr as well as 80 nm Au are deposited for nonmagnetic contacts (yellow in figure 5.10 (b)). Afterwards, the

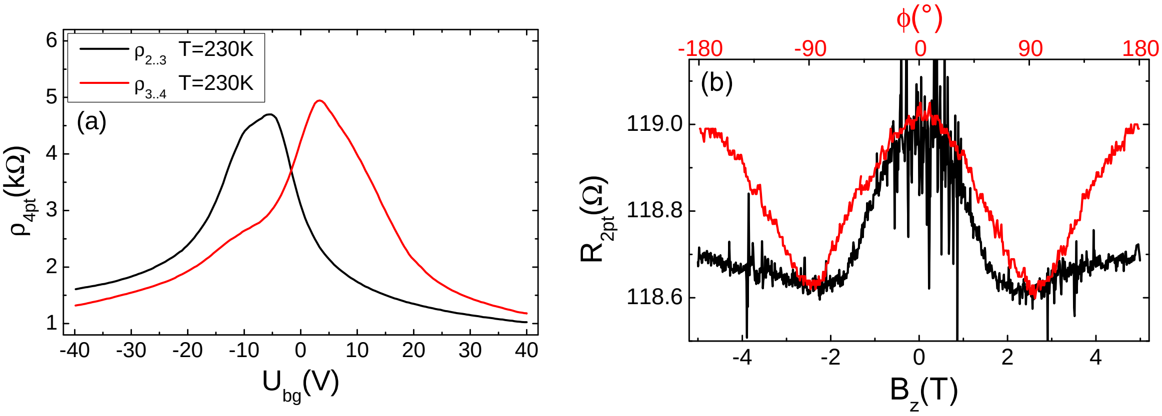

Figure 5.11: *(a) Backgate voltage dependence of the resistivity for two different regions (black and red curves) of the sample in figure 5.10. These regions show a different position of the CNP, which is likely due to a difference in doping of the areas covered by the ferromagnetic stripes and the uncovered areas. (b) Anisotropic magnetoresistance of the ferromagnetic stripe. The red curve shows the stripe resistance for an inplane magnetic field of $B = 1$ T at varying angle ϕ between magnetic field and stripe orientation. The dependence of the resistance on an out-of plane magnetic field is shown by the black curve.*

sample structure is defined by an etching step with oxygen plasma.

5.3.1 Sample Characterization

The backgate dependence of the four-point resistivity of this sample is shown in figure 5.11 (a). For this a charge current is applied between contacts 1 and 5 in figure 5.10 (b) and the voltage was taken between contacts 2 and 3 (black curve in figure 5.11 (a)) and between contacts 3 and 4 (red curve in figure 5.11 (a)). Here, a different position of the CNP can be observed for the two regions. This indicates a different amount of doping, either by the ferromagnetic contacts themselves, or by a difference in hydrogen coverage between the areas underneath the stripes and the rest of the sample. For both sample regions, mobilities of $\mu_h = 2000\,\mathrm{cm}^2/\mathrm{Vs}$ for the hole side and $\mu_{el} = 2400\,\mathrm{cm}^2/\mathrm{Vs}$ for the electron side can be evaluated by applying equation 3.5.

Another important characteristic of this sample is the magnetization behavior of the ferromagnetic stripes with an applied external magnetic field. This can be investigated by employing the anisotropic magnetoresistance (AMR) effect [261]. Due to the presence of SOC, the scattering cross section of specific electronic orbitals in a ferromagnet is anisotropic and dependent on the magnetization direction. Hence, the resistance of a ferromagnet due to the AMR effect depends on the relative orientation of the current and magnetization directions. In particular, for the utilized Co-stripes (which are likely polycrystalline), the change in resistance by the AMR-effect is expected to follow [262]:

$$R(\phi) = R_\perp + \Delta R_{AMR} \cdot \cos^2(\phi) \tag{5.1}$$

where ϕ denotes the angle between the magnetization and current directions, $R_{\perp}$ the minimum resistance for a perpendicular orientation of these directions and ΔR_{AMR} the maximum resistance change due to the AMR effect.

This effect is studied by taking the two-point resistance between contacts 3 and 7 in figure 5.10 (b). The magnetization behavior of this stripe is particularly important, since it will be used as the spin injection contact for the measurements in the following sections. However, measurements from the other stripe (not shown here) showed the same behavior regarding the magnetic field dependence of the stripe magnetization.

For the red curve in figure 5.11 (b), an inplane magnetic field of $|B| = 1\,\mathrm{T}$ is applied and rotated in the xy-plane. Here, $\phi = 0\,°$ corresponds to the magnetic field being in y-direction in figure 5.10 (b). This curve follows the $\cos^2$ dependence in equation 5.1, which shows that for the inplane magnetic field strength of $|B| = 1\,\mathrm{T}$, the stripe magnetization follows the applied field.

Further, the magnetic field dependence of the resistance of this stripe on an out-of plane magnetic field is shown by the black curve in figure 5.11 (b). For this, a linear background was subtracted. Here, it can be seen that at $B_z = 0\,\mathrm{T}$, the stripe magnetization lies in the y-direction, which results in the observed maximal resistance of the stripe. The reason for this is the shape anisotropy, which minimizes the stray field and therefore favors the magnetization to lie in stripe direction (see e.g. [262]). At higher magnetic field, the resistance decreases as the stripe magnetization rotates towards the out-of plane direction. A saturation of the resistance at $B_z = 1.8\,\mathrm{T}$ can be seen, which marks the field at which the stripe magnetization is completely aligned in the z-direction. The increase of the stripe resistance at $|B_z| > 1.8\,\mathrm{T}$ can likely be attributed to positive magnetoresistance. As will be discussed in section 5.3.3, these measurements can be employed to calculate the magnetization direction for a given out-of plane magnetic field.

5.3.2 Nonlocal Spin Transport Measurements

The sample structure in figure 5.10 (b) can also be employed for spin transport measurements. For this, a current is applied between contacts 3 and 5 and a nonlocal voltage is measured between contacts 2 and 1. According to section 4.2.1 the applied current through the injector stripe creates a spin accumulation in graphene, underneath the injector. This leads to a spin current due to spin diffusion, and the resulting spin accumulation underneath the detector stripe can be detected as a nonlocal voltage.

Nonlocal Spin-Valve

In this configuration the nonlocal spin-valve measurement described in section 4.2.2 can be carried out. Here, the magnetization of both injector and detector stripes is first aligned by a magnetic field in stripe direction of $B_y = \pm 1\,\mathrm{T}$. Then, the magnetic field is swept in the opposite direction. Due to the different shape of the two ferromagnetic stripes depicted in figure 5.10 (b), these stripes have a slightly different

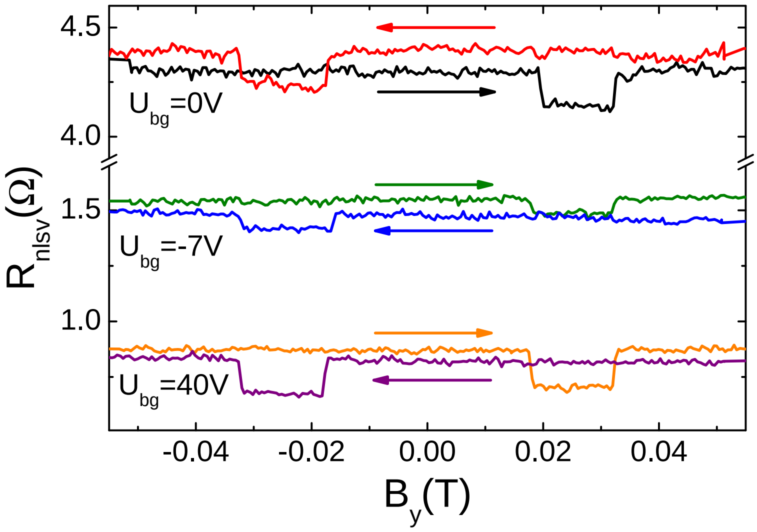

Figure 5.12: *Measurement of the nonlocal spin-valve effect at different backgate voltages. The jumps on the nonlocal resistance correspond to a switching of the configuration of the stripe magnetizations from parallel to antiparallel and back. The arrows mark the sweep direction of the applied magnetic field.*

coercive field. In particular, the stripe with the spatula-shaped tips is expected to reverse the magnetization direction at a lower magnetic field than the stripe with the sharp tips (for measurements of this difference, see [260]).

The behavior of the nonlocal resistance on this magnetic field is depicted in figure 5.12. Here, the reversal of the stripe magnetizations can be clearly seen as a jump in the nonlocal resistance. According to equations 4.18 and 4.19, the magnetic field region with a lower value of R_{nlsv}, corresponds to an antiparallel configuration of the magnetization directions of the stripes, while the field regions with the higher R_{nlsv} correspond to a parallel configuration. As can be seen the position of the jumps in the nonlocal resistance reverses sign for reversing the sweep direction, which is a clear indication of the switching of the magnetization directions of the stripes as the origin of this behavior. Importantly, this nonlocal spin-valve effect can be observed over the whole backgate range, which confirms that the ferromagnetic stripes can be employed for spin injection for the measurement of the ISHE in section 5.3.3. Further, a nonzero baseline resistance (the median of the R_{nlsv}-values for parallel and antiparallel configuration) can be observed in figure 5.12. This offset in the nonlocal resistance is likely caused by leakage charge currents through an inhomogeneous interface between graphene and the Co-stripes [263] or by the presence of thermoelectric effects [264].

Hanle Spin-Precession

Applying an out-of plane magnetic field in this configuration causes Larmor-precession of the spin current, as discussed in section 4.2.2. The dependence of R_{nlsv} on such an out-of plane magnetic field is depicted in figure 5.13. As can be seen in figure 5.13 (a), the observed signal is superimposed by a parabolic background. According to the measurements of the AMR-effect in figure 5.11 (b), at a magnetic field of $|B_z| > 1.8\,\mathrm{T}$ the magnetization of both the injector and detector stripes is expected to be fully aligned in the $\pm z$-direction. Thus, the polarization of the injected spin accumulation is in out-of plane direction and therefore does not precess in the applied magnetic field.

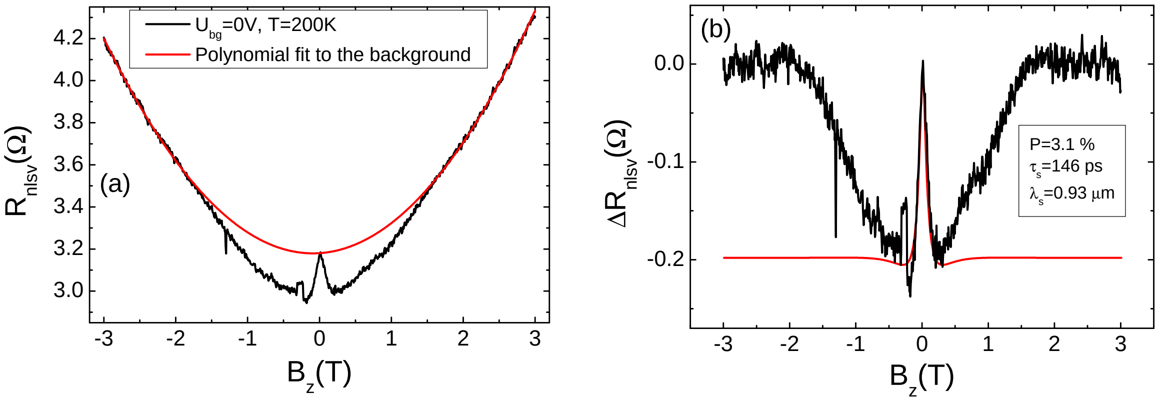

Figure 5.13: *(a) Dependence of the nonlocal resistance in the spin-valve configuration on an out-of plane magnetic field (black line). Considering the higher magnetic field range, a fit to a parabolic background can be obtained (red curve). (b) Nonlocal resistance after subtraction of the parabolic background. The low magnetic field behavior follows the Hanle-effect and can be fitted with equation 4.20. For the higher magnetic field range, R_{nl} follows the projection of the stripe magnetizations on the ±z-axis.*

Hence, no spin dependent change in R_{nlsv} is expected for the magnetic field range $|B_z| > 1.8\,\mathrm{T}$. Such a parabolic background in the nonlocal signal was also observed by Volmer et al. [202]. They attributed this to a charge current contribution in R_{nlsv} in the presence of pinholes in the tunnel barriers, which they also supported by finite element simulations, done with COMSOL.

Since this contribution has no effect on the spin dependent part of the nonlocal resistance, this parabolic background can be subtracted from the measured R_{nlsv}. The resulting spin dependent contribution to the nonlocal resistance ΔR_{nlsv} can be observed in figure 5.13 (b). In the low magnetic field range, the magnetization of the stripes can be assumed to point along the y-axis and to be stable with the applied magnetic field. The peak in the nonlocal resistance around zero magnetic field can therefore be attributed to precession of the injected spins, while traversing the sample, according to the Hanle-effect, described in section 4.2.2.

R_{nlsv} in this low magnetic field range can therefore be fitted with equation 4.20, which is shown as the red curve in figure 5.13 (b). Here, the extracted spin injection efficiency of $P_j = 3.1\,\%$ is much lower than for spin injection measurements in pristine graphene, performed with spin injection contacts fabricated by the same method [216, 259, 260]. A possible explanation for this discrepancy can be increased island growth of the MgO tunnel barrier due to the attached hydrogen. This may lead to an increase of pinholes in the tunnel barrier, which is also indicated by the relatively low contact resistance between the ferromagnetic stripes and graphene of $R_c = 1.2 - 4.2\,\mathrm{k\Omega\mu m^2}$, measured in a three-point configuration. Further, the presence of hydrogen atoms can also cause increased relaxation of the electron spins, while traversing the tunnel barrier, which can also result in a reduced spin injection efficiency.

The extracted spin lifetime of $\tau_{s,xy} = 146\,\mathrm{ps}$ is also smaller than in pristine graphene, where spin lifetimes on the order of $\tau_s = 1 - 10\,\text{ns}$ are typically observed. Regarding reported values in hydrogenated graphene, the observed spin lifetime is lower than the reported values by Wojtaszek et al. [218] but very similar to the value of $\tau_s = 200\,\text{ps}$, obtained by Balakrishnan et al. by spin-valve measurements (see supplementary of [229]).

At higher magnetic field range, due to the diffusive character of spin transport, the inplane spin polarization is completely randomized and the corresponding contribution to R_{nlsv} vanishes. Further, as mentioned above, the magnetization of both injector and detector stripes in this magnetic field range rotates into the z-direction. Then, the resulting out-of plane component of the polarization of the injected spins does not precess in the applied field. The higher magnetic field behavior of the nonlocal resistance in figure 5.13 (b) therefore follows the projection of the stripe magnetizations onto the $\pm z$-directions (R_{nlsv} is always positive for this effect, since the magnetizations of both injector and detector stripes are rotated toward the same direction). This can be confirmed by the saturation of R_{nlsv} at a magnetic field of $|B_z| = 1.8\,\text{T}$, which coincides with the value obtained by the AMR-measurements in figure 5.11 (b).

A possible way for inferring on the dominant source of spin relaxation, which was discussed in section 4.2.4, is to measure the anisotropy between the lifetimes of out-of plane and inplane spins $\zeta = \tau_{s,z}/\tau_{s,xy}$. This value can be obtained by comparing the R_{nlsv}-value at zero magnetic field, where the injector and detector magnetization lie in stripe direction, and R_{nlsv} at $|B_z| > 1.8\,\text{T}$, where the magnetizations are aligned in out-of plane direction. Since for both values no spin precession occurs, the R_{nlsv} are related to the inplane and out-of plane spin lifetimes according to equation 4.18 and $\lambda_s = \sqrt{D_s \tau_s}$. As can be seen in figure 5.13 (b), these values of R_{nlsv} are identical within the margin of error in this measurement, which indicates $\zeta = 1$, corresponding to isotropic spin relaxation.

As discussed in section 4.2.3, both Elliot-Yafet as well as Dyakonov-Perel mechanisms, induced by intrinsic or symmetry breaking SOC, generate an anisotropy in the spin relaxation rates. However, isotropic spin relaxation is expected for the resonant scattering mechanism at magnetic impurities. Since, as discussed in section 4.2.3, bonded hydrogen atoms have been shown to both induce magnetic moments in graphene [190] and cause resonant scattering [257], it seems likely that spin relaxation in this sample is dominated by this mechanism. Further, for this spin relaxation mechanism, the observed spin lifetimes are in agreement with calculations by Soriano et al., who obtained a spin lifetime on the order of $\tau_s = 100\,\text{ps}$ for a hydrogen concentration of 0.0015 % [265], which is similar to the concentration in this sample.

However, it can not be excluded that the observation of the spin lifetime, obtained in this measurement, is limited by the spin sink effect of the contacts, which was discussed in section 4.2.4. This effect can occur at pinholes in the tunnel barriers, which are likely to be present in this sample, as indicated by the relatively low contact resistance and the large parabolic background in the Hanle-measurement in figure 5.13 (a). Since this mechanism is not expected to vary for different spin polarizations, a contribution from this effect to the observed spin relaxation would also show the isotropic behavior discussed above.

The measured τ_s can therefore be taken as a lower bound for the spin lifetime in this sample. Since the same recipe for hydrogenation was employed for the sample in this section and in section 5.2, the spin lifetimes in both samples are expected to be similar. This extracted spin lifetime explains the absence of a WAL-effect in figure 5.7 (b). Here, such an effect was shown to only be observable for $\tau_{SO} < 20\,\mathrm{ps}$ in this sample, while τ_s is a lower bound for τ_{SO}, since for τ_{SO} only SOC related spin relaxation is considered. Further, the observed τ_s is clearly large enough for an expected oscillation of the nonlocal resistance in the H-bar configuration in the employed magnetic field range, as shown in figures 5.9 (c) and (d).

5.3.3 Measurements in the ISHE-Configuration

Since both spin selective and non spin selective contacts are available in the sample depicted in figure 5.10, a possible ISHE can be investigated more directly than by employing the H-bar method. For this, a charge current is applied between contacts 3 and 1 in figure 5.10 (b) and a nonlocal voltage is taken between contacts 4 and 6. In this configuration, a spin accumulation beneath the ferromagnetic injector stripe is generated, which was confirmed by the measurements in the spin-valve configuration in section 5.3.2. Then, the spin accumulation causes a spin current due to diffusion, which can then be converted into a charge current through the ISHE discussed in section 4.3. In an open circuit this charge current then corresponds to a nonlocal voltage between contacts 4 and 6 in figure 5.10 (b).

Expected Behavior from the ISHE

As discussed in section 4.3.1, for the occurrence of the SHE or ISHE, the charge current and spin current directions and the spin polarization are all required to be perpendicular to each other. As shown by the AMR-measurements in figure 5.11 (b), without an external magnetic field, the stripe magnetization and therefore the polarization of the injected spins are in stripe direction. Correspondingly, no inplane charge current generated from the ISHE, and thus no nonlocal signal is expected. However, both the measurements of the AMR- and the Hanle-effect in this sample showed that by applying an out-of plane magnetic field, the magnetization of the injector stripe can be rotated towards the out-of plane direction. This out-of plane component of the injected spin polarization then leads to a nonlocal voltage, which is expected to follow [236, 266]:

$$R_{SH} = \frac{P_j \alpha_{SH}}{2\sigma} e^{-L/\lambda_s} \sin\theta \tag{5.2}$$

with $\sin(\theta)$ being the projection of the stripe magnetization on the z-axis.

The magnetization direction of the injector stripe $\sin\theta$, evaluated by two different methods, is depicted in figure 5.14 (a). For the black curve in figure 5.14 (a), the high magnetic field behavior of the Hanle-measurement in figure 5.13 (b) is used. In this measurement the out-of plane spin dependent nonlocal resistance in the spin-valve geometry is expected to follow $R_{nlsv}(B_z) = R_{nlsv}(|B_z| > 1.8\,\mathrm{T}) \sin^2(\theta)$, since the nonlocal

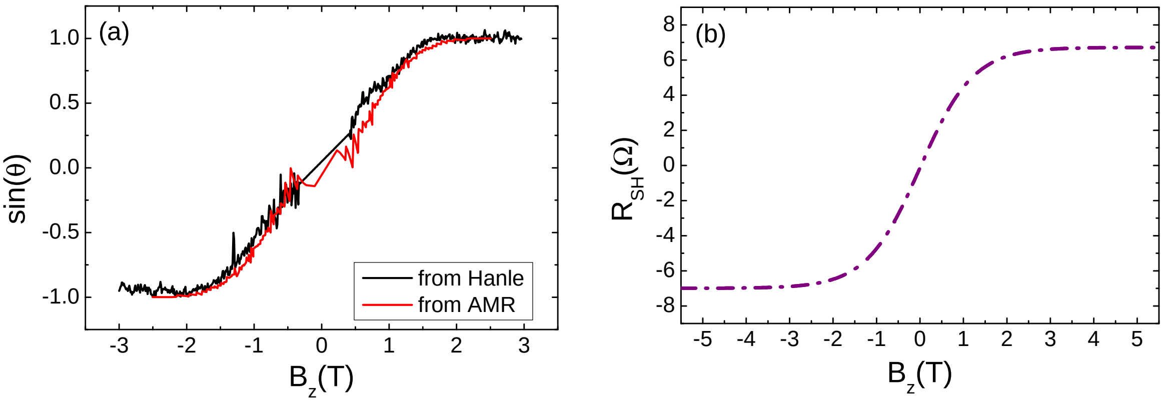

Figure 5.14: *(a) Projection of the magnetization of the injector stripe on the z-axis, determined by two different methods. For the black curve, the high magnetic field dependence of the Hanle-measurement in figure 5.13 (b) was taken. The red curve shows the magnetization dependence extracted from the AMR-measurements in figure 5.11 (b). (b) Expected nonlocal resistance, stemming from the ISHE, according to equation 5.2. Here, $\alpha_{SH} = 1$ was taken from the SHE-interpretation of the nonlocal resistance observed with the H-bar method.*

resistance depends on the projection of both injector and detector stripe magnetizations on the z-axis. The red curve in figure 5.14 (a) shows the magnetization direction, evaluated by employing the AMR-measurements in figure 5.11 (b). Here, the magnetization direction is calculated by comparing the inplane angular dependence of the AMR-effect on the stripe resistance, with the out-of plane magnetic field behavior of the AMR-effect. As can be seen, the magnetic field dependence of $\sin(\theta)$ in figure 5.14, determined by these different methods yields the same results.

Further, the magnitude of the expected ISHE can be estimated by using the nonlocal spin-valve measurements in section 5.3.2. For both the spin-valve- and ISHE-configurations, the detector areas are placed at a distance of $L = 1.5\,\mu\mathrm{m}$ from the injector stripe. Hence, combining equations 4.18 and 5.2 gives the maximum value for R_{SH} for the fully out-of plane oriented injector stripe magnetization:

$$R_{SH}(|B_z| > 1.8\,\mathrm{T}) = \frac{\alpha_{SH} W}{P_j \lambda_s} R_{nl}(0) \approx \alpha_{SH} \times 6.9\,\Omega \tag{5.3}$$

Following the SHE-interpretation of the large nonlocal resistance in section 5.2.3 gives a spin-Hall angle close to the CNP of at least $\alpha_{SH} \approx 1$. Then, combining equations 5.2 and 5.3, results in the expected magnetic field dependent ISHE signal, which is shown in figure 5.14 (b).

Measurement and Potential Origin of Nonlocal Signal in the ISHE-Configuration

The observed nonlocal resistance in the ISHE-geometry at different backgate voltages is depicted in figure 5.15 (a). Here, the expected behavior from the ISHE, shown in

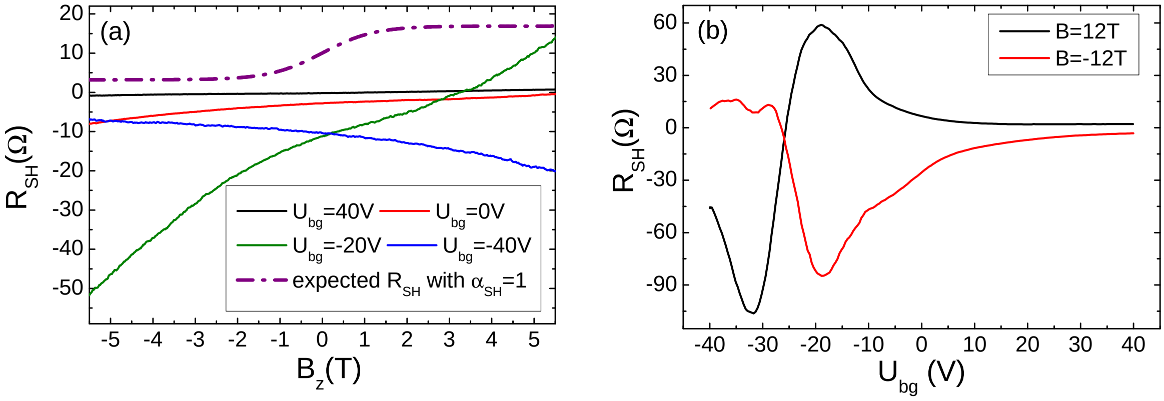

Figure 5.15: *(a) Magnetic field dependent nonlocal resistance in the ISHE-configuration at different backgate voltages. Compared with the expected curve from the ISHE (dashed purple curve), no saturation of the measured R_{SH} at high magnetic fields can be observed. (b) Backgate sweeps of R_{SH} at $B_z = 12$ T (black curve) and $B_z = -12$ T (red curve). The curves show similarities to the expected behavior for the conventional Hall-effect in graphene.*

figure 5.14 (b), is included as the dashed purple curve, where an offset was added for clarity. As can be seen in figure 5.15 (a), a large magnetic field dependent nonlocal resistance can be observed in the ISHE-configuration. However, no saturation of this signal at high magnetic field $|B_z| > 1.8$ T can be seen. Hence, R_{SH} does not follow the projection of the injector stripe magnetization on the out-of plane axis, which is expected from the ISHE-mechanism, according to equation 5.2. This behavior indicates that the observed nonlocal resistance in this measurement is not caused by the ISHE.

The magnetic field dependent nonlocal resistance in figure 5.15 (a) also differs for the applied backgate voltages. This backgate dependence of R_{SH} is depicted in figure 5.15 (b) at applied magnetic fields of $B_z = 12$ T (black curve) and $B_z = -12$ T (red curve), where the injector stripe magnetization is clearly aligned in the $z/-z$-direction. The shape of these curves shows similarities to the commonly observed behavior of the conventional Hall-effect in graphene [1]. This behavior indicates that the magnetic field dependence of the nonlocal resistance is caused by a charge rather than a spin related mechanism.

Further, a sign change of the nonlocal voltage occurs at $U_{bg} \approx -25$ V. It has to be noted that between the measurements in figure 5.11 (a) and figure 5.15, the sample was transferred from a 3D-vector cryostat with a maximum magnetic field of $|B| = 1$ T to a second cryostat with an uniaxial maximum magnetic field of $|B_z| = 14$ T. After the transfer, backgatesweeps of the sample resistivity (not shown here) showed a shift of the black curve in 5.11 (a) to a CNP at $U_{CNP} = -20$ V. The sign change of the R_{SH} in figure 5.15 (b) therefore roughly coincides with the CNP of the region beneath the ferromagnetic contacts.

As for the baseline resistance in the nonlocal spin-valve measurements in figure 5.12, the behavior of R_{SH} can be caused by leakage charge currents in the presence of an in-

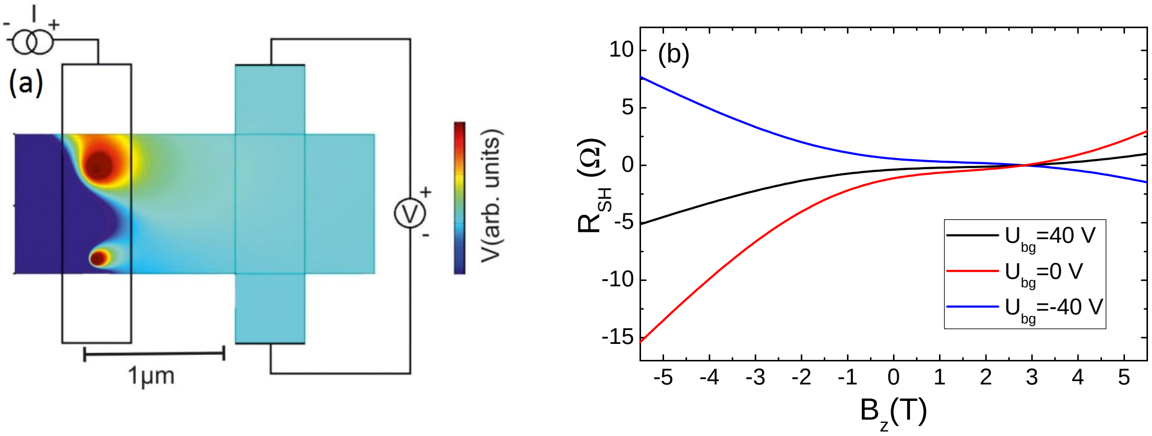

Figure 5.16: *Simulation of charge transport contribution in the inverse spin-Hall effect geometry in the presence of pinholes. (a) Potential distribution over the simulated sample in the presence of two nonequivalent pinholes. (b) Magnetic field dependent nonlocal resistance for different backgate voltages. The behavior of the simulated nonlocal resistance with regard to applied magnetic field and backgate voltages is similar to the behavior found in the experiment. Provided by Daniel Schiermeier [267].*

homogeneous tunnel barrier. Due to the relatively low contact resistance of the tunnel barriers in this sample, the presence of pinholes in the tunnel barriers is likely. To simulate the magnetic field dependence of the nonlocal resistance in the ISHE-configuration caused by charge currents through an inhomogeneous tunnel barrier, finite element simulations done with COMSOL were performed by Daniel Schiermeier [267]. For this, the employed sample design in the presence of two nonequivalent pinholes in the tunnel barrier was considered (this is similar to the calculations performed by Volmer et al. in [202]). Figure 5.16 (a) shows the potential distribution in the simulated sample, for the conducted measurement.

The corresponding nonlocal resistance in dependence of an applied magnetic field for different backgate voltages is depicted in figure 5.16 (b). Here, the CNP was set to $U_{CNP} = -20\,\mathrm{V}$. As can be seen, the simulated curves show the same general behavior as the observed nonlocal resistance in figure 5.15 (a) regarding the shape of the magnetic field dependence, the magnitude of the signal in relation to the applied backgate voltage and the sign change of R_{SH}. It is therefore likely that the observed nonlocal resistance in figure 5.15, originates from a charge current effect, caused by the presence of pinholes in the employed tunnel barrier.

Such a charge current effect can mask a potential signal caused by the ISHE in this measurement configuration. However, comparing the measurements in figure 5.15 (a) with the expected signal from the ISHE (purple curve in figure 5.15 (a)) shows that for the employed spin-Hall angle of $\alpha_{SH} = 1$, a contribution from the ISHE to the obtained signal should clearly be visible in the measurements.

The SHE interpretation of the nonlocal resistances, obtained in the H-bar method

__Figure 5.17:__ Theoretical estimation of the spin-Hall angle in hydrogenated graphene at zero temperature, in dependence of the Fermi energy position. The hydrogen concentration, employed for this calculation, is similar to the experimentally obtained values for the samples in sections 5.2 and 5.3. Data provided by Denis Kochan.

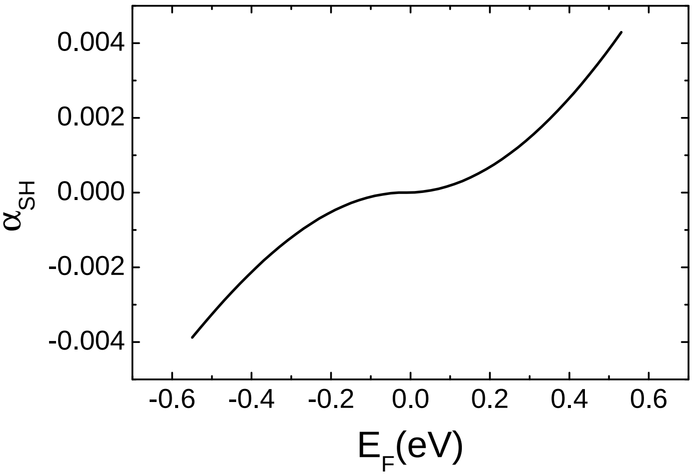

in section 5.2.3, suggests a maximum of the spin-Hall angle at the CNP. However, the backgate dependence of the resistivity in the sample, investigated in this section, showed two CNPs for two different regions in figure 5.11 (a). For the measurements in the ISHE-configuration, the relevant region is characterized by the red curve in figure 5.11 (a), since in this region the potential conversion between spin and charge currents through the ISHE occurs. Therefore, an especially large ISHE-induced nonlocal signal is expected for the red curve in figure 5.15 (a), which marks the magnetic field dependence of R_{SH}, close to the CNP $U_{CNP} = 5\,\mathrm{V}$ of the relevant sample region. As can be seen by comparing the red and purple curves in figure 5.15 (a), the obtained signal (which is likely caused by the spurious charge current effect discussed above) is much smaller in magnitude than the expected ISHE contribution. These results suggest the spin-Hall angle at the CNP to be $\alpha_{SH} \ll 1$, which is in disagreement with the SHE-interpretation of the large nonlocal resistance, observed in the H-bar method.

5.4 Discussion

5.4.1 Order of Magnitude Estimation of the Spin-Hall Angle

To obtain an estimation of the expected spin-Hall angle in the samples investigated in this thesis, Denis Kochan provided theoretical calculations concerning the skew-scattering mechanism. For this, the model described in section 2.3.3 was applied to a graphene supercell, containing one hydrogen atom and 16120 carbon atoms (for further details on the calculations see [244]). This corresponds to a hydrogen concentration of 0.0062 %, which is similar to the value of the samples, investigated in sections 5.2 and 5.3.

The resulting spin-Hall angle as a function of the Fermi energy ($E_F = 0$ corresponds to the CNP) is depicted in figure 5.17. It can be seen that the predicted value of α_{SH} is more than two orders of magnitude lower than from the SHE-interpretation of the nonlocal resistance in section 5.2.3. Such a small spin-Hall angle could be masked in the experiment by the charge current background effect, described in the previous section. Further, α_{SH} in figure 5.17 is shown to vanish at the CNP, which is also in disagreement with the behavior observed by the H-bar method.

5.4.2 Origin of Nonlocal Resistance in the H-bar Method

The absence of an inplane magnetic field dependence of the nonlocal resistance in the H-bar method in section 5.2 indicates a non spin related origin of this signal. However, the mechanism behind this large nonlocal signal close to the CNP is an open question that so far eluded the scientific community.

Valley-Hall Effect as Possible Origin of the Nonlocal Resistance

The behavior of the observed nonlocal resistance is in agreement with previous results in hydrogenated [38] and heavy atom decorated graphene [18] with regard to the magnitude, decay length λ and lack of inplane magnetic field dependence. In [18], the nonlocal resistance was ascribed to a so called valley-Hall effect (VHE). Here, similar to the SHE, described in section 4.3, a charge current generates a transverse valley polarized current, which means that electrons in different valleys flow in opposite directions [268, 269]. This valley current, which transports orbital angular momentum, is therefore neutral with regard to charge and spin (in the absence of SOC, which mixes spin and orbital momentum). In the H-bar configuration, the valley current is then transformed into a charge current by the inverse counterpart of the VHE, which can be detected as a nonlocal voltage [270].

For the occurrence of such a VHE in graphene, breaking of inversion symmetry is necessary [268]. This can be achieved by creating an asymmetry in the potential energy of the two different sublattices in graphene [271] discussed in section 2.1, and by applying nonuniform strain [272]. In the case of broken inversion symmetry, a nonzero Berry curvature is introduced close to the CNP, which is opposite for the two valleys [269]. This Berry curvature acts as a pseudomagnetic field, and similar to the Lorentz force, in the presence of an electric field causes an anomalous velocity, which is perpendicular to the electric field and therefore results in the valley polarized current in the VHE [268, 269].

A large nonlocal resistance in the H-bar configuration, arising from the interplay of VHE and inverse VHE, has been observed by Gorbachev et al. in graphene/hBN heterostructures [273]. Here, a global sublattice asymmetry in graphene is caused by the different lattice constants between hBN and graphene, resulting in a different average potential of the two sublattices [30, 274]. Similarly, a VHE has been observed in bilayer graphene, where the sublattice asymmetry is induced by the application of a transverse electric field [275, 276], which adds a sublattice dependent potential energy, according to equation 2.11.

In hydrogenated graphene, a sublattice asymmetry can be caused by preferential binding of the hydrogen atoms to different sublattices. Katoch et al. observed such a difference in hydrogen occupation between sublattices in bilayer graphene [277]. However, this is due to the different binding energy between dimer and nondimer sublattices in the top layer of bilayer graphene (see section 2.2), which was exposed to hydrogen atoms. This is contrary to single layer graphene, employed in this chapter, where no potential energy difference between the sublattices, and therefore no difference in occupation with hydrogen atoms is expected.

Along with the intrinsic VHE, induced by global breaking of inversion symmetry, also skew scattering by the bonded hydrogen atoms can be a possible source for a VHE in graphene. Asmar et al. showed that an adatom distribution, which breaks mirror symmetry (regarding the axis of incoming charge carriers), can result in a VHE, while it is absent when mirror symmetry is preserved [278]. However, it is expected that scattering off the attached hydrogen atoms is independent when the distance between these impurities is larger than the phase coherence length λ_ϕ. While λ_ϕ, extracted from the WL-measurements in section 5.2.2, is likely larger than the average distance between impurities at low temperatures of $T = 1.7\,\mathrm{K}$, this is certainly not the case at $T = 185\,\mathrm{K}$, where no WL-feature can be observed in this sample (not shown here). Then, the resulting valley currents, generated by scattering at individual impurities, are expected to average out [278]. Since the nonlocal resistance in section 5.2.3 persists up to $T = 185\,\mathrm{K}$, this mechanism can not explain the observed behavior.

It was also reported that the presence of both spin- and valley-Hall effects can lead to a suppression of the Hanle-like oscillation of the nonlocal resistance in the H-bar structure, as observed in section 5.2 [279]. However, this is only the case when the spin diffusion length is smaller than the intervalley scattering length $\lambda_s < \lambda_{iv}$. Indeed, a potential valley current in the sample is expected to decay with the intervalley scattering length λ_{iv} [270]. As discussed before, bonded hydrogen atoms act as atomically sharp narrow resonant scatterers, with a resonant level close to the charge neutrality point of graphene [191, 192]. Thus, scattering at these hydrogen atoms is expected to induce strong mixing of states from different valleys, effectively washing out the VHE. This can be seen by the occurrence of a D-peak in the Raman-spectrum of the hydrogenated samples as well as by the small intervalley scattering length close to the CNP of $\lambda_{iv} = 34\,\mathrm{nm}$, extracted from the weak localization measurements in section 5.2.2. This is in strong contrast to the decay length of $\lambda = 510 - 565\,\mathrm{nm}$, observed from the distance dependence of the nonlocal resistance in the H-bar method. This discrepancy rules out the VHE as a potential source of the observed large nonlocal signals.

Other Potential Sources for the Nonlocal Resistance

Large nonlocal resistances were observed in graphene, patterned into a periodic antidot lattice, by Pan et al. [280]. Importantly, these antidots do not induce a sublattice asymmetry or break inversion symmetry and therefore no VHE is expected. Here, it was argued that the presence of a bandgap, combined with strong intervalley scattering is sufficient to create a nonzero Berry curvature, even when inversion symmetry is conserved. The observed nonlocal resistance was therefore attributed to currents transverse to the applied external electric field due to the induced Berry curvature, as for the VHE.

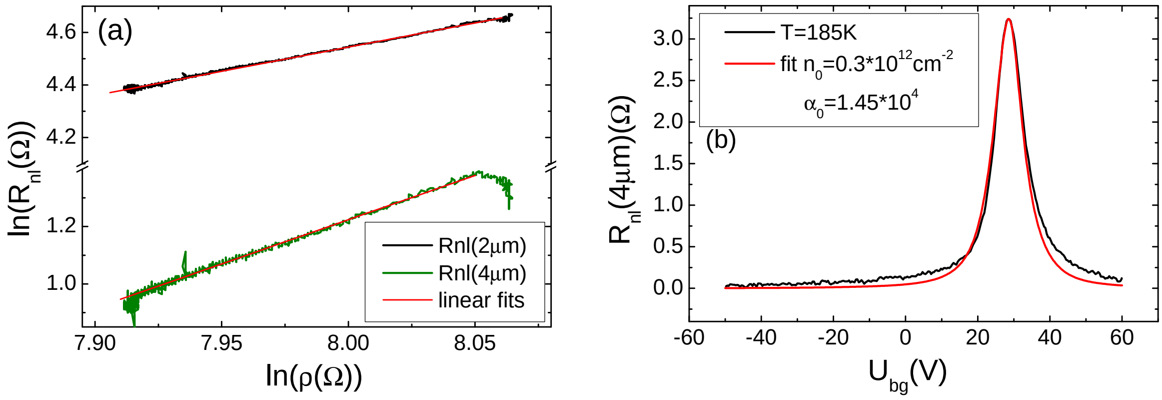

Figure 5.18: *(a) Dependence of the nonlocal resistances R_{nl} at two different distances from the current path on the sample resistivity ρ. The data was taken at varying temperatures during cooldown of the sample. (b) Fit of the backgate voltage dependence of R_{nl} at 4 µm distance with equation 5.4. While the shape of the observed curve shows good agreement with the theoretical prediction, the required coefficient $\alpha_0 = 1.45 \cdot 10^4$ is much too large to explain the measured nonlocal resistance.*

As mentioned above, strong intervalley scattering is present in the hydrogenated graphene samples. Further, for the sample discussed in section 5.2, a band gap of $E_{gap} = 0.25\,\text{meV}$ was extracted from the temperature dependence of the sample resistivity at the CNP (not shown here). The nonlocal resistance expected from this Berry curvature effect was calculated to be [280]:

$$R_{nl} = \rho^3 \left(\frac{e^2}{h}\right)^2 \frac{(E_{gap}/\hbar v_F)^2}{(E_{gap}/\hbar v_F)^2 + \pi\sqrt{n^2 + n_0^2}} \cdot \alpha_0 \tag{5.4}$$

with the Fermi velocity v_F, the charge carrier concentration n, the residual charge carrier concentration at the charge neutrality point n_0 and a coefficient α_0 that is dependent on the sample geometry and the decay length λ.

Since both the sample resistivity ρ and the observed nonlocal resistances R_{nl} in section 5.2 are temperature dependent, the dependence of R_{nl} and ρ can be extracted by varying the sample temperature. Figure 5.18 (a) shows this relation in double logarithmic representation with ρ and R_{nl} both taken at the CNP during cooldown of the sample. From this, a dependence of $R_{nl}(2\,\mu\text{m}) \propto \rho^{1.84}$ can be extracted for the nonlocal resistance at 2 µm distance from the current path and $R_{nl}(4\,\mu\text{m}) \propto \rho^{3.05}$ at 4 µm distance. While, it can be argued that more short ranged effects additionally influence the nonlocal resistance closer to the current path, the nonlocal resistance at 4 µm distance closely follows the ρ^3 dependence predicted by equation 5.4.

Thus, the charge carrier dependence of the nonolocal resistance taken at 4 µm distance form the current path can be fitted with equation 5.4. This can be seen in figure 5.18 (b), where a good agreement between measurement and theoretical prediction can be achieved with a residual charge carrier density at the CNP of $n_0 = 0.3 \cdot 10^{12}/\,\text{cm}^2$ and the coefficient $\alpha_0 = 1.45 \cdot 10^4$. However, this value for the coefficient α_0 is much larger than the expected value, which is on the order of $\alpha_0 \approx e^{-L/\lambda} = 6.9 \cdot 10^{-4}$ [280]. Therefore, the expected magnitude of this effect is 8 orders of magnitude smaller than the observed nonlocal resistance. The observed behavior can therefore not be attributed to this effect.

Considering a model with gold decorated graphene, calculations by van Tuan et al. showed a sizeable contribution to the nonlocal resistance generated by transport through evanescent waves [39] (see also [281]). This effect, which is specific to Dirac-materials [39], occurs close to the CNP [282]. However, this mechanism is only expected to have a measurable effect in geometries with $W > L$ [39]. This is contrary to the observed nonlocal resistances with $L = 2W$ and $L = 4W$ in figure 5.8.

Other mechanisms that have been reported to create large nonlocal resistances in graphene include a SHE, induced by Zeeman splitting of the conduction and valence bands close to the CNP [283, 284], and thermo-magneto-electric effects [285]. However, these mechanisms fail to explain the presence of the nonlocal resistances at zero applied out-of plane magnetic field.

Consequently, none of these previously proposed mechanisms can sufficiently explain the experimental observations of the large nonlocal resistance in the H-bar configuration. One possibility for an alternative mechanism can be enhanced charge inhomogeneity, induced by the hydrogen adatoms, which can create randomly positioned $p - n$ junctions when the Fermi energy is tuned to be close to the CNP. As has been reported, these $p - n$ junctions can guide electron paths and therefore cause a deviation from diffusive transport [286, 287], as described by the Drude model in section 3.1. Since the exact distribution of the bonded hydrogen atoms and therefore the potential landscape in the investigated samples is unknown, further experiments, potentially involving multiple scanning probe microscopy techniques as in [213, 288], are required for investigating this mechanism.

5.5 Conclusion

Several methods for investigation of SOC-effects in hydrogenated graphene have been employed in this chapter. First, plasma hydrogenation has been established as a reliable method for functionalization of graphene by covalently bonded hydrogen atoms. This process has been characterized by Raman-spectroscopy, where the occurrence of a D-peak can be seen upon hydrogenation. As discussed in section 3.2, this D-peak signals increased intervalley scattering and is therefore sensitive to atomically sharp defects such as bonded hydrogen atoms. Further, it was shown that annealing the hydrogenated graphene results in a decrease of the D-peak, corresponding to desorption of the bonded hydrogen. Importantly, graphene exposed to deuterium instead of hydrogen plasma showed a noticeable different desorption behavior with annealing temperature. This difference for these two isotopes unambiguously confirms that the atomically sharp defects, observed by the occurrence of the D-peak in the Raman-spectra, are indeed bonded hydrogen (deuterium) atoms.

With this method for hydrogenation two different sample types were investigated in this chapter. First, in a regular Hall-bar shaped sample, the weak localization effect as well as nonlocal transport in the so called H-bar configuration were investigated. In the second sample type, the combination of ferromagnetic and nonmagnetic contacts allowed the investigation of spin transport and the ISHE.

Notably, in none of these methods a drastically increased SOC, compared to pristine graphene could be observed. However, a lower bound for the spin orbit scattering time τ_{SO} can be obtained. Due to the absence of a WAL-peak at the CNP, this lower bound could be placed at $\tau_{SO} > 20\,\text{ps}$. Further, measurements of Hanle spin precession in the nonlocal spin-valve configuration show an isotropic spin lifetime of $\tau_s = 146\,\text{ps}$. Here, the observed τ_s is likely limited by spin relaxation at the magnetic moments, induced by the attached hydrogen atoms, or limited by the measurement technique, employing non ideal spin injection contacts. Thus, this measurements give a lower bound of $\tau_{SO} > \tau_s = 146\,\text{ps}$.

Concerning the SHE, measurements with both sample types have been executed to solve the controversy of previous, conflicting reports in hydrogenated graphene [38, 229]. Nonlocal measurements in the H-bar configuration showed large nonlocal resistances. However, the absence of any dependence of this nonlocal signal on an applied inplane magnetic field excludes the previously reported combination of SHE and ISHE as the source of this signal. Since no such large nonlocal resistance can be observed in pristine graphene (not shown here), the origin of this signal in hydrogenated graphene is still an open question. As discussed in section 5.4.2, none of several previously suggested mechanisms can sufficiently explain the observed nonlocal resistance. Most notably, a possible valley-Hall effect can be excluded, since the intervalley scattering length extracted by WL-measurements is more than an order of magnitude smaller than the length on which the nonlocal signal decays with regard to the distance from the current path. Therefore, any VHE would be strongly suppressed by the strong intervalley scattering at the hydrogen atoms in this sample.

Finally, measurements combining ferromagnetic and nonmagnetic contacts clearly showed the absence of a giant SHE in the hydrogenated graphene sample. This is in accordance with theoretical calculations, which place the expected spin-Hall angle into a range, which is not accessible with the sensitivity of the employed measurement.

It has to be noted that the results presented in this chapter are in complete agreement with our previous measurements in graphene, which was hydrogenated by high-dose electron beam exposure of an applied PMMA-resist [289]. Here, also a large nonlocal resistance, without any inplane magnetic field dependence was observed, while measurements combining spin selective and non selective contacts showed no measurable signal stemming from the SHE.

6 SOC-Effects in Graphene/WSe$_2$-Heterostructures

Placing graphene into contact with TMDs has been proposed as a method to drastically increase the SOC in graphene [61, 70]. Contrary to the hydrogenation method discussed in chapter 5, this method does not rely on a strong alteration of the graphene lattice, which results in additional scattering.

Further, due to the atomically flat surface of TMDs such as WSe$_2$, heterostructures containing graphene and TMDs are expected to yield high electron mobilities on the order of hBN encapsulated graphene. Therefore, in this chapter the possibility of employing the TMD WSe$_2$ to induce strong SOC in graphene while preserving the high intrinsic mobility of graphene is explored. Additionally, it is investigated whether the induced SOC-strength can be altered by applying an electric field perpendicular to the graphene surface.

To this end, multiple combinations of single layer or bilayer graphene with WSe$_2$ and hBN are investigated. A short description of the used sample fabrication methods is given in section 6.1. This is followed by investigation of the properties of a single layer graphene/WSe$_2$ heterostructure, placed onto a Si/SiO$_2$-substrate in section 6.2. Here, the electron mobility is limited by the presence of the SiO$_2$, which provides the required elastic scattering to observe phase coherent diffuse effects. Thus, the WAL-effect can be employed to investigate the properties of the SOC in graphene, induced by WSe$_2$.

Section 6.3 focuses on the possibility to tune the induced SOC in bilayer graphene/WSe$_2$ by the application of a transverse electric field. Also, this is done by analyzing the dependence of the WAL-behavior on various properties. For this section, the sample fabrication, measurements and data analysis were performed by Julia Amann in the course of her Master's thesis [290] under the author's supervision.

In section 6.4, an emphasis is put on the charge transport properties in WSe$_2$/bilayer graphene/hBN heterostructures. Also, a comparison between SiO$_2$ and WSe$_2$ as a substrate for graphene is drawn.

The main results of sections 6.2 and 6.4 have been published in [151]. As will be discussed in section 6.2.3, analysis of the WAL-effect yields a certain ambiguity, specifically in the ratio between the extracted symmetric and asymmetric spin orbit scattering times. At the time of the publication of [151], it was believed that this ratio is close to unity. This is since the relevant SOC terms are comparable in magnitude and for both symmetric and asymmetric SOC, spin relaxation is expected to be dominated by the Dyakonov-Perel mechanism. However, recent theoretical [83] and experimental [220, 221] results suggest a much larger ratio. Thus, a reevaluation of the WAL measurements in section 6.2 was required. Although, this leads to a difference in magnitude of the extracted spin-orbit scattering times, the general trends, observed in section 6.2, and the conclusions drawn from that are the same as in [151].

6.1 Sample Fabrication

For the fabrication of the samples discussed in this chapter, heterostructures containing different two dimensional materials have been assembled by applying a dry van der Waals pickup process [71]. To this end, the various materials were exfoliated onto Si/SiO_2 substrates and suitable flakes were identified by an optical microscope. Contrary to single or bilayer graphene, multilayer hBN-flakes and WSe_2-flakes have been employed. Here, hBN was exfoliated from single-crystals provided by T. Taniguchi and K. Watanabe [291], while the WSe_2 source-crystals were obtained commercially from HQ-graphene.

For the sample employed in section 6.2, single layer graphene was picked up by WSe_2, while for the samples in section 6.4, bilayer graphene was encapsulated between hBN and WSe_2. Here, the top flake of the heterostructure was exfoliated onto a thin film of polypropylene carbonate (PPC). Then, this flake was used to pick up the subsequent flakes at room temperature and the finished stack was placed onto a standard Si/SiO_2-substrate, where the conducting p^{++}-doped Si acts as a backgate in the measurements. This was followed by removing the PPC-layer in chloroform and subsequent annealing for 1 hour at 320 ° in vacuum and 1 hour at 320 ° in forming gas. This annealing step removes contaminations between the layers as well as PPC-residues on top of the stack. Importantly, with this technique only the top layer has been in contact with the employed polymer, which provides atomically clean interfaces between the different materials [292] (for a more detailed description of this transfer method see [293]).

Afterwards, the stacks were etched into Hall-bars by reactive ion etching in a CHF_3/O_2-plasma. Then, the graphene was contacted by one dimensional side contacts [71] consisting of 5 nm of Cr and 80 nm Au. Further, the samples were covered with 10 nm of Al_2O_3, which was followed by the deposition of a Au top gate. Although hBN as well as WSe_2 can sufficiently act as a topgate dielectric by themselves, the Al_2O_3 film is necessary to avoid any leakage current between the topgate and the graphene at the sides of the stack. Thus, Al_2O_3 was deposited by atomic layer deposition (ALD) at a temperature of $T = 120\,°C$, since by this method also the side surfaces of the stack are covered with the insulator.

For the sample discussed in chapter 6.3, several steps have been taken to improve the sample and contact qualities as well as the topgate stability. First, instead of the previously employed PPC-film, for this sample, a thin polycarbonate (PC)-film was placed onto a pad of polydimethylsiloxane (PDMS). Since these polymers are more stable with temperature than PPC, the stacking process can be done at an elevated temperature of $T > 100\,°C$. This process has the advantage of yielding larger contamination free areas of the heterostructures, while the subsequent annealing process can

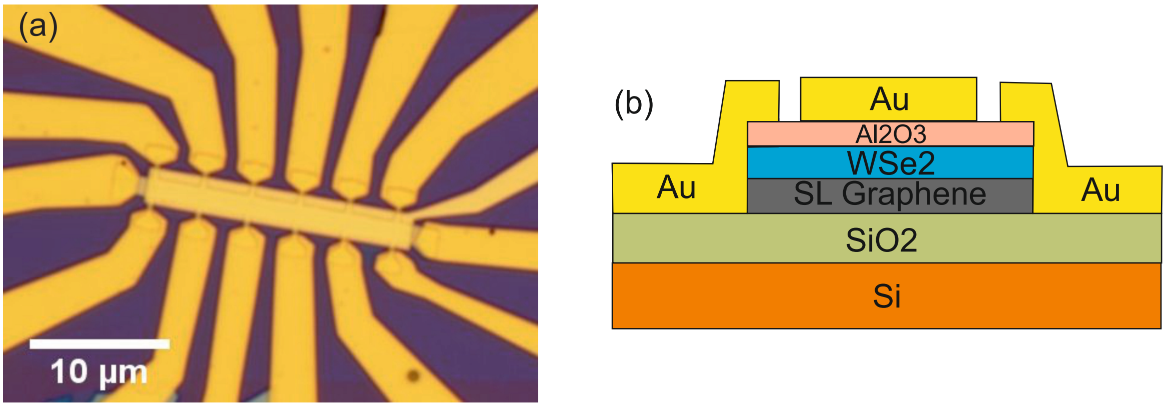

Figure 6.1: *(a) Optical microscope picture of a sample, consisting of a WSe$_2$/graphene stack. (b) Schematic cross section of the sample.*

be omitted [294].

Additionally, the one dimensional side contacts were replaced with larger areal contacts to the graphene. This was achieved by selectively etching the contact area of the top WSe$_2$ in a SF$_6$-plasma [295]. Then, the uncovered graphene was contacted by 0.5 nm Cr and 30 nm Au. Finally, the deposition of Al$_2$O$_3$ as a dielectric for the topgate was replaced by the transfer of an additional hBN-layer on top of the sample, which was followed by the deposition of a Au topgate (for details on the sample fabrication see [290]).

6.2 SL Graphene/WSe$_2$

To examine SOC in graphene induced by the proximity to WSe$_2$, the sample depicted in figure 6.1 (a) was fabricated. As can be seen in the schematic side view shown in figure 6.1 (b), this sample consists of a WSe$_2$/single layer graphene stack, which was placed directly onto a Si/SiO$_2$ substrate.

6.2.1 Sample Characterization

The presence of both a top- and a backgate allows to independently vary the charge carrier concentration and the applied transverse electric field in this sample, according to equations 3.6 and 3.7. This can be seen in figure 6.2, where the backgate voltage dependence of the sample resistivity is shown for different topgate voltage values.

Here, the position of the CNP is a function of both applied gate voltages. From this relation, the topgate capacitance C_t can be calculated with the value $C_b = 1.2 \cdot 10^{-4}\,\mathrm{As/Vm^2}$ for the backgate. It has to be noted that the presence of a transverse electric field is not expected to influence the resistivity of single layer graphene. The smaller value of the maximum resistivity at the CNP with topgate voltage $U_{tg} = -4\,\mathrm{V}$ (black curve in figure 6.2), compared to the value at $U_{tg} = -2\,\mathrm{V}$ is therefore likely due to the Fermi energy in the WSe$_2$ layer moving out of the bandgap. Further,

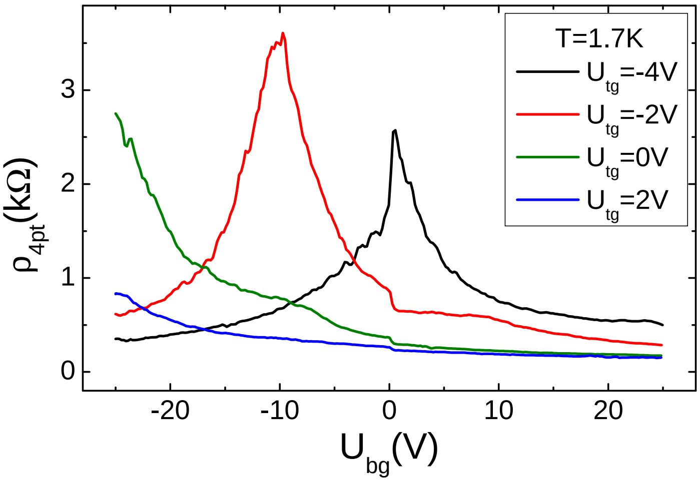

Figure 6.2: *Backgate voltage dependence of the sample resistivity for different applied topgate voltages. The position of the CNP with regard to the backgate voltage changes with applied applied topgate voltage. From the curves, a mobility of $\mu = 12000\,cm^2/Vs$ can be obtained.*

no absolute values for the applied transverse electric field can be calculated for given values of back- and topgate voltages. A more detailed discussion on the calculation of the applied field and charge carrier density will therefore be given in section 6.3, where a transverse electric field induces a bandgap in bilayer graphene and can therefore be investigated by gatesweeps.

From the curves in figure 6.2, a mobility of $\mu = 12000\,\mathrm{cm^2/Vs}$ can be extracted. This value is comparable to the mobility usually observed in graphene on SiO$_2$ and is therefore likely limited by the presence of the SiO$_2$ substrate (for the influence of the WSe$_2$ layer on the mobility of graphene see section 6.4).

6.2.2 Contributions to the Magnetoconductivity

Universal Conductance Fluctuations

To examine the WAL-effect in this sample, the dependence of the sample conductivity on an out-of plane magnetic field in a low magnetic field range is investigated. Figure 6.3 (a) shows magnetic field sweeps at slightly different charge carrier concentrations, with $\Delta n = 0.015\cdot 10^{12}/\mathrm{cm}^2$ between the curves. Here, a peak in the conductivity around $B_z = 0\,\mathrm{T}$ can be observed in all curves, according to the WAL-effect discussed in chapter 4.1.3. However, in all curves fluctuations of the conductivity, which are dependent on magnetic field strength and charge carrier concentrations, can be seen. These fluctuations are termed universal conductance fluctuations (UCF) and are commonly observed in graphene samples, when the phase coherence length is longer or on the same order of magnitude as the sample dimensions $\lambda_\phi \geq W, L$ [141, 296].

Similar to the WL/WAL-effect, UCFs result from interference of different electron paths, while traversing the sample [91]. Consequently, the UCF interference pattern can be altered by applying a magnetic field, which induces an additional phase to the interference condition, or by changing the charge carrier density, which changes the Fermi wavelength of the electrons. Further, both the magnitude and the correlation magnetic field (the applied out-of plane magnetic field on which the conductivity

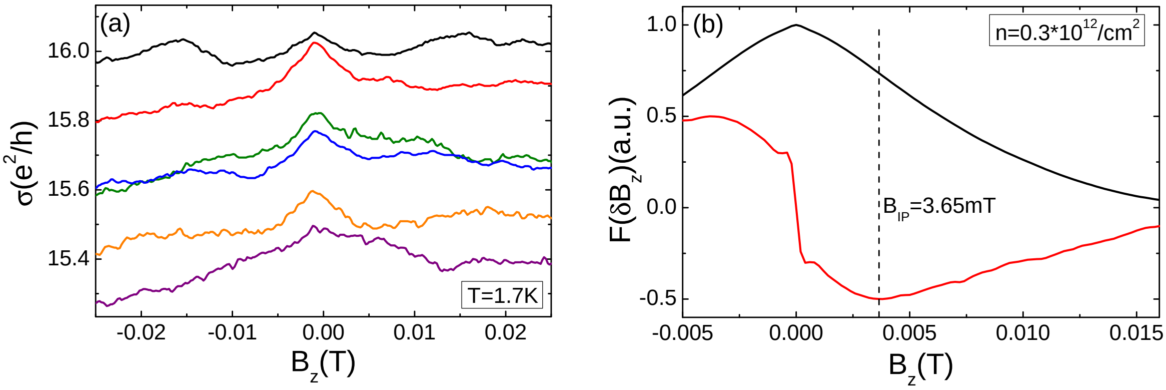

Figure 6.3: *(a) Out-of plane magnetic field dependence of the sample conductivity at slightly different charge carrier concentrations around $n \approx 0.3 \cdot 10^{12}/cm^2$. While a WAL-peak around $B_z = 0$ T can be observed in all curves, these are superimposed by gate dependent UCFs. (b) The autocorrelation function (black curve) of magnetic field sweeps can be used to analyze the UCFs. The inflection point $B_{IP} = 3.65\,mT$, determined by taking the minimum of the derivative (red curve), reveals a phase coherence time of $\tau_\phi = 6.9\,ps$.*

changes due to UCFs) of the UCFS are dependent on the phase coherence time τ_ϕ in the sample [297]. Hence, analysis of the UCFs can be used to infer on τ_ϕ for a specific charge carrier density n.

To this end, the autocorrelation function $F(\delta B_z)$ of the magnetic field dependent conductance curves at $n = 0.3 \cdot 10^{12}/\mathrm{cm}^2$ is depicted by the black curve in figure 6.3 (b). It has been shown by Lundeberg et al. that the most robust way, with regard to potential sources of error, to determine τ_ϕ from UCFs is to take the inflection point B_{IP}, which is the minimum of the derivative of $F(\delta B_z)$ (red curve in figure 6.3 (b)) [298]. Then, τ_ϕ can be determined by [141, 298]:

$$\tau_\phi^{-1} \approx \frac{2DB_{IP}}{3\hbar} \tag{6.1}$$

Thus, from the value of $B_{IP} = 3.65\,\mathrm{mT}$ in figure 6.3 (b), a phase coherence time of $\tau_\phi = 6.9\,\mathrm{ps}$ can be extracted at $n = 0.3 \cdot 10^{12}/\mathrm{cm}^2$. It has to be noted that the jump in the red curve in figure 6.3 (b) at $B_z = 0\,\mathrm{T}$ is due to the sweep rate of the magnetic field of $\Delta B_z = 0.2\,\mathrm{mT}$ in the measurements in figure 6.3 (a). This measurement resolution also limits the evaluation of UCFs at higher charge carrier densities $n > 0.3 \cdot 10^{12}/\mathrm{cm}^2$, since both D and τ_ϕ increase with charge carrier density, which reduces B_{IP}, according to equation 6.1.

Parabolic Background

In addition to the occurrence of UCFs, a small parabolic background can be observed in the curves in figure 6.3 (a). It has been shown that this background has a strong influence on the spin-orbit scattering times, obtained from fitting the WAL peaks [153].

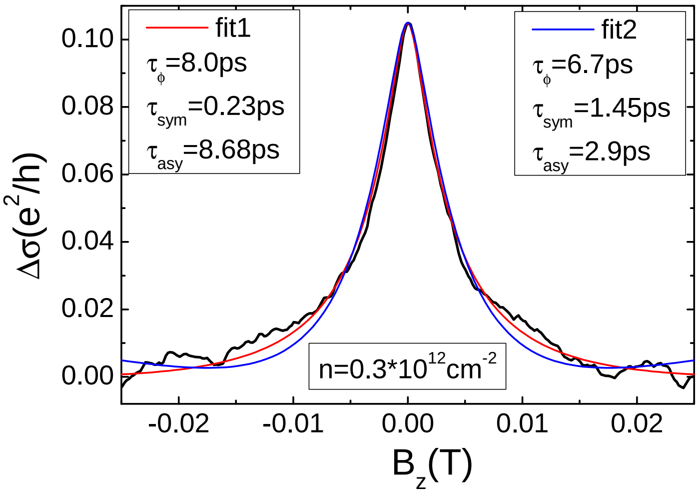

Figure 6.4: *Magnetoconductivity (black curve) averaged over 20 curves, after subtraction of a parabolic background, which was obtained from the high magnetic field behavior of the conductivity. Fits of the conductivity with the formula for the WAL-effect in equation 6.2 and two different sets of parameters are shown as the red and blue curves.*

To remove this background, in previous studies the magnetic field dependent conductivity at higher temperatures of $T = 30\,\mathrm{K}$, where no WAL can be observed any more, was subtracted from the low temperature behavior [153, 160]. However, as WL-studies in graphene show, contributions to the WAL-behavior can still be present at this temperature [143].

Therefore, for the WAL-curves in this chapter, a parabolic background was obtained from the higher magnetic field range of $B_z = -1\,\mathrm{T}$- $1\,\mathrm{T}$ in single magnetic field sweeps. Then, this background was subtracted from the low magnetic field curves in the following sections. Additional contributions to the background from ballistic boundary scattering (see section 6.4) as observed in [153], can not be removed by the process employed here. However, these effects are disregarded due to the lower mobility and following mean free path in this sample and the sample in section 6.3.

6.2.3 Fitting Procedure of Weak Antilocalization Peaks

To suppress UCFs in the magnetoconductivity, an average of 15 to 30 curves at slightly different charge carrier densities has been taken for all WAL-curves in sections 6.2 and 6.3 (see [152] for a discussion on the effect of this ensemble averaging method). The resulting magnetic field dependence of the sample conductivity at an average charge carrier density of $n = 0.3 \cdot 10^{12}/\mathrm{cm}^2$ (obtained from simultaneous measurement of the Hall-resistance R_H) is shown in figure 6.4. Here, a clear peak in the conductivity around $B_z = 0\,\mathrm{T}$ can be observed.

To extract the spin orbit scattering times in graphene, the WAL-behavior is commonly fitted with equation 4.7 (see e.g. [152–154]). This formula was derived in the limit of strong intervalley scattering with $\tau_{iv} < \tau_{SO}$ [149]. Such a strong intervalley scattering would certainly result in the occurrence of a D-peak in Raman-measurements. However, in graphene/TMD heterostructures no such D-peak could be found in [299].

For a moderate amount of intervalley scattering $\tau_{iv} \approx \tau_{sym}, \tau_{asy}$, equation 4.7 has to be modified to (see supplementary of [160]):

$$\Delta\sigma(B) = -\frac{e^2}{2\pi h}\Bigg[F\left(\frac{\tau_B^{-1}}{\tau_\phi^{-1}}\right) - F\left(\frac{\tau_B^{-1}}{\tau_\phi^{-1}+2\tau_{asy}^{-1}}\right) - 2F\left(\frac{\tau_B^{-1}}{\tau_\phi^{-1}+\tau_{asy}^{-1}+\tau_{sym}^{-1}}\right)$$
$$-F\left(\frac{\tau_B^{-1}}{\tau_\phi^{-1}+2\tau_{iv}^{-1}}\right) + F\left(\frac{\tau_B^{-1}}{\tau_\phi^{-1}+2\tau_{iv}^{-1}+2\tau_{asy}^{-1}}\right) + 2F\left(\frac{\tau_B^{-1}}{\tau_\phi^{-1}+2\tau_{iv}^{-1}+\tau_{asy}^{-1}+\tau_{sym}^{-1}}\right)\Bigg] \tag{6.2}$$

The dependence of the conductivity correction due to the WAL-effect on four independent parameters in equation 6.2 makes fitting the WAL-peaks in this chapter problematic. Further, since no additional method to determine τ_{iv} is available, assumptions for this property have to be made. WSe$_2$ has been reported to have a similar amount of surface roughness than hBN. Therefore, it is reasonable to assume that the employed graphene/WSe$_2$ heterostructures on SiO$_2$-substrates, investigated in sections 6.2 and 6.3, show a similar amount of intervalley scattering than in graphene/hBN on SiO$_2$. Thus, for fitting the measurements in sections 6.2 and 6.3, an intervalley scattering length of $\lambda_{iv} = 420\,\text{nm}$, which was obtained from WL-measurements in section 6.4 (see figure 6.13 (a)), is assumed. Importantly, as λ_{iv} is a measure of the average distance between atomically sharp defects in graphene, λ_{iv} is seen as a constant parameter rather than τ_{iv}, which can be obtained from $\lambda_{iv} = \sqrt{D\tau_{iv}}$.

The red and blue curves in figure 6.4 show fits of the conductivity with equation 6.2 and two sets of parameters. While the best fit to the data is clearly obtained by the red curve in figure 6.4, the blue curve still shows a reasonable fit with drastically different values for the spin orbit scattering times. Hence, also the anisotropy $\zeta = \frac{\tau_{asy}}{\tau_{sym}} + 1/2 \approx \frac{\tau_{asy}}{\tau_{sym}}$ from equation 4.28 has to be considered. Here, the value $\zeta = 38$ given by the fit shown as the red curve in figure 6.4 is in good agreement with values obtained from spin injection measurements in graphene/WSe$_2$ samples, which showed an anisotropy of $\zeta = 10-40$ [220, 221], considering that ζ is also expected to be dependent on the charge carrier density. Also, the magnitude of the spin orbit scattering time is in general agreement with WAL measurements in graphene/WSe$_2$ by various groups [153, 155, 158, 160]. Further, the extracted phase coherence time of $\tau_\phi = 8.0\,\text{ps}$ is comparable to the value of $\tau_\phi = 6.9\,\text{ps}$, obtained from the UCF-analysis in figure 6.3 (b).

Given the ambiguity of the fitting parameters shown in figure 6.4, the extracted scattering times from the WAL-fits have to be taken with care, especially considering the influence of residual contributions of UCFs in the magnetoconductivity curves, which can not be fully removed by the ensemble averaging process mentioned above. However, the order of magnitude of the extracted scattering times as well as the general behavior with changing temperature, charge carrier density and transverse electric field are still robust against potential sources of error in the fitting procedure.

6.2.4 Temperature Dependence of WAL-peaks

To verify that the peak in the conductivity shown in figure 6.4 is due to the WAL-effect, the dependence of this peak on temperature is depicted in figure 6.5 (a). As with the

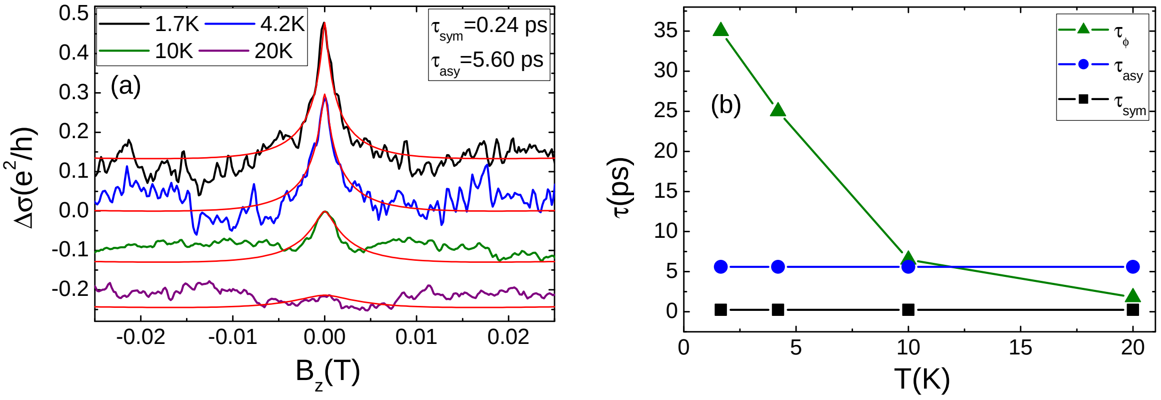

Figure 6.5: *(a) Magnetoconductivity at different temperatures after averaging over several curves at slightly different charge carrier density and subtraction of a parabolic background. Here, an arbitrary offset has been added for clarity. A decrease of the WAL-peak with increasing temperature can be observed. (b) Parameters obtained from fitting the curves in (a) (as shown by the red curves in (a)) in dependence of temperature. τ_ϕ decreases with increasing temperature, while the spin orbit scattering times remain constant.*

following graphs in this chapter depicting the correction to the magnetoconductivity $\Delta\sigma$, an arbitrary offset has been added to the curves for clarity. The rapid decay of the observed peak in the conductivity at $B_z = 0\,\mathrm{T}$ with increasing temperature is a clear indication for the phase coherent characteristic of this effect. Further, good fits to the data for all temperatures can be found when the spin orbit scattering times τ_{sym} and τ_{asy} are kept constant. This is reasonable, since τ_{sym} and τ_{asy} are only expected to be weakly dependent on temperature for various sources of spin relaxation. Therefore, the decay of the WAL-peak with increasing temperature can be attributed to the decreasing phase coherence time τ_ϕ, as can be seen in figure 6.5 (b).

These measurements, which were taken at a mean charge carrier density of $n = 1.0 \cdot 10^{12}/\mathrm{cm}^2$, were performed after a second cooldown with regard to the other measurements in this section. Warming up and cooling down the sample had a slight effect on the position of the CNP in gatesweeps and on the parameters extracted from the analysis of the WAL-behavior, especially on the phase coherence time τ_ϕ. Thus, the parameters shown in figure 6.5 can not be directly compared to the measurements in figure 6.6. A likely source for the change in sample parameters during the subsequent cooldown are mid-bandgap states due to impurities in the WSe$_2$ layer, which can be populated or depopulated at higher temperatures, but are trapped at low temperature.

6.2.5 Charge Carrier Density Dependence and Dominant Spin-Relaxation Mechanism

To give an estimate of the SOC-strength in this sample, the dominant source of spin relaxation, which limits the observed τ_{sym} and τ_{asy}, has to be determined. As discussed

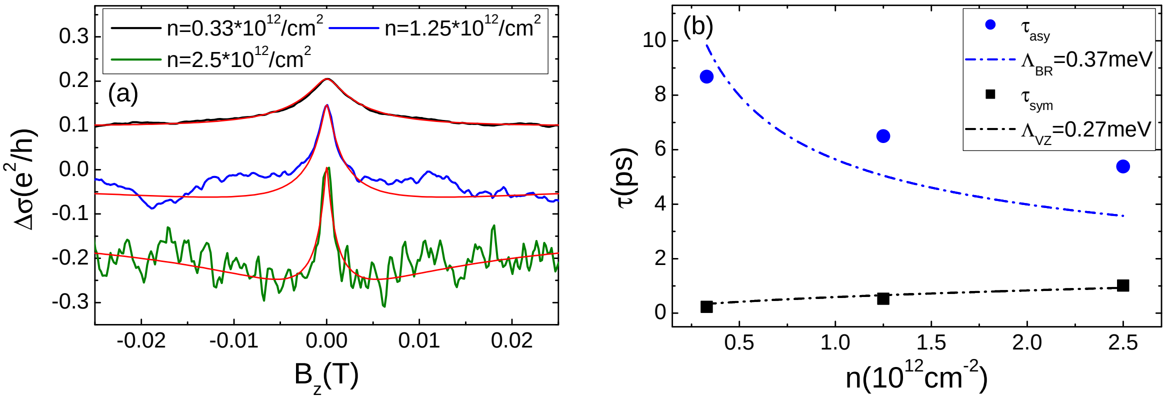

Figure 6.6: *(a) Magnetoconductivity at three different charge carrier densities. All curves can be fitted with equation 6.2 (red curves). (b) Charge carrier density dependence of extracted spin orbit scattering times.* τ_{sym} *and* τ_{asy} *show opposite trends with increasing n, which is in agreement with the predicted Dyakonov-Perel mechanism as the dominant source of spin orbit scattering. Fitting these data points (dashed curves) provides an estimate for the SOC-strengths in this sample.*

in section 4.2.3, different spin relaxation mechanisms can be distinguished by their relation to the momentum scattering time τ_p and therefore their dependence on charge carrier density n.

Thus, figure 6.6 (a) depicts the WAL-effect at three different charge carrier densities at a temperature of $T = 1.7\,\mathrm{K}$. Here, it can be seen that the WAL-peak increases in height and narrows in width as n is increased. The main reason for this behavior is the increase in the phase coherence time with increasing charge carrier density (not shown here), which is consistent with electron-electron interaction as the main source of phase decoherence, as discussed in section 4.1.

Further, figure 6.6 (b) depicts the charge carrier density dependence of the extracted spin orbit scattering times τ_{sym} and τ_{asy}. Importantly, τ_{sym} and τ_{asy} show opposite trends with regard to increasing n. The decrease of τ_{asy} with increasing charge carrier density is typical for the Dyakonov-Perel mechanism as the dominant source of spin orbit scattering in graphene. τ_{asy} is limited by symmetry breaking SOC-sources and is inversely proportional to the momentum scattering time $\tau_{asy} \propto \tau_p^{-1} \propto n^{-1/2}$, according to equation 4.26.

Assuming the term $ak\Delta_{PIA}$ to be small ($ak\Delta_{PIA} < 6\,\mu\mathrm{eV}$ in the investigated charge carrier density range, based on [61]), the blue curve in figure 6.6 (b) shows the best fit to the observed values of τ_{asy} with equation 4.26. From this, an estimate for the Rashba SOC-strength of $\Lambda_{BR} = 0.37\,\mathrm{meV}$ can be achieved. This value is in good agreement with $\Lambda_{BR} = 0.56\,\mathrm{meV}$, obtained from DFT calculations in graphene/WSe$_2$ by Gmitra et al. [61] (see section 2.3.4), considering the uncertainty for analyzing the WAL-curves.

Contrary to that, τ_{sym}, which takes into account only symmetric sources of SOC, increases with increasing n in figure 6.6 (b). The conventionally discussed Elliott-Yafet mechanism can not sufficiently explain the very small values of τ_{sym} depicted in figure 6.6 (b), since applying equation 4.21 results in an unrealistically large intrinsic SOC-strength of $\Lambda_I = 84\,\mathrm{meV}$. Such a large SOC-strength would certainly be observable as a bandgap (see section 2.3.2) in the transport measurements shown in figure 6.2.

However, the charge carrier density dependence of τ_{sym} is in good agreement with the occurrence of the so called valley Zeeman SOC in graphene/WSe$_2$, which is due to different SOC-terms for the two sublattices in graphene (see section 2.3.4). As discussed in section 4.2.4, valley Zeeman SOC induces an effective out-of plane magnetic field that is opposite for the two different valleys in graphene. Thus, the correlation time relevant for the Dyakonov-Perel mechanism is the intervalley scattering time τ_{iv}, rather than the momentum scattering time. As discussed in section 6.2.3, τ_{iv} in this sample is unknown, however a constant value for the intervalley scattering length λ_{iv} was assumed for fitting the WAL-curves in this section. Consequently, the relation $\tau_{iv} = \lambda_{iv}^2/D \propto 1/\sqrt{n}$ is expected for the intervalley scattering time, which leads to $\tau_{sym} \propto \sqrt{n}$.

Applying equation 4.27 to the extracted values of τ_{sym} in figure 6.6 shows good agreement with a value for the valley Zeeman SOC-strength of $\Lambda_{VZ} = 0.27\,\mathrm{meV}$. This value is by a factor of four smaller than $\Lambda_{VZ} = 1.2\,\mathrm{meV}$, obtained by Gmitra et al. [61]. Here, the assumed value of $\lambda_{iv} = 420\,\mathrm{nm}$ for the intervalley scattering length directly influences the extracted Λ_{VZ}. Thus, a shorter λ_{iv} in the actual sample would result in an increased Λ_{VZ}.

Further, it has to be noted that equation 4.27 was calculated in the regime of strong intervalley scattering with $\omega_z \tau_{iv} < 1$ and $\omega_z = 2\Lambda_{VZ}/\hbar$. This condition is a prerequisite for the Dyakonov-Perel mechanism, as described in section 4.2.3, since for $\omega_z \tau_{iv} > 1$ on average a full precession of the electron spin occurs before the effective magnetic field induced by the SOC changes direction [226]. However, depending on the actual intervalley scattering length, this might not always be the case in this sample, especially at low charge carrier densities. This can therefore lead to an underestimation of the extracted parameter Λ_{VZ} (see also the discussion in the supplementary of [160]).

Furthermore, the calculations in [61] were done for a system consisting of graphene on monolayer WSe$_2$, while for the samples in this chapter, bulk WSe$_2$ has been used. A possible difference for the induced SOC-strength between monolayer and bulk TMDs was reported by Wakamura et al. [157, 158]. The relative orientation between graphene and WSe$_2$ was also predicted to influence the induced SOC-strength [85, 86]. This can be understood, since Λ_{VZ} depends on the different environment of the two sublattices of graphene, which is induced by different lattice constant of graphene and WSe$_2$. Therefore, it is not surprising that Λ_{VZ} can be influenced by changing the relative orientation between these two materials. However, a comparison with theory can not be obtained here, since the exact twist angle in this sample is unknown.

6.2.6 Influence of Transverse Electric Field

The availability of both a top- and a backgate in this sample allows independent tuning of the charge carrier density and the transverse electric field. Thus, the dependence

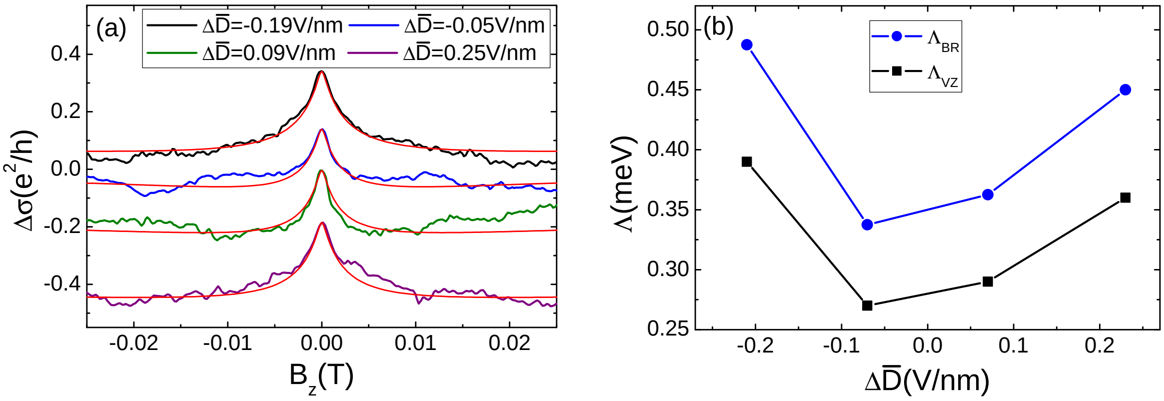

Figure 6.7: *(a) Magnetoconductivity at different applied out-of plane electric displacement fields $\Delta\bar{D}$ with fits from equation 6.2 (red curves). (b) Electric field dependence of the extracted SOC-strengths, obtained from the fits in (a). A small influence of the applied field on Λ_{BR} and Λ_{VZ} can be observed. Importantly, the absolute value for the applied displacement field in this sample is unknown, which leads to an arbitrary position of $\Delta\bar{D} = 0$ V/nm.*

of the WAL behavior on an applied electric field at a constant charge carrier density can be investigated.

Figure 6.7 (a) shows the occurrence of the WAL-effect for four different values of applied electric displacement field $\Delta\bar{D}$ at a charge carrier density of $n = 1.25{\cdot}10^{12}\,/\mathrm{cm}^2$ and temperature of $T = 1.7\,\mathrm{K}$. For fitting these curves (red curves in figure 6.7 (a)), a constant value for the phase coherence time τ_ϕ was assumed, since the dominant dephasing mechanism of electron-electron interaction is expected to be independent of a transverse electric field. Notably, the best fits for this curves were found, when the ratio $\zeta = \tau_{asy}/\tau_{sym}$ was kept at a constant value $\zeta = 12$ for all curves (this value is different than in section 6.2.3, since ζ is dependent on n).

Figure 6.7 (b) depicts the SOC-strengths Λ_{BR} and Λ_{VZ}, obtained by employing equations 4.26 and 4.27, according to the Dyakonov-Perel relaxation mechanism, to the spin orbit scattering times extracted from the fits in figure 6.7 (a). Here, the SOC-strengths increase with electric field in both directions. However, it has to be noted that the absolute value of the dielectric displacement field in single layer graphene can not be determined. This is since, contrary to bilayer graphene in section 6.3, a transverse electric field does not influence the bandstructure of single layer graphene. Hence, the parameters U_{b0} and U_{t0} in equation 3.6 can not be determined independently. Therefore, the position of $\Delta\bar{D} = 0\,\mathrm{V/nm}$ in figure 6.7 (b) is chosen arbitrarily.

The presence of an out-of plane electric field is in general predicted to induce Bychkov-Rashba SOC in graphene due to breaking of mirror symmetry (see section 2.3.1). This effect can be assumed to be on the same order of magnitude as in pristine graphene discussed in section 2.3.2. Then, for a change in displacement field of $\Delta\bar{D} = 0.2\,\mathrm{V/nm}$, a change of the Bychkov-Rashba SOC of $\Delta\Lambda_{BR} = 0.2 - 3\,\mu\mathrm{eV}$ is expected, depending on different theoretical calculations [62, 63]. Since this change is much smaller than the observed effect of the applied electric field, it can be disregarded in this analysis. Further, it has to be noted that accurate fits to the curves 6.7 (a) can not be achieved by only varying τ_{asy} (nor by only varying τ_{sym}) for different electric fields.

Another effect of the applied out-of plane field is an effective shift in energy of the valence and conduction bands of WSe$_2$ relative to the graphene bandstructure due to an added potential difference between the materials [300]. This can affect the mixing of electronic states of graphene and WSe$_2$, which in turn influences both Λ_{VZ} and Λ_{BR} [61, 81].

Electric field dependence on the WAL-effect in graphene covered with WS$_2$ was examined by Yang et al. [154]. Here, a monotonic increase in Λ_{BR} with applied field was observed. However, in their analysis, they argue that the induced valley Zeeman SOC does not have any effect on spin relaxation, leading to $\tau_{sym}^{-1} = 0$. This assumption is contrary to the findings in this section as well as spin relaxation experiments in graphene/TMD-heterostructures, which consistently found $\tau_{sym} < \tau_{asy}$ [220, 221]. Despite that, the monotonic behavior of Λ_{BR} with electric field can be consistent with the results in figure 6.7 (b), considering a possible difference in absolute electric field (the position of $\Delta\bar{D} = 0$) and a different position of the Fermi energy with respect to the graphene in WS$_2$, compared to WSe$_2$. These discrepancies can shift the investigated electric field range from the behavior in figure 6.7 (b), showing a minimum in the SOC-strengths, to the monotonic behavior observed in [154].

Zihlmann et al. reported measurements on the transverse electric field dependence of WAL-peaks in WSe$_2$/graphene/hBN stacks (supplementary of [160]). They observed a change in the extracted spin orbit scattering times at different electric fields, which amount to a similar change in the corresponding SOC-strengths as in figure 6.7 (b). However, they did not observe a clear trend in the extracted time scales with applied electric field. Further, they argue that the observed fluctuations in τ_{sym} and τ_{asy} are within the sensitivity of the measurement and thus no clear electric field tunability of the induced SOC can be observed.

Indeed, for the curves in figure 6.7 (a), contributions from universal conductance fluctuations, which persist after the ensemble averaging method discussed in section 6.2.3, are clearly visible. Hence, it can not be ruled out that the effect shown in figure 6.7 is influenced by these remaining UCFs. From this, a tunability of the SOC in this sample by applying a transverse electric field can not unambiguously be confirmed.

6.3 BL Graphene/WSe$_2$

As described in section 2.3.4, a much higher tunability of the induced SOC with a transverse electric field is expected in a system containing bilayer graphene and WSe$_2$ [41]. Thus, the sample depicted in figure 6.8 was fabricated. Here, a 24 nm thick hBN-flake was placed onto the etched and contacted Hall-bar to improve the stability of the topgate. Apart from the topgate characteristics, the additional hBN is not expected

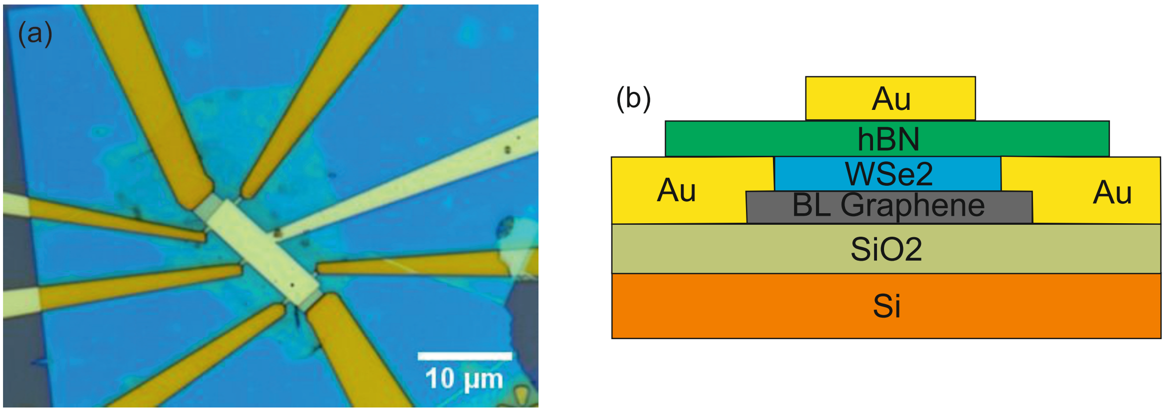

Figure 6.8: *(a) Optical microscope picture of a sample, consisting of a WSe$_2$/ bilayer graphene stack. (b) Schematic cross section of the sample.*

to influence the properties of the bilayer graphene. For a more detailed discussion of the results presented in this section, see [290].

6.3.1 Sample Characterization

Figure 6.9 (a) shows the backgate voltage dependence of the sample resistivity for different topgate voltages. As for the sample in section 6.2, the backgate voltage at which the CNP (maximum resistivity of the curves) occurs changes by varying the applied topgate voltage. Thus, the Fermi-energy in the graphene can be effectively shifted by both gates. Further, the maximum resistivity at the CNP also changes with applied topgate voltage. This is due to the different combinations of backgate and topgate voltages, which correspond to different external out-of plane electric fields. As discussed in section 2.2.2, this transverse electric field induces a bandgap in bilayer graphene, which can be observed as the increased resistivity at the CNP.

From the curve in figure 6.9 (a), which shows the lowest maximum resistivity at the CNP (black curve), a mobility on the hole-side of $\mu_h = 3000\,\mathrm{cm^2/Vs}$ can be extracted. In these measurements, the maximum values for the gate voltages, and therefore also for the applied electric field, are constricted. For the backgate, an applied voltage higher than $U_{bg} > 60\,\mathrm{V}$ likely results in a breakdown of the backgate dielectric, which results in the destruction of the sample. Applying topgate voltages above $U_{tg} > 6\,\mathrm{V}$ causes the Fermi-energy in the WSe$_2$ to shift into the conduction band. This leads to free electrons in the WSe$_2$, which effectively screen the additional topgate voltage [301]. Hence, the range of applied transverse electric field at specific charge carrier densities is limited by the gate dielectrics.

The position in backgate voltage of the CNP $U_{bg}(CNP)$ for different topgate voltages U_{tg} is depicted as the black squares in figure 6.9 (b). As can be seen by the black curve in figure 6.9 (b), $U_{bg}(CNP)$ shows a linear dependence on U_{tg}. From the slope of this curve, the ratio between backgate and topgate capacities C_b/C_t for equation 3.6 can be extracted, which allows to determine C_t from the known value C_b for the

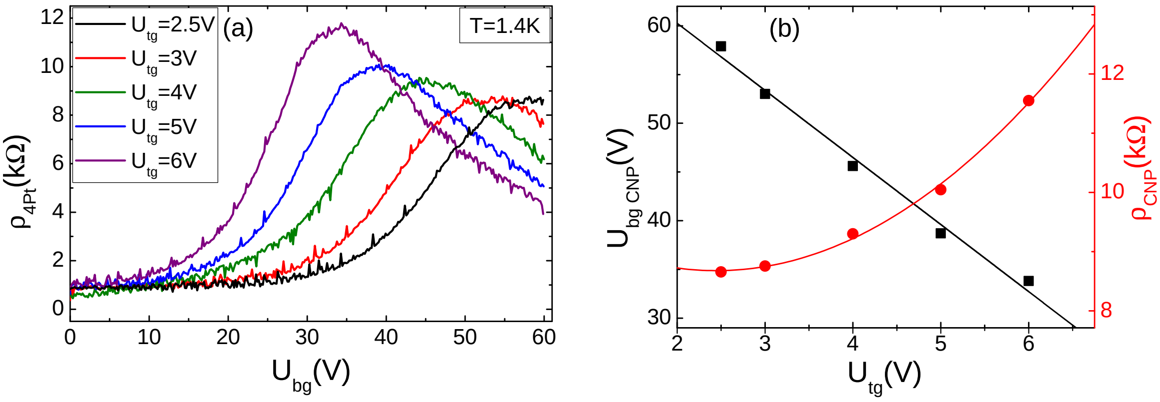

Figure 6.9: *(a) Backgate voltage dependence of the sample resistivity for different topgate voltage values U_{tg}. Applying a topgate voltage shifts the position of the backgate voltage, where the CNP occurs. Also, the maximum resistivity at the CNP changes with applied U_{tg}. (b) Dependence of the backgate voltage position of the CNP (black squares) with U_{tg}. From the linear dependence (black curve), the ratio between backgate and topgate capacities can be calculated. The sample resistivity at the CNP (red dots) follows a parabolic dependence with U_{tg} (red curve). Here, the increased resistivity is due to the out-of plane electric field determined by the combination of the gate voltages, which opens a bandgap in bilayer graphene.*

standard SiO$_2$-substrates, employed for all samples in this chapter.

Further, the red dots in figure 6.9 (b) show the maximum resistivity of the sample at the CNP for different topgate voltage values. These points follow a parabolic behavior with the applied topgate voltage (red curve in figure 6.9 (b)). Here, the minimum of the curve marks the combination of U_{bg} and U_{tg} with zero transverse electric field $\bar{D} = 0\,\mathrm{V/nm}$ and minimum charge carrier density. These gate voltage values correspond to U_{b0} and U_{t0} in equation 3.6. Thus, both charge carrier density and applied electric field can be tuned independently by the two gate voltages, according to equation 3.7. Then, contrary to the sample in section 6.2, for all gate voltages the absolute value of the transverse electric field $\bar{D}$ can be determined.

Importantly, here $\bar{D} = 0\,\mathrm{V/nm}$ corresponds to the situation where no bandgap occurs in the bilayer graphene. Therefore, this value is a combination of both the applied external and the internal transverse electric field, which can arise due to the proximity of graphene to the WSe$_2$. This is different than the bandstructures shown in figure 2.8, where the electric field values refer only to the external electric field. This means that the situation with $\bar{D} = 0\,\mathrm{V/nm}$ in this sample corresponds to the bandstructure calculation with $E_{ext} = -0.25\,\mathrm{V/nm}$ (figure 2.8 (c)) in figure 2.8.

6.3.2 Tunability of WAL with Applied Electric Field

Figure 6.10 shows the WAL-effect in the sample, depicted in figure 6.8, at a temperature of $T = 1.4\,\mathrm{K}$. By adjusting the back- and topgate voltage values according to

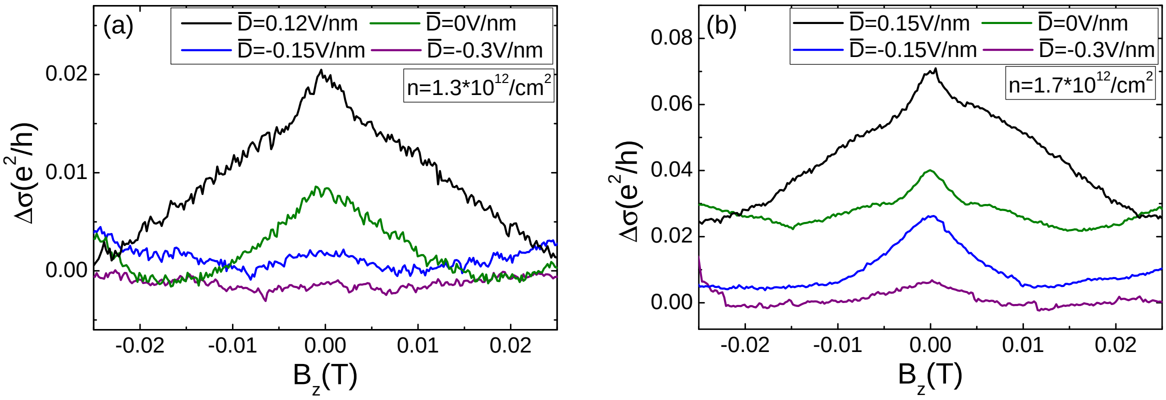

Figure 6.10: *Correction to the magnetoconductivity at constant charge carrier density* $n = 1.3 \cdot 10^{12}/cm^2$ *in (a) and* $n = 1.7 \cdot 10^{12}/cm^2$ *in (b) for different applied transvere electric fields* $\bar{D}$*. The WAL peak, which is clearly visible at* $\bar{D} = 0$ *V/nm for both values of* n*, increases by applying positive electric field and decreases with negative field.*

equations 3.6 and 3.7, for these curves the charge carrier density was kept at a constant value of $n = 1.3 \cdot 10^{12}\,/\mathrm{cm}^2$ in (a) and $n = 1.7 \cdot 10^{12}\,/\mathrm{cm}^2$ in (b), while the out-of plane electric field $\bar{D}$ was varied. As for the measurements of the WAL-effect in section 2.6, an average over several magnetic field sweeps at slightly different charge carrier densities (but constant $\bar{D}$) was taken and a parabolic background was subtracted for the curves in figure 6.10 (a) and (b).

Contrary to the results in the single layer graphene sample in figure 6.7 (a), the effect of the out-of plane electric field on the WAL behavior in this sample is clearly visible. As shown in figure 6.10, applying a positive electric field leads to an increased height of the WAL-peak, while applying negative field leads to a decrease of the peak. Also, the influence of the charge carrier density on the effect of the applied transverse electric field can be observed. This is apparent for the curves at the largest negative applied field of $\bar{D} = -0.3\,\mathrm{V/nm}$, where the peak almost vanishes for $n = 1.3 \cdot 10^{12}\,/\mathrm{cm}^2$ in figure 6.10 (a), while it is still clearly visible for $n = 1.7 \cdot 10^{12}\,/\mathrm{cm}^2$ in figure 6.10 (b).

Overall, the observed peaks are an order of magnitude smaller than for the sample in section 6.2, while the peak widths are strongly increased. This behavior points to a smaller phase coherence length in the bilayer graphene sample, compared to the sample containing single layer graphene. The smaller λ_ϕ is due to the lower mobility, which results in a smaller diffusion constant D as well as a shorter phase coherence time τ_ϕ at the same charge carrier density, reducing $\lambda_\phi = \sqrt{D\tau_\phi}$. The smaller peak heights in this sample hinder the unambiguous fitting of the WAL behavior with independent parameters τ_{sym} and τ_{asy} (see section 6.2.3).

6.3.3 Electric Field Tunability of the Induced SOC-Parameters

As discussed in section 2.3.4, a large tunability of the SOC in bilayer graphene/WSe$_2$ heterostructures with an applied out-of plane electric field is expected. In this system, the electronic states close to the CNP are comprised of states originating from the two different layers. Since the top layer in the sample discussed in this section is close to the WSe$_2$, large SOC is induced here. However, the short range character of this proximity effect results in a much smaller effect for the bottom layer, for which the induced SOC is expected to be similar as in pristine graphene [41].

Gmitra and Fabian predicted a two order of magnitude tunability of the SOC-strengths with application of a transverse electric field. A sharp transition between high and low SOC configurations appears only at low charge carrier density and large applied electric field, in particular when $2|\Delta_E| \gg |E_F|$ [54], where Δ_E denotes the potential energy difference between the two graphene layers invoked by the electric field. However, due to the relatively short phase coherence length in this sample, only WAL-peaks at higher charge carrier concentrations (shown in figure 6.10) could be investigated.

At these charge carrier densities, despite an applied out-of plane electric field, mixing of electronic states from the two different graphene layers occurs due to the off-diagonal terms in equation 2.11. This mixing can be taken into account by the occupation of the two layers $g_{1,2}$, described in equation 2.27. Here, g_2 denotes the polarization of the top layer of bilayer graphene (which is close to the WSe$_2$).

Following Khoo et al. and disregarding the small SOC in the bottom graphene layer (layer 1), the $z/-z$-symmetric SOC in dependence of electric field $\bar{D}$ is expected to follow the layer polarization as [54]:

$$\Lambda_{VZ}(\bar{D}) = \Lambda_{VZ,0} \cdot g_2(\bar{D}) \tag{6.3}$$

However, the WAL-behavior in figure 6.10 shows the opposite dependence on external electric field than the expected $\Lambda_{VZ}(\bar{D})$. Here, the WAL-peak height increases with positive electric field, while $g_2(\bar{D})$ and therefore $\Lambda_{VZ}(\bar{D})$ decreases. Also the experimental behavior seemingly contradicts the interpretation from Gmitra and Fabian [41], where an increase of the SOC-strength in the valence band is expected for negative electric field (since the layer sequence for the model in figure 2.8 is inverted compared to the experiment).

The likely reason for this discrepancy are opposite trends between symmetric and antisymmetric SOC-strengths with regard to applied electric field. As discussed in section 4.1.3, the presence of $z/-z$-mirror symmetry breaking SOC is essential for the occurrence of the WAL-effect in graphene. Thus, the decrease of the WAL-peaks in figure 6.10 can be caused by a decreasing $z/-z$-mirror symmetry breaking SOC, even in the case that the symmetric SOC is simultaneously increasing.

Due, to the small phase coherence time in this sample, it is not possible to independently examine τ_{sym} and τ_{asy}. Hence, additional experiments and theoretical efforts are necessary to analyze the electric field dependence of the various SOC-parameters in this system.

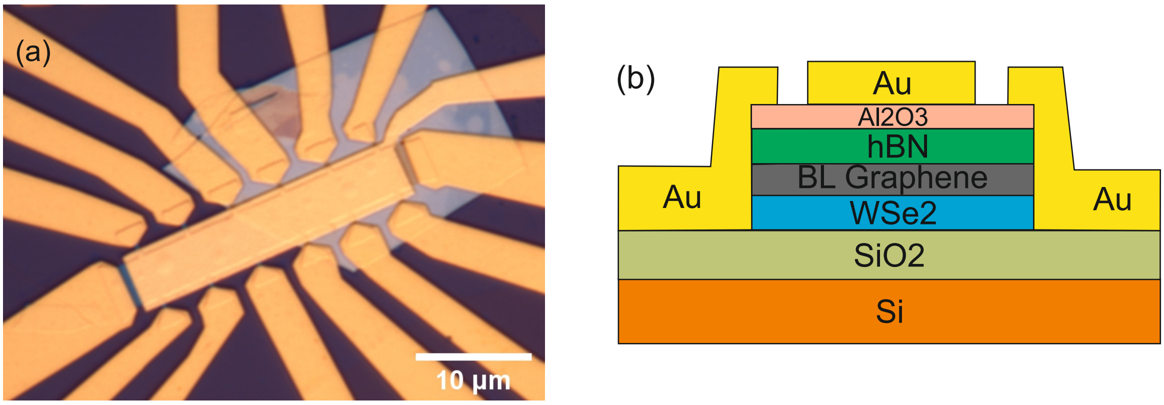

Figure 6.11: *(a) Optical microscope picture of a sample, consisting of a WSe_2/ bilayer graphene/hBN heterostructure. Here, the hBN/bilayer graphene stack is placed in a way that one part of the stack lies on the WSe_2 (blue flake) and the other part lies directly on the SiO_2 substrate. This allows to directly compare the effect of the two substrates in the same graphene sample. (b) Schematic cross section of the sample area lying on the WSe_2.*

6.4 hBN/BL Graphene/WSe_2

For the samples discussed in sections 6.2 and 6.3, the electron mobility was likely limited by the presence of the SiO_2 substrate. It is therefore intriguing to examine the possibility of high mobility graphene heterostructures with large induced SOC by the proximity to WSe_2.

Thus, samples where bilayer graphene was encapsulated between WSe_2 and hBN were fabricated. The sample structure employed here is shown schematically in figure 6.11 (b). As depicted in figure 6.11 (a), for the particular sample investigated in this section, bilayer graphene was picked up by hBN and the graphene/hBN was placed in such a way that part of the stack lies on the WSe_2 (seen as the blue flake in figure 6.11 (a)) and the other part lies directly on the SiO_2 substrate. Therefore, the sample consists of two different areas, which allows to directly compare the influence of the SiO_2 and WSe_2 substrates on the properties of graphene.

6.4.1 Sample Characterization

For the sample shown in figure 6.11 (a) only the topgate was fully functional. Therefore, control over the transverse electric field in this sample was not possible.

Figure 6.12 (a) shows the dependence of the sample resistivity on the topgate voltage for the two different sample areas. For the area with graphene/hBN on SiO_2, shown as the red curve in figure 6.12 (a), a small p-type doping can be observed. Further, from this curve mobilities of $\mu_{h,SiO_2} = 3200\,\mathrm{cm^2/Vs}$ for the hole- and $\mu_{el,SiO_2} = 5300\,\mathrm{cm^2/Vs}$ for the electron side can be extracted. This values are very similar to the mobility observed in bilayer graphene/WSe_2 on SiO_2, investigated in section 6.3. This confirms

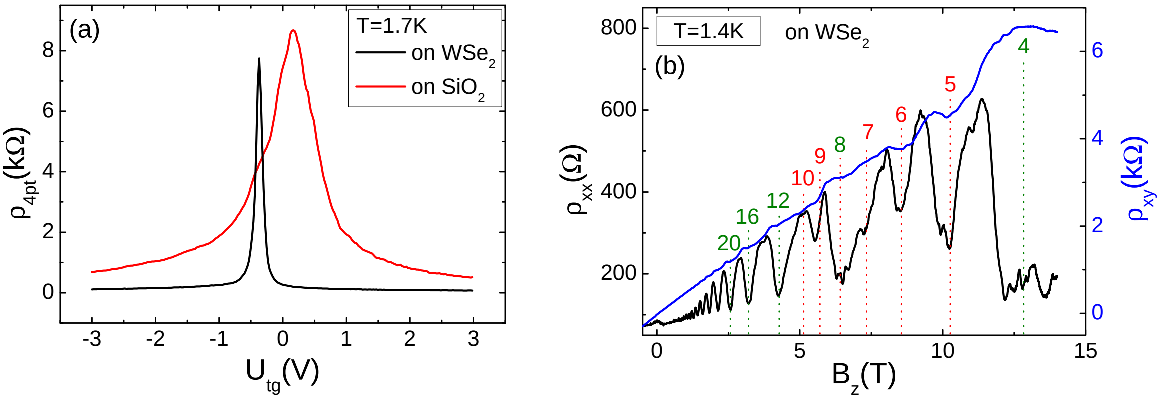

Figure 6.12: *(a) Dependence of sample resistivity on topgate voltage. The sample area where a bilayer graphene/hBN stack was placed onto WSe$_2$ (black curve) shows a much higher electron mobility than the sample area directly placed on the SiO$_2$ substrate (red curve). (b) High magnetic field dependence of the longitudinal (black curve) and transversal (blue curve) resistivity. Shubnikov-de Haas oscillations and plateaus in the Hall resistivity, stemming from the quantum-Hall effect, can be observed both at the fourfold degenerate (green numbers) and symmetry broken (red numbers) filling factors. The dotted vertical lines mark the calculated magnetic field position for the corresponding filling factors.*

that in the previously discussed samples, the electron mobility was limited by the SiO$_2$ substrate.

Contrary, the black curve in figure 6.12 (a) for the sample area on the WSe$_2$ shows a small n-type doping. Further, the black curve shows a much narrower peak, corresponding to lower resistivity away from the CNP, than the red curve. This behavior is in agreement with the larger extracted values for the mobility of $\mu_{h,WSe_2} = 57000\,\text{cm}^2/\text{Vs}$ and $\mu_{el,WSe_2} = 92000\,\text{cm}^2/\text{Vs}$ for hole and electron sides, for the area on WSe$_2$. Similar mobilities have also been found in hBN/single layer graphene/WS$_2$ heterostructures (see [302]).

For the sample area on WSe$_2$, the high mobility is confirmed by magnetoresistance measurements in a high magnetic field range. Figure 6.12 (b) shows the dependence of the longitudinal sample resistivity (black curve) and the transversal Hall-resistivity (red curve) on an out-of plane magnetic field. Here, pronounced Shubnikov-de Haas (SdH) oscillations and plateaus in the Hall resistivity can be observed for filling factors $v = 4 \cdot i$, where i is an integer number. Oscillations and quantum-Hall plateaus at these filling factors, which are marked by the green numbers and the green dotted lines in figure 6.12 (b), are typical for bilayer graphene [51] due to the fourfold degeneracy of the electronic states and the Berry phase of 2π [45].

However, as marked by the red numbers and dotted lines in figure 6.12 (b), at high magnetic field also oscillations and plateaus for filling factors $v \neq 4 \cdot i$ can be seen. These are a result of symmetry breaking by the applied magnetic field, which can lift the spin and valley degeneracies in graphene due to Zeeman and electron-electron

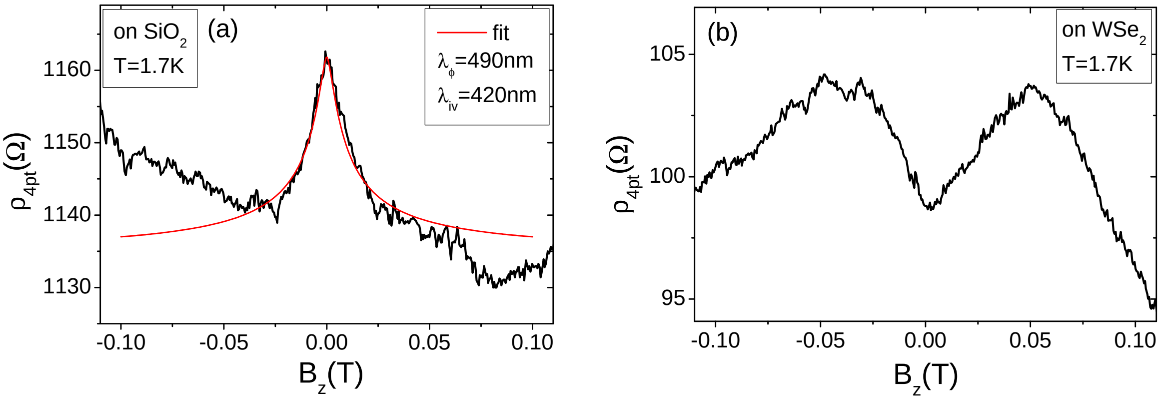

Figure 6.13: *(a) Magnetic field dependence of the resistivity of the sample area of bilayer graphene/hBN on SiO$_2$. The peak in the resistivity at $B_z = 0$ T can be attributed to the conventional WL effect. Fitting this peak with euqation 4.6 (red curve) gives values for the phase coherence and intervalley scattering times. (b) Magnetoresistivity for the sample area on WSe$_2$. Here, the dip in the conductivity is too large and too broad to be attributed to the WAL-effect.*

interactions [303–305]. Importantly, the splitting of the corresponding Landau-levels is only visible when the interaction energy is larger than the disorder broadening of the Landau levels [118]. Therefore, the observation of SdH oscillations and quantum-Hall plateaus at these symmetry broken filling factors is an indication of a high sample quality.

The lifting of the degeneracies hinders a possible analysis of a SOC signature in the spin splitting of the Landau levels, as proposed by Cysne et al. [306]. Further, Wang et al. reported a beating in the SdH oscillations in bilayer graphene/WSe$_2$, which they interpreted as stemming from induced SOC [153]. However, this interpretation is under debate, since it requires SOC-strengths that are one order of magnitude larger than the values predicted by theory and confirmed by WAL and spin injection measurements. For the samples in this section, no such beating can be observed at any charge carrier density. This is in agreement with recent reports by Chuang et al. for similar hBN/bilayer graphene/WSe$_2$ heterostructures [307].

6.4.2 Low Field Magnetoresistivity

The magnetic field dependence of the sample resistivity in a lower magnetic field range is depicted in figure 6.13 for the two different sample areas. Figure 6.13 (a) shows the magnetoresistivity for the area with bilayer graphene/hBN directly placed onto SiO$_2$ at a charge carrier density of $n = 1.0 \cdot 10^{12}/\text{cm}^2$. Importantly, in this section, the sample resistivity instead of the conductivity in sections 6.2 and 6.3 is shown. Thus, the peak observed at $B_z = 0$ T in figure 6.13 (a) corresponds to the conventional WL effect rather than WAL. This is not surprising, since in this sample area the graphene is not in contact with the WSe$_2$. Hence, the SOC-strength is expected to be similar than in pristine graphene.

Fitting the peak in the resistivity with equation 4.6 for the WL effect in bilayer graphene results in a phase coherence length of $\lambda_\phi = 490\,\mathrm{nm}$. Further, the intervalley scattering length $\lambda_{iv} = 420\,\mathrm{nm}$, extracted from this fit, was taken as a reference value for the analysis of the WAL-effect and the valley Zeeman SOC in sections 6.2 and 6.3.

Contrary to the sample area with bilayer graphene/hBN on SiO2, a pronounced dip in the resistivity around $B_z = 0\,\mathrm{T}$ can be observed in figure 6.13 (b) for the area on WSe$_2$. However, for this feature, the obvious interpretation of stemming from the WAL-effect due to the induced SOC by the WSe$_2$ can not be applied, since the dip in figure 6.13 (b) is much too large, with a magnitude of $\Delta\sigma = 20e^2/h$, and also too broad with regard to applied magnetic field to be fitted with equation 4.7 or 6.2, corresponding to the WAL-effect.

6.4.3 Magneto size effect

Dependence on Sample Width

To investigate the origin of the magnetic field dependent feature in figure 6.13 (b), figure 6.14 (a) shows the magnetoresistivity of two different samples consisting of hBN/bilayer graphene/WSe$_2$. Here, the black curve in figure 6.14 (a) is a zoom-out of figure 6.13 (b), while the red curve represents a sample with electron mobilities of $\mu_h = 90000\,\mathrm{cm^2/Vs}$ on the hole side and $\mu_{el} = 100000\,\mathrm{cm^2/Vs}$ on the electron side. Due to the similar mobilities in these two samples, the contrast in the magnetoresistivity feature can be assigned to the difference in sample size. Specifically, the observed feature is much broader and more pronounced in a sample with a width of $W = 1\,\mathrm{\mu m}$, shown by the red curve in figure 6.14 (a), than in the sample with width $W = 4\,\mathrm{\mu m}$, represented by the black curve.

The dependence of the magnetoresistivity on the sample width is a clear indication that this feature is stemming from a quasiballistic effect. Here, due to the high mobility in these samples, the mean free path of $\lambda_p \approx 1\,\mathrm{\mu m}$, depending on the charge carrier density (see section 3.1), is comparable to the width of the two samples.

A likely explanation for the observed behavior in figure 6.14 (a) of an increase in resistivity with magnetic field up to a certain point, followed by a decrease at higher fields, is the so called magneto size effect [91]. A prerequisite condition for this effect to occur is that scattering at the sample edges is predominantly diffusive, which is common for the disordered graphene edges created by reactive ion etching, as for the samples investigated in this section. This is in contrast to specular scattering, which occurs in electrostatically confined edges, where the longitudinal momentum is conserved during scattering at the edges [91].

The magneto size effect is illustrated in figure 6.14 (b). Here, diffusive scattering between the sample boundaries is initially increased by applying a perpendicular magnetic field, which increases the overall resistivity. At high magnetic field, the cyclotron diameter $2r_c$ becomes smaller than the sample width. Then, scattering at the edges can no longer reverse the direction of the scattered electrons and the sample resistivity

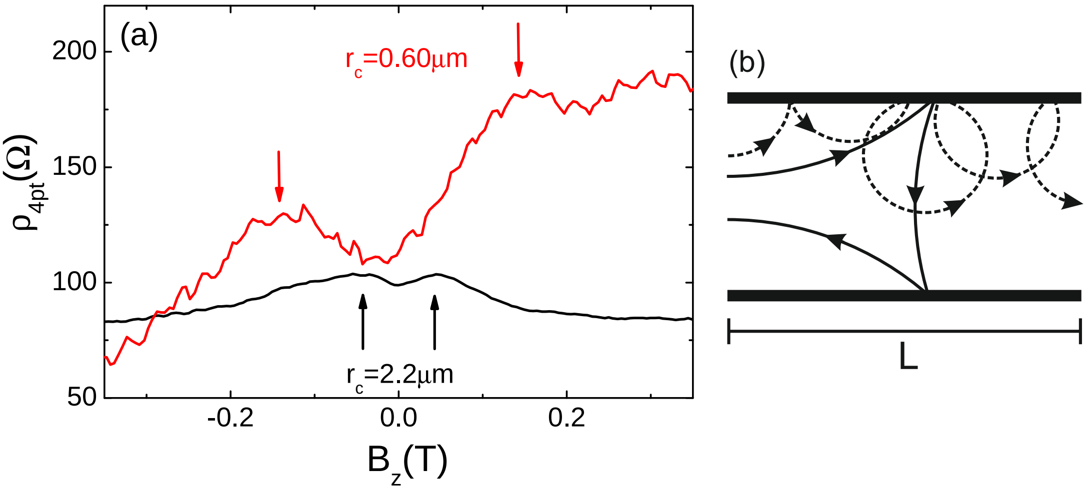

Figure 6.14: *(a) Magnetoresistivity from two samples with widths $W = 4\,\mu m$ (black curve) and $W = 1\,\mu m$ (red curve). The magnetic field dependent feature is much broader and more pronounced for the narrower sample. This is in agreement with the magneto size effect. The cyclotron radii for the magnetic field at maximum resistivity, calculated by equation 6.4, are shown by the black and red arrows. (b) Schematic electron trajectories in a finite sample with applied magnetic field. At low magnetic field with $2r_c \gg W$ (solid lines), the scattering between sample boundaries is initially increased with magnetic field strength. At higher magnetic field with $2r_c < W$ (dashed lines), backscattering at the sample edges and therefore the sample resistivity is decreased with magnetic field. Adapted from [308].*

becomes even smaller than the value at $B_z = 0\,\mathrm{T}$, which can be seen in figure 6.14 (a).

Characteristic for the magneto size effect is a fixed ratio between sample width W and the cyclotron radius r_c, at the magnetic field strength, at which the resistivity of the boundary scattering feature is at maximum. This cyclotron radius is given by [91]:

$$r_c(B_{max}) = \frac{\hbar k_F}{eB_{max}} = \frac{\hbar\sqrt{\pi n}}{eB_{max}} \tag{6.4}$$

In figure 6.14 (a), cyclotron radii of $r_c(B_{max}) = 2.2\,\mu\mathrm{m}$ for the 4 µm wide sample (marked by the black arrows) and $r_c(B_{max}) = 0.6\,\mu\mathrm{m}$ for the 1 µm wide sample (marked by the red arrows) are found. Thus, the cyclotron radius is proportional to the sample width with $W \approx 1.8 \cdot r_c(B_{max})$. Further, the higher amplitude of the effect in the 1 µm wide sample compared to the wider sample is in agreement with this effect, since for the narrower sample, the mean free path is closer to the sample width and scattering between sample boundaries is therefore increased.

In semiconductor two dimensional electron gases, a relation $W = 0.55 \cdot r_c(B_{max})$ was found [309] in agreement with theoretical calculations in the classical regime [310]. In single layer graphene/hBN heterostructures, the relation $W \approx 0.9 \cdot r_c(B_{max})$ was reported [95, 308]. This relation could be theoretically reproduced by a model specific to single layer graphene [311].

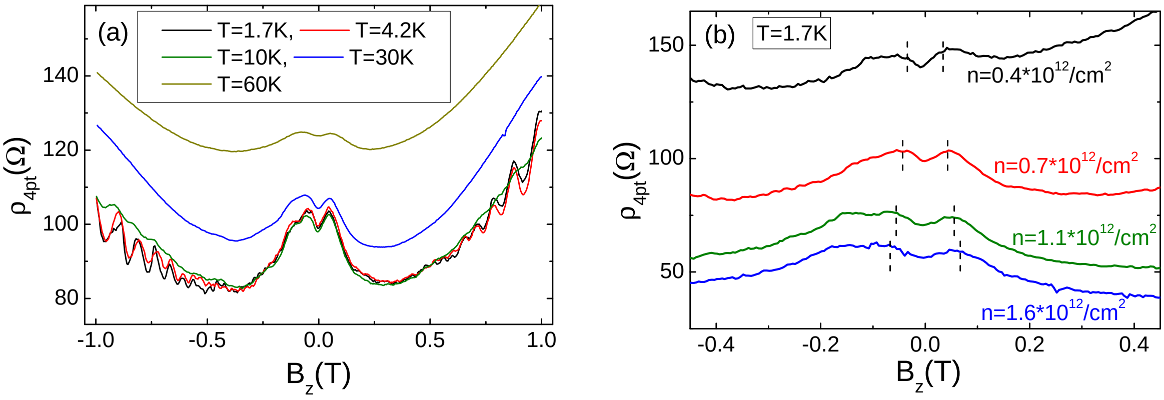

Figure 6.15: *(a) Magnetoresistivity at different temperatures. The low magnetic field feature is relatively stable with increasing temperature, which indicates a non phase coherent origin. (b) Charge carrier density dependence of the magnetoresistivity feature. The feature width increases with increasing n, which is consistent with the magneto size effect. The resistance peak positions follow the calculated magnetic field values (marked by the dashed vertical lines).*

Dependence on Temperature and Charge Carrier Density

The dependence of the magnetoresistivity feature on varying sample temperature and charge carrier density can further confirm the magneto size effect as the origin of the observed feature. Figure 6.15 (a) shows the magnetoresistivity at different temperatures. Here, no significant change in the low magnetic field behavior can be seen for $T \leq 10\,\mathrm{K}$ and traces of the low magnetic field feature are still observable at $T = 60\,\mathrm{K}$. This is in strong contrast to the WAL-effect observed in figure 6.5, where almost a complete decay of the WAL peaks occurred at $T = 20\,\mathrm{K}$. The high stability with temperature therefore excludes a phase coherent effect as the origin of the low magnetic field behavior. The decrease of the feature size at $T > 10\,\mathrm{K}$ in figure 6.15 (a) is likely due to a decrease in mean free path, which is also consistent with the overall increased sample resistivity.

Additionally, the charge carrier density dependence of the magnetoresistivity is depicted in figure 6.15 (b). Here, the feature width increases with increasing charge carrier density as the cyclotron radius increases, according to equation 6.4. This can be seen by the dotted vertical lines in figure 6.15 (b), which mark the magnetic field values at which the maximum resistivity from the boundary scattering effect is calculated with the relation $W = 1.8 \cdot r_c(B_{max})$. A good agreement between the resistance maxima in figure 6.15 (b) and the calculated magnetic field values can be found.

6.4.4 Absence of WAL in hBN/Bilayer Graphene/WSe$_2$

Notably, no WAL behavior could be observed in the hBN/Bilayer Graphene/WSe$_2$ samples. The absence of a WAL peak in these samples can be attributed to a number of possible reasons. First, since the bilayer graphene is only in contact with WSe$_2$ on one side, the induced SOC is dependent on the transverse electric field in the samples, as seen in section 6.3. However, for both samples discussed in this section, only one gate was functional. Therefore, no control or evaluation of the perpendicular electric field was possible. Thus, it can not be excluded that the induced SOC and consequently the expected WAL-effect in these samples is diminished by an unfavorable electric field configuration.

Additionally, Yang et al. showed that the presence of hBN in hBN/single layer graphene/WSe$_2$ reduces the interaction between graphene and WSe$_2$ and therefore possibly also the induced SOC-strength [312]. For this, they used the strong photoluminescence (PL) response of monolayer WSe$_2$ [313]. It has been shown that in monolayer WSe$_2$/graphene stacks the electron-hole pairs created in the WSe$_2$ during the PL measurement can recombine nonradiatively trough charge transfer to the graphene [314]. Thus, the PL in WSe$_2$/graphene is greatly suppressed. Contrary, for graphene encapsulated by WSe$_2$ and hBN, Yang et al. observed that the PL was restored to almost the magnitude in monolayer WSe$_2$. They attributed this to a slightly increased interlayer distance between graphene and WSe$_2$ due to the presence of the hBN. Since the proximity SOC is a very short ranged effect, this can drastically diminish the induced SOC in graphene. However, this is in disagreement with recent reports where signatures of strong induced SOC were found in hBN/graphene/TMD structures [87, 160].

Further, as indicated by the occurrence of the magneto size effect, electron transport in these samples is in the quasiballistic regime. However, WAL is a diffusive effect and equations 4.7 and 6.2 are only valid for $\tau_\phi > \tau_{sym,asy} > \tau_p$. For the mobilities observed in hBN/Bilayer Graphene/WSe$_2$, values of $\tau_p \approx 1\,\text{ps}$ can be found. Hence, $\tau_{sym} > \tau_p$ may not be valid here. Then, a possible WAL-effect is expected to be suppressed due to the reduced amount of backscattering. Such a behavior has also been observed in GaAs heterostructures [315]. In accordance with that, Zihlmann et al. observed WAL in high mobility hBN/single layer graphene/WSe$_2$ samples, while focusing only on the low charge carrier density range, where the mean free path is reduced [160].

6.5 Conclusion

In this chapter the properties of different heterostructures containing graphene and WSe$_2$ were investigated. For the sample in section 6.2, a single layer graphene/WSe$_2$ stack was placed onto a Si/SiO$_2$ substrate. The electron mobility in this sample was limited by the SiO$_2$ substrate, which keeps charge transport properties in the diffusive regime. Thus, measurements of a pronounced WAL-effect could be used to investigate the induced SOC in graphene. Here, the strong temperature dependence of the observed WAL behavior confirms the phase coherent characteristic of this effect.

The charge carrier density dependence of the spin orbit scattering times, extracted from the WAL peaks, showed good agreement with the expected relation from the Dyakonov-Perel mechanism in graphene/TMDs, as proposed by Cummings et al. [83]. Specifically, the opposite trends of symmetric and asymmetric spin orbit scattering times with increasing charge carrier density reflect the different characteristics of the corresponding SOC types. From this dependence, an estimate of the SOC-strengths could be made, which is in good agreement with theoretical reports. Further, a weak dependence of the WAL-peaks on an applied transverse electric field could be observed. However, it could not be excluded that this is only a remnant of spurious effects in the measurements.

Bilayer graphene/WSe_2 on SiO_2 investigated in section 6.3 showed a higher tunability of the WAL-peaks with applied electric field. Indeed, almost a complete vanishing of the observed WAL-peaks was seen by application of a negative (as defined in section 3.1) electric field, while an increase in WAL magnitude was observed for positive electric field. However, this behavior is in contrast to theoretical predictions, where for the investigated case with E_F lying in the valence band, a decrease of the SOC strength is expected for positive electric field [41].

This behavior can be caused by opposite trends of the symmetric and asymmetric SOC strengths with increasing electric field and the differing dependencies of the WAL-behavior on these scattering times according to section 4.1.3. Examining the exact behavior of the various SOC-terms in this system with an applied transverse electric field is a work in progress and requires additional measurements from different samples, as well as theoretical calculations. However, the strong influence of this electric field on the observed WAL-behavior is already clearly observable here.

Encapsulation of bilayer graphene between WSe_2 and hBN investigated in section 6.4 showed high electron mobilities that are comparable to values obtained in graphene encapsulated between hBN on both sides. The suitability of WSe_2 for high quality graphene was made apparent by comparing measurements of two areas of the same sample, where either SiO_2 or WSe_2 was used as the substrate for a bilayer graphene/hBN stack.

Further, a magnetoresistivity feature in WSe_2/bilayer graphene/hBN could be attributed to a quasiballistic boundary scattering effect. This interpretation is in agreement with the observed dependence of this resistivity feature on sample temperature, charge carrier density and sample width. The transition to the quasiballistic charge transport regime in these samples is also the likely reason for the lack of any WAL feature. Thus, no statement on the induced SOC in these samples could be made.

7 Summary

In this thesis, the possibility to increase the otherwise very weak SOC in graphene by functionalization was explored. To this end, effects stemming from SOC in graphene functionalized with two different methods were examined. Since these results aim to advance the progress towards potential spintronic devices, the electron mobility of the different structures was also taken into account.

In chapter 5, functionalization of single layer graphene was done by weakly hydrogenating graphene. Here, the amount of applied hydrogen could be regulated by the employed method of plasma hydrogenation. This method was characterized by Raman measurements, which show a peak in the Raman spectra upon hydrogenation corresponding to atomically sharp defects. Contrary to previously employed methods in the literature, comparing the different desorption behavior of hydrogen and deuterium atoms unambiguously confirms that these defects consist of bonded hydrogen atoms.

In devices fabricated by this method, charge and spin transport measurements were performed. Measurements of both weak localization and nonlocal spin transport did not indicate a drastically increased SOC, compared to the case of pristine graphene. With these methods a lower bound for the spin orbit scattering time of $\tau_{SO} > 100\,\mathrm{ps}$ in the employed hydrogenated graphene samples could be established.

Different measurements were performed to solve the controversy regarding the reported giant SHE in weakly hydrogenated graphene. Employing the H-bar configuration confirmed the reported large nonlocal resistance, which was previously interpreted as stemming from a combination of the SHE and the inverse SHE. However, no dependence of this nonlocal signal on an applied inplane magnetic field could be found, which indicates a non spin related origin.

Further, by using a more direct way to measure the SHE with spin injection through a ferromagnetic contact, no signature of a giant SHE was found, which is in accordance with theoretical calculations. Thus, it can be concluded that the large nonlocal resistance obtained in the H-bar method is not an indication of a giant SHE in hydrogenated graphene. However, the exact origin of this nonlocal signal is still unknown and requires further investigation.

Hence, the potential of hydrogenated graphene as a high mobility material with large SOC seems to be limited, since no clear sign of a drastically increased SOC in this system could be found. Further, already in this rather dilute limit of hydrogen concentration, the electron mobility of the devices was limited by the applied hydrogen atoms.

This is contrary to the results in chapter 6, where SOC is induced by bringing graphene into proximity to the TMD WSe_2. Magnetotransport measurements in single layer graphene/WSe_2 structures showed a pronounced WAL-effect, indicating large

SOC in the graphene sample. The dependence of this WAL-feature on charge carrier density showed good agreement with theoretical predictions for the different types and magnitudes of the induced SOC.

Additionally, in bilayer graphene/WSe_2 a high tunability of the WAL-feature with application of an electric field transverse to the graphene plane was observed. These results show the potential of this sample structure for a spin transistor design as suggested in [41, 42], or other spintronic applications which require tunable SOC strength. However, apparent contradiction with theoretical expectations of the electric field dependence of the induced SOC requires further investigations of this material system.

Further, sample structures with bilayer graphene completely encapsulated with WSe_2 on one side and hBN on the other side confirmed the suitability of WSe_2 as a substrate for high quality graphene devices. The high electron mobility in these samples, extracted from charge transport, was confirmed by the occurrence of a quasiballistic boundary scattering effect in a sample as wide as 4 µm. The high mobility in this sample also prevented an estimate of the SOC-strength by measurement of the WAL-effect in this sample structure type.

The combination of the measurements in the different sample structures in chapter 6 confirms the suitability of WSe_2 as a substrate for high mobility graphene with large, possibly electric field tunable, induced SOC-strength. Also, the employed assembly technique provides the opportunity to combine different proximity induced effects from different materials on both sides of graphene, such as increased SOC and induced magnetism [316]. Thus, the properties of graphene can further be tuned to reveal new interesting phenomena or to fit potential applications.

Bibliography

[1] K. S. Novoselov et al. “Electric Field Effect in Atomically Thin Carbon Films”. In: *Science* 306 (2004), pp. 666–669 (cit. on pp. 1, 20, 72).

[2] A. K. Geim and K. S. Novoselov. “The rise of graphene”. In: *Nat Mater* 6 (2007), pp. 183–191 (cit. on pp. 1, 21).

[3] Jian-Hao Chen et al. “Intrinsic and extrinsic performance limits of graphene devices on SiO2”. In: *Nat Nano* 3 (2008), pp. 206–209 (cit. on p. 1).

[4] K. I. Bolotin et al. “Temperature-Dependent Transport in Suspended Graphene”. In: *Phys. Rev. Lett.* 101 (2008), p. 096802 (cit. on p. 1).

[5] C. R. Dean et al. “Boron nitride substrates for high-quality graphene electronics”. In: *Nat Nano* 5 (2010), pp. 722–726 (cit. on pp. 1, 14).

[6] E. Prada et al. “Singular elastic strains and magnetoconductance of suspended graphene”. In: *Phys. Rev. B* 81 (2010), p. 161402 (cit. on p. 1).

[7] L. A. Ponomarenko et al. “Cloning of Dirac fermions in graphene superlattices”. In: *Nature* 497 (2013), pp. 594–597 (cit. on pp. 1, 2).

[8] Denis Kochan, Martin Gmitra, and Jaroslav Fabian. “Spin Relaxation Mechanism in Graphene: Resonant Scattering by Magnetic Impurities”. In: *Phys. Rev. Lett.* 112 (2014), p. 116602 (cit. on pp. 1, 41, 43).

[9] John Orton. *Semiconductors and the Information Revolution.* Academic Press, 2009, pp. 31–56 (cit. on p. 1).

[10] Wolfgang Pauli. “Letter to Peierls”. In: *Wissenschaftlicher Briefwechsel mit Bohr, Einstein, Heisenberg u.a. Band II.* Springer, 1931 (cit. on p. 1).

[11] D. C. Elias et al. “Control of Graphene’s Properties by Reversible Hydrogenation: Evidence for Graphane”. In: *Science* 323 (2009), pp. 610–613 (cit. on pp. 1, 13, 53).

[12] Rahul R. Nair et al. “Fluorographene: A Two-Dimensional Counterpart of Teflon”. In: *Small* 6 (2010), pp. 2877–2884 (cit. on p. 1).

[13] X. Hong et al. “Colossal negative magnetoresistance in dilute fluorinated graphene”. In: *Phys. Rev. B* 83 (2011), p. 085410 (cit. on p. 1).

[14] X. Hong et al. “Evidence for Spin-Flip Scattering and Local Moments in Dilute Fluorinated Graphene”. In: *Phys. Rev. Lett.* 108 (2012), p. 226602 (cit. on p. 1).

[15] Susanne Irmer et al. “Spin-orbit coupling in fluorinated graphene”. In: *Phys. Rev. B* 91 (2015), p. 115141 (cit. on p. 1).

[16] Tobias Frank et al. "Copper adatoms on graphene: Theory of orbital and spin-orbital effects". In: *Phys. Rev. B* 95 (2017), p. 035402 (cit. on p. 1).

[17] Zhenzhao Jia et al. "Transport study of graphene adsorbed with indium adatoms". In: *Phys. Rev. B* 91 (2015), p. 085411 (cit. on p. 1).

[18] Yilin Wang et al. "Neutral-current Hall effects in disordered graphene". In: *Phys. Rev. B* 92 (2015), p. 161411 (cit. on pp. 1, 2, 50, 75).

[19] R. R. Nair et al. "Spin-half paramagnetism in graphene induced by point defects". In: *Nature Physics* 8 (2012), pp. 199–202 (cit. on pp. 1, 41).

[20] E. C. T. O'Farrell et al. "Rashba Interaction and Local Magnetic Moments in a Graphene-BN Heterostructure Intercalated with Au". In: *Phys. Rev. Lett.* 117 (2016), p. 076603 (cit. on p. 1).

[21] J. Kotakoski et al. "From Point Defects in Graphene to Two-Dimensional Amorphous Carbon". In: *Phys. Rev. Lett.* 106 (2011), p. 105505 (cit. on pp. 1, 54).

[22] Igor Zutic et al. "Proximitized materials". In: *Materials Today* 22 (2019), pp. 85–107 (cit. on p. 2).

[23] C. Tonnoir et al. "Induced Superconductivity in Graphene Grown on Rhenium". In: *Phys. Rev. Lett.* 111 (24 2013), p. 246805 (cit. on p. 2).

[24] D. K. Efetov et al. "Specular interband Andreev reflections at van der Waals interfaces between graphene and NbSe2". In: *Nature Physics* 12 (2016), pp. 328–332 (cit. on p. 2).

[25] Landry Bretheau et al. "Tunnelling spectroscopy of Andreev states in graphene". In: *Nature Physics* 13 (2017), pp. 756–760 (cit. on p. 2).

[26] Zhiyong Wang et al. "Proximity-Induced Ferromagnetism in Graphene Revealed by the Anomalous Hall Effect". In: *Phys. Rev. Lett.* 114 (1 2015), p. 016603 (cit. on p. 2).

[27] Johannes Christian Leutenantsmeyer et al. "Proximity induced room temperature ferromagnetism in graphene probed with spin currents". In: *2D Materials* 4 (2017), p. 014001 (cit. on p. 2).

[28] Bogdan Karpiak et al. "Magnetic proximity in a van der Waals heterostructure of magnetic insulator and graphene". In: *2D Materials* 7 (2019), p. 015026 (cit. on p. 2).

[29] C. R. Dean et al. "Hofstadter/'s butterfly and the fractal quantum Hall effect in moire superlattices". In: *Nature* 497 (2013), pp. 598–602 (cit. on p. 2).

[30] B. Hunt et al. "Massive Dirac Fermions and Hofstadter Butterfly in a van der Waals Heterostructure". In: *Science* 340 (2013), pp. 1427–1430 (cit. on pp. 2, 75).

[31] Igor Zutic, Jaroslav Fabian, and S. Das Sarma. "Spintronics: Fundamentals and applications". In: *Rev. Mod. Phys.* 76 (2004), pp. 323–410 (cit. on pp. 2, 34).

[32] Jaroslav Fabian et al. “Semiconductor Spintronics”. In: *Acta Phys. Slov.* 57 (2007), p. 565 (cit. on pp. 2, 9, 34–37, 39, 41).

[33] Wei Han et al. “Graphene spintronics”. In: *Nat Nano* 9 (2014), pp. 794–807 (cit. on pp. 2, 40).

[34] Z M Gebeyehu et al. “Spin communication over 30 μm long channels of chemical vapor deposited graphene on SiO2”. In: *2D Materials* 6 (2019), p. 034003 (cit. on pp. 2, 43).

[35] A. H. Castro Neto and F. Guinea. “Impurity-Induced Spin-Orbit Coupling in Graphene”. In: *Phys. Rev. Lett.* 103 (2009), p. 026804 (cit. on pp. 2, 13, 53).

[36] Martin Gmitra, Denis Kochan, and Jaroslav Fabian. “Spin-Orbit Coupling in Hydrogenated Graphene”. In: *Phys. Rev. Lett.* 110 (2013), p. 246602 (cit. on pp. 2, 10, 13).

[37] Jayakumar Balakrishnan. “Spin transport studies in graphene”. PhD thesis. Department of physics national university of singapore, 2013 (cit. on pp. 2, 47, 49).

[38] A. A. Kaverzin and B. J. van Wees. “Electron transport nonlocality in monolayer graphene modified with hydrogen silsesquioxane polymerization”. In: *Phys. Rev. B* 91 (2015), p. 165412 (cit. on pp. 2, 49, 50, 53, 54, 57, 61, 62, 75, 79).

[39] D. Van Tuan et al. “Spin Hall Effect and Origins of Nonlocal Resistance in Adatom-Decorated Graphene”. In: *Phys. Rev. Lett.* 117 (2016), p. 176602 (cit. on pp. 2, 78).

[40] Martin Gmitra and Jaroslav Fabian. “Graphene on transition-metal dichalcogenides: A platform for proximity spin-orbit physics and optospintronics”. In: *Phys. Rev. B* 92 (2015), p. 155403 (cit. on pp. 2, 11, 14, 15).

[41] Martin Gmitra and Jaroslav Fabian. “Proximity Effects in Bilayer Graphene on Monolayer WSe_2: Field-Effect Spin Valley Locking, Spin-Orbit Valve, and Spin Transistor”. In: *Phys. Rev. Lett.* 119 (2017), p. 146401 (cit. on pp. 2, 3, 8, 16, 17, 92, 96, 104, 106).

[42] Kimberley C. Hall and Michael E. Flatté. “Performance of a spin-based insulated gate field effect transistor”. In: *Applied Physics Letters* 88 (2006), p. 162503 (cit. on pp. 3, 106).

[43] A. H. Castro Neto et al. “The electronic properties of graphene”. In: *Rev. Mod. Phys.* 81 (2009), pp. 109–162 (cit. on pp. 6, 7, 32).

[44] N. M. R. Peres. “The transport properties of graphene”. In: *Journal of Physics: Condensed Matter* 21 (2009), p. 323201 (cit. on pp. 5, 7).

[45] M.I. Katsnelson. *Graphene: Carbon in Two Dimensions.* Cambridge University Press, 2012 (cit. on pp. 5–8, 31, 42, 98).

[46] P. R. Wallace. “The Band Theory of Graphite”. In: *Phys. Rev.* 71 (1947), pp. 622–634 (cit. on pp. 5, 6).

[47] G.F. Bassani and G.P. Parravicini. *Electronic states and optical transitions in solids.* International series of monographs in the science of the solid state. Pergamon Press, 1975 (cit. on p. 5).

[48] D. W. Boukhvalov, M. I. Katsnelson, and A. I. Lichtenstein. “Hydrogen on graphene: Electronic structure, total energy, structural distortions and magnetism from first-principles calculations”. In: *Phys. Rev. B* 77 (2008), p. 035427 (cit. on pp. 7, 13).

[49] Yuanbo Zhang et al. “Direct observation of a widely tunable bandgap in bilayer graphene”. In: *Nature* 459 (2009), pp. 820–823 (cit. on pp. 8, 21).

[50] Edward McCann, David S.L. Abergel, and Vladimir I. Fal’ko. “Electrons in bilayer graphene”. In: *Solid State Communications* 143 (2007). Exploring graphene, pp. 110–115 (cit. on pp. 7–9).

[51] K. S. Novoselov et al. “Unconventional quantum Hall effect and Berry’s phase of 2π in bilayer graphene”. In: *Nature Physics* 2 (2006), pp. 177–180 (cit. on pp. 8, 98).

[52] Jeroen B. Oostinga et al. “Gate-induced insulating state in bilayer graphene devices”. In: *Nat Mater* 7 (2008), pp. 151–157 (cit. on pp. 8, 9).

[53] Andrea F. Young and Leonid S. Levitov. “Capacitance of graphene bilayer as a probe of layer-specific properties”. In: *Phys. Rev. B* 84 (2011), p. 085441 (cit. on pp. 9, 16, 18).

[54] Jun Yong Khoo, Alberto F. Morpurgo, and Leonid Levitov. “On-Demand Spin–Orbit Interaction from Which-Layer Tunability in Bilayer Graphene”. In: *Nano Letters* 17 (2017), pp. 7003–7008 (cit. on pp. 9, 16, 18, 96).

[55] Taisuke Ohta et al. “Controlling the Electronic Structure of Bilayer Graphene”. In: *Science* 313 (2006), pp. 951–954 (cit. on p. 9).

[56] J.D. Jackson. *Classical electrodynamics.* Wiley, 1962 (cit. on p. 9).

[57] Denis Kochan, Susanne Irmer, and Jaroslav Fabian. “Model spin-orbit coupling Hamiltonians for graphene systems”. In: *Phys. Rev. B* 95 (2017), p. 165415 (cit. on pp. 9–13, 16).

[58] Susanne Irmer. “Theoretical investigations of orbital and spin-orbital effects in functionalized graphene”. PhD thesis. Universität Regensburg, 2018 (cit. on pp. 9, 13).

[59] C. L. Kane and E. J. Mele. “Quantum Spin Hall Effect in Graphene”. In: *Phys. Rev. Lett.* 95 (2005), p. 226801 (cit. on pp. 10–12).

[60] Cheng-Cheng Liu, Hua Jiang, and Yugui Yao. “Low-energy effective Hamiltonian involving spin-orbit coupling in silicene and two-dimensional germanium and tin”. In: *Phys. Rev. B* 84 (2011), p. 195430 (cit. on p. 10).

[61] Martin Gmitra et al. “Trivial and inverted Dirac bands and the emergence of quantum spin Hall states in graphene on transition-metal dichalcogenides”. In: *Phys. Rev. B* 93 (2016), p. 155104 (cit. on pp. 11, 14, 15, 34, 81, 89, 90, 92).

[62] M. Gmitra et al. “Band-structure topologies of graphene: Spin-orbit coupling effects from first principles”. In: *Phys. Rev. B* 80 (2009), p. 235431 (cit. on pp. 11, 12, 91).

[63] Hongki Min et al. “Intrinsic and Rashba spin-orbit interactions in graphene sheets”. In: *Phys. Rev. B* 74 (2006), p. 165310 (cit. on pp. 12, 91).

[64] Daniel Huertas-Hernando, F. Guinea, and Arne Brataas. “Spin-orbit coupling in curved graphene, fullerenes, nanotubes, and nanotube caps”. In: *Phys. Rev. B* 74 (2006), p. 155426 (cit. on p. 12).

[65] Yugui Yao et al. “Spin-orbit gap of graphene: First-principles calculations”. In: *Phys. Rev. B* 75 (2007), p. 041401 (cit. on p. 12).

[66] J. C. Boettger and S. B. Trickey. “First-principles calculation of the spin-orbit splitting in graphene”. In: *Phys. Rev. B* 75 (2007), p. 121402 (cit. on p. 12).

[67] Sergej Konschuh, Martin Gmitra, and Jaroslav Fabian. “Tight-binding theory of the spin-orbit coupling in graphene”. In: *Phys. Rev. B* 82 (2010), p. 245412 (cit. on p. 12).

[68] J. Sichau et al. “Resonance Microwave Measurements of an Intrinsic Spin-Orbit Coupling Gap in Graphene: A Possible Indication of a Topological State”. In: *Phys. Rev. Lett.* 122 (2019), p. 046403 (cit. on p. 12).

[69] S. Konschuh et al. “Theory of spin-orbit coupling in bilayer graphene”. In: *Phys. Rev. B* 85 (2012), p. 115423 (cit. on p. 13).

[70] T. P. Kaloni et al. “Quantum spin Hall states in graphene interacting with WS2 or WSe2”. In: *Applied Physics Letters* 105, 233112 (2014), pp. - (cit. on pp. 14, 81).

[71] L. Wang et al. “One-Dimensional Electrical Contact to a Two-Dimensional Material”. In: *Science* 342 (2013), pp. 614–617 (cit. on pp. 14, 82).

[72] A. K. Geim and I. V. Grigorieva. “Van der Waals heterostructures”. In: *Nature* 499 (2013), pp. 419–425 (cit. on p. 14).

[73] A. V. Kretinin et al. “Electronic Properties of Graphene Encapsulated with Different Two-Dimensional Atomic Crystals”. In: *Nano Letters* 14 (2014), pp. 3270–3276 (cit. on p. 14).

[74] J. Y. Tan et al. “Electronic transport in graphene-based heterostructures”. In: *Applied Physics Letters* 104, 183504 (2014), p. 183504 (cit. on p. 14).

[75] L. Banszerus et al. “Extraordinary high room-temperature carrier mobility in graphene-WSe_2 heterostructures”. In: *arxiv*: 1909.09523 (2019) (cit. on p. 14).

[76] L Banszerus et al. “Identifying suitable substrates for high-quality graphene-based heterostructures”. In: *2D Materials* 4 (2017), p. 025030 (cit. on pp. 14, 24).

[77] Julia Gusakova et al. “Electronic Properties of Bulk and Monolayer TMDs: Theoretical Study Within DFT Framework (GVJ-2e Method)”. In: *physica status solidi (a)* 214 (2017), p. 1700218 (cit. on p. 14).

[78] Andor Kormányos et al. “k·ptheory for two-dimensional transition metal dichalcogenide semiconductors”. In: *2D Materials* 2 (2015), p. 022001 (cit. on pp. 14, 15).

[79] Tobias Frank et al. “Protected Pseudohelical Edge States in $\mathbb{Z}_2$-Trivial Proximitized Graphene”. In: *Phys. Rev. Lett.* 120 (2018), p. 156402 (cit. on p. 15).

[80] Tobias Frank. “Ab initio studies of extrinsic spin-orbit coupling effects in graphene and quantum Monte Carlo simulations of phosphorene”. PhD thesis. Universitat Regensburg, 2018 (cit. on p. 15).

[81] Abdulrhman M. Alsharari, Mahmoud M. Asmar, and Sergio E. Ulloa. “Mass inversion in graphene by proximity to dichalcogenide monolayer”. In: *Phys. Rev. B* 94 (2016), p. 241106 (cit. on pp. 15, 92).

[82] A. Mreńca-Kolasińska, B. Rzeszotarski, and B. Szafran. “Spin-active devices based on graphene/WSe_2 heterostructures”. In: *Phys. Rev. B* 98 (2018), p. 045406 (cit. on p. 15).

[83] Aron W. Cummings et al. “Giant Spin Lifetime Anisotropy in Graphene Induced by Proximity Effects”. In: *Phys. Rev. Lett.* 119 (2017), p. 206601 (cit. on pp. 16, 40, 41, 44, 45, 81, 103).

[84] Abdulrhman M. Alsharari, Mahmoud M. Asmar, and Sergio E. Ulloa. “Topological phases and twisting of graphene on a dichalcogenide monolayer”. In: *Phys. Rev. B* 98 (2018), p. 195129 (cit. on p. 16).

[85] Yang Li and Mikito Koshino. “Twist-angle dependence of the proximity spin-orbit coupling in graphene on transition-metal dichalcogenides”. In: *Phys. Rev. B* 99 (2019), p. 075438 (cit. on pp. 16, 90).

[86] Alessandro David et al. “Induced spin-orbit coupling in twisted graphene–transition metal dichalcogenide heterobilayers: Twistronics meets spintronics”. In: *Phys. Rev. B* 100 (2019), p. 085412 (cit. on pp. 16, 90).

[87] J. O. Island et al. “Spin-orbit-driven band inversion in bilayer graphene by the van der Waals proximity effect”. In: *Nature* 571 (2019), pp. 85–89 (cit. on pp. 17, 103).

[88] N.W. Ashcroft and N.D. Mermin. *Solid state physics.* Science: Physics. Saunders College, 1976 (cit. on p. 19).

[89] S. Hunklinger. *Festkörperphysik.* De Gruyter Studium. De Gruyter, 2014 (cit. on p. 19).

[90] K. S. Novoselov et al. “Two-dimensional gas of massless Dirac fermions in graphene”. In: *Nature* 438 (2005), pp. 197–200 (cit. on p. 19).

[91] C.W.J. Beenakker and H. van Houten. “Quantum Transport in Semiconductor Nanostructures”. In: *Semiconductor Heterostructures and Nanostructures.* Ed. by Henry Ehrenreich and David Turnbull. Vol. 44. Solid State Physics. Academic Press, 1991, pp. 1–228 (cit. on pp. 19, 27–29, 84, 100, 101).

[92] Kentaro Nomura and A. H. MacDonald. “Quantum Transport of Massless Dirac Fermions”. In: *Phys. Rev. Lett.* 98 (2007), p. 076602 (cit. on p. 19).

[93] Nuno J. G. Couto et al. “Random Strain Fluctuations as Dominant Disorder Source for High-Quality On-Substrate Graphene Devices”. In: *Phys. Rev. X* 4 (2014), p. 041019 (cit. on pp. 19, 20, 24, 30).

[94] M. Monteverde et al. “Transport and Elastic Scattering Times as Probes of the Nature of Impurity Scattering in Single-Layer and Bilayer Graphene”. In: *Phys. Rev. Lett.* 104 (2010), p. 126801 (cit. on p. 19).

[95] Martin Drienovsky et al. “Commensurability Oscillations in One-Dimensional Graphene Superlattices”. In: *Phys. Rev. Lett.* 121 (2018), p. 026806 (cit. on pp. 19, 101).

[96] J. Martin et al. “Observation of electron-hole puddles in graphene using a scanning single-electron transistor”. In: *Nat Phys* 4 (2008), pp. 144–148 (cit. on p. 20).

[97] Yuanbo Zhang et al. “Origin of spatial charge inhomogeneity in graphene”. In: *Nature Physics* 5 (2009), pp. 722–726 (cit. on p. 20).

[98] Nuno J. G. Couto. “Quantum transport through graphene and topological insulators”. PhD thesis. UNIVERSIT´E DE GEN‘EVE, 2014 (cit. on pp. 20, 30).

[99] Andrea C. Ferrari et al. “Raman spectroscopy of amorphous, nanostructured, diamond-like carbon, and nanodiamond”. In: *Philosophical Transactions of the Royal Society of London. Series A: Mathematical, Physical and Engineering Sciences* 362 (2004), pp. 2477–2512 (cit. on p. 21).

[100] F. Tuinstra and J. L. Koenig. “Raman Spectrum of Graphite”. In: *The Journal of Chemical Physics* 53 (1970), pp. 1126–1130 (cit. on pp. 21, 23, 24).

[101] Andrea C. Ferrari. “Raman spectroscopy of graphene and graphite: Disorder, electron-phonon coupling, doping and nonadiabatic effects”. In: *Solid State Communications* 143 (2007), pp. 47–57 (cit. on pp. 22, 55).

[102] L.M. Malard et al. “Raman spectroscopy in graphene”. In: *Physics Reports* 473 (2009), pp. 51–87 (cit. on p. 22).

[103] Andrea C. Ferrari and Denis M. Basko. “Raman spectroscopy as a versatile tool for studying the properties of graphene”. In: *Nat Nano* 8 (2013), pp. 235–246 (cit. on pp. 22–24).

[104] C. Casiraghi et al. “Raman Spectroscopy of Graphene Edges”. In: *Nano Lett.* 9 (2009), pp. 1433–1441 (cit. on p. 22).

[105] C. Casiraghi et al. “Raman fingerprint of charged impurities in graphene”. In: *Applied Physics Letters* 91 (2007), p. 233108 (cit. on p. 22).

[106] Cinzia Casiraghi. “Probing disorder and charged impurities in graphene by Raman spectroscopy”. In: *physica status solidi (RRL) – Rapid Research Letters* 3 (2009), pp. 175–177 (cit. on pp. 23, 24).

[107] A. C. Ferrari et al. “Raman Spectrum of Graphene and Graphene Layers”. In: *Phys. Rev. Lett.* 97 (2006), p. 187401 (cit. on p. 23).

[108] S. Heydrich et al. “Scanning Raman spectroscopy of graphene antidot lattices: Evidence for systematic p-type doping”. In: *Applied Physics Letters* 97 (2010), p. 043113 (cit. on p. 24).

[109] C. Neumann et al. “Raman spectroscopy as probe of nanometre-scale strain variations in graphene”. In: *Nature Communications* 6 (2015), p. 8429 (cit. on p. 24).

[110] Christoph Neumann et al. “Line shape of the Raman 2D peak of graphene in van der Waals heterostructures”. In: *physica status solidi (b)* 253 (2016), pp. 2326–2330 (cit. on p. 24).

[111] L. G. Cancado et al. “Quantifying Defects in Graphene via Raman Spectroscopy at Different Excitation Energies”. In: *Nano Letters* 11 (2011), pp. 3190–3196 (cit. on pp. 24, 25, 55, 59).

[112] Axel Eckmann et al. “Raman study on defective graphene: Effect of the excitation energy, type, and amount of defects”. In: *Phys. Rev. B* 88 (2013), p. 035426 (cit. on pp. 24, 25).

[113] Axel Eckmann et al. “Probing the Nature of Defects in Graphene by Raman Spectroscopy”. In: *Nano Letters* 12 (2012), pp. 3925–3930 (cit. on p. 25).

[114] B. L. Altshuler et al. “Magnetoresistance and Hall effect in a disordered two-dimensional electron gas”. In: *Phys. Rev. B* 22 (1980), pp. 5142–5153 (cit. on p. 27).

[115] N. M. R. Peres. “Colloquium: The transport properties of graphene: An introduction”. In: *Rev. Mod. Phys.* 82 (2010), pp. 2673–2700 (cit. on pp. 27–29).

[116] Gerd Bergmann. “Physical interpretation of weak localization: A time-of-flight experiment with conduction electrons”. In: *Phys. Rev. B* 28 (1983), pp. 2914–2920 (cit. on p. 28).

[117] Gerd Bergmann. “Weak localization in thin films: a time-of-flight experiment with conduction electrons”. In: *Physics Reports* 107 (1984), pp. 1–58 (cit. on p. 28).

[118] Thomas Ihn. *Semiconductor Nanostructures: Quantum states and electronic transport.* Oxford University Press, 2009 (cit. on pp. 28, 29, 32, 99).

[119] Supriyo Datta. *Electronic Transport in Mesoscopic Systems.* Cambridge Studies in Semiconductor Physics and Microelectronic Engineering. Cambridge University Press, 1995 (cit. on p. 28).

[120] B L Altshuler, A G Aronov, and D E Khmelnitsky. “Effects of electron-electron collisions with small energy transfers on quantum localisation”. In: *Journal of Physics C: Solid State Physics* 15 (1982), pp. 7367–7386 (cit. on p. 28).

[121] B. N. Narozhny, Gábor Zala, and I. L. Aleiner. “Interaction corrections at intermediate temperatures: Dephasing time”. In: *Phys. Rev. B* 65 (2002), p. 180202 (cit. on p. 28).

[122] Y. Aharonov and D. Bohm. “Significance of Electromagnetic Potentials in the Quantum Theory”. In: *Phys. Rev.* 115 (1959), pp. 485–491 (cit. on p. 28).

[123] G. P. Mikitik and Yu. V. Sharlai. “The Berry phase in graphene and graphite multilayers”. In: *Low Temperature Physics* 34 (2008), pp. 794–800 (cit. on p. 29).

[124] Tsuneya Ando, Takeshi Nakanishi, and Riichiro Saito. “Berry’s Phase and Absence of Back Scattering in Carbon Nanotubes”. In: *Journal of the Physical Society of Japan* 67 (1998), pp. 2857–2862 (cit. on p. 29).

[125] Hidekatsu Suzuura and Tsuneya Ando. “Crossover from Symplectic to Orthogonal Class in a Two-Dimensional Honeycomb Lattice”. In: *Phys. Rev. Lett.* 89 (2002), p. 266603 (cit. on pp. 29, 30).

[126] D. V. Khveshchenko. “Electron Localization Properties in Graphene”. In: *Phys. Rev. Lett.* 97 (2006), p. 036802 (cit. on pp. 29, 30).

[127] A. F. Morpurgo and F. Guinea. “Intervalley Scattering, Long-Range Disorder, and Effective Time-Reversal Symmetry Breaking in Graphene”. In: *Phys. Rev. Lett.* 97 (2006), p. 196804 (cit. on pp. 29, 30).

[128] E. McCann et al. “Weak-Localization Magnetoresistance and Valley Symmetry in Graphene”. In: *Phys. Rev. Lett.* 97 (2006), p. 146805 (cit. on p. 30).

[129] K. Kechedzhi et al. “Weak localization in monolayer and bilayer graphene”. In: *The European Physical Journal Special Topics* 148 (2007), pp. 39–54 (cit. on p. 30).

[130] S. V. Morozov et al. “Strong Suppression of Weak Localization in Graphene”. In: *Phys. Rev. Lett.* 97 (2006), p. 016801 (cit. on p. 30).

[131] F. V. Tikhonenko et al. “Weak Localization in Graphene Flakes”. In: *Phys. Rev. Lett.* 100 (2008), p. 056802 (cit. on pp. 30, 31, 60).

[132] Xiaosong Wu et al. “Weak Antilocalization in Epitaxial Graphene: Evidence for Chiral Electrons”. In: *Phys. Rev. Lett.* 98 (2007), p. 136801 (cit. on p. 30).

[133] F.V. Tikhonenko et al. “The effect of inter-valley scattering on weak localisation in graphene”. In: *Physica E: Low-dimensional Systems and Nanostructures* 40 (2008). 17th International Conference on Electronic Properties of Two-Dimensional Systems, pp. 1364–1366 (cit. on p. 30).

[134] J Eroms and D Weiss. “Weak localization and transport gap in graphene antidot lattices”. In: *New Journal of Physics* 11 (2009), p. 095021 (cit. on p. 30).

[135] Florian Oberhuber et al. “Weak localization and Raman study of anisotropically etched graphene antidots”. In: *Applied Physics Letters* 103, 143111 (2013), pp. - (cit. on p. 30).

[136] Florian Oberhuber. “Untersuchung kristallographisch definierter Graphen- Ränder”. PhD thesis. Universität Regensburg, 2015 (cit. on p. 30).

[137] Bernard R. Matis et al. “Giant negative magnetoresistance and a transition from strong to weak localization in hydrogenated graphene”. In: *Phys. Rev. B* 85 (2012), p. 195437 (cit. on p. 30).

[138] Ruwantha Jayasingha et al. “In Situ Study of Hydrogenation of Graphene and New Phases of Localization between Metal–Insulator Transitions”. In: *Nano Letters* 13 (2013), pp. 5098–5105 (cit. on p. 30).

[139] Bernard R. Matis, Brian H. Houston, and Jeffrey W. Baldwin. “Evidence for Spin Glass Ordering Near the Weak to Strong Localization Transition in Hydrogenated Graphene”. In: *ACS Nano* 10 (2016), pp. 4857–4862 (cit. on p. 30).

[140] Dong-Keun Ki et al. “Inelastic scattering in a monolayer graphene sheet: A weak-localization study”. In: *Phys. Rev. B* 78 (2008), p. 125409 (cit. on pp. 31, 60, 61).

[141] M. B. Lundeberg et al. “Defect-Mediated Spin Relaxation and Dephasing in Graphene”. In: *Phys. Rev. Lett.* 110 (2013), p. 156601 (cit. on pp. 31, 84, 85).

[142] Mark B. Lundeberg and Joshua A. Folk. “Rippled Graphene in an In-Plane Magnetic Field: Effects of a Random Vector Potential”. In: *Phys. Rev. Lett.* 105 (2010), p. 146804 (cit. on pp. 31, 34).

[143] F. V. Tikhonenko et al. “Transition between Electron Localization and Antilocalization in Graphene”. In: *Phys. Rev. Lett.* 103 (2009), p. 226801 (cit. on pp. 31, 86).

[144] K. Kechedzhi et al. “Influence of Trigonal Warping on Interference Effects in Bilayer Graphene”. In: *Phys. Rev. Lett.* 98 (2007), p. 176806 (cit. on p. 32).

[145] R. V. Gorbachev et al. “Weak Localization in Bilayer Graphene”. In: *Phys. Rev. Lett.* 98 (2007), p. 176805 (cit. on p. 32).

[146] S. Engels et al. “Limitations to Carrier Mobility and Phase-Coherent Transport in Bilayer Graphene”. In: *Phys. Rev. Lett.* 113 (2014), p. 126801 (cit. on p. 32).

[147] Shinobu Hikami, Anatoly I. Larkin, and Yosuke Nagaoka. “Spin-Orbit Interaction and Magnetoresistance in the Two Dimensional Random System”. In: *Progress of Theoretical Physics* 63 (1980), pp. 707–710 (cit. on p. 32).

[148] G. Bergmann. “Weak anti-localization—An experimental proof for the destructive interference of rotated spin 12”. In: *Solid State Communications* 42 (1982), pp. 815–817 (cit. on p. 32).

[149] Edward McCann and Vladimir I. Fal’ko. “$z \to -z$ Symmetry of Spin-Orbit Coupling and Weak Localization in Graphene”. In: *Phys. Rev. Lett.* 108 (2012), p. 166606 (cit. on pp. 32, 86).

[150] Stefan Ilić, Julia S. Meyer, and Manuel Houzet. “Weak localization in transition metal dichalcogenide monolayers and their heterostructures with graphene”. In: *Phys. Rev. B* 99 (2019), p. 205407 (cit. on p. 33).

[151] Tobias Völkl et al. “Magnetotransport in heterostructures of transition metal dichalcogenides and graphene”. In: *Phys. Rev. B* 96 (2017), p. 125405 (cit. on pp. 33, 81, 82).

[152] Zhe Wang et al. “Strong interface-induced spin-orbit interaction in graphene on WS2”. In: *Nat Commun* 6 (2015), pp. – (cit. on pp. 33, 86).

[153] Zhe Wang et al. “Origin and Magnitude of ‘Designer’ Spin-Orbit Interaction in Graphene on Semiconducting Transition Metal Dichalcogenides”. In: *Phys. Rev. X* 6 (2016), p. 041020 (cit. on pp. 33, 34, 85–87, 99).

[154] Bowen Yang et al. “Tunable spin–orbit coupling and symmetry-protected edge states in graphene/WS2”. In: *2D Materials* 3 (2016), p. 031012 (cit. on pp. 34, 86, 92).

[155] Bowen Yang et al. “Strong electron-hole symmetric Rashba spin-orbit coupling in graphene/monolayer transition metal dichalcogenide heterostructures”. In: *Phys. Rev. B* 96 (2017), p. 041409 (cit. on pp. 34, 87).

[156] Bowen Yang. “Spin-Orbit Coupling in Graphene and Transition Metal Dichalcogenides”. PhD thesis. UC Riverside, 2017 (cit. on p. 34).

[157] T. Wakamura et al. “Strong Anisotropic Spin-Orbit Interaction Induced in Graphene by Monolayer WS_2”. In: *Phys. Rev. Lett.* 120 (2018), p. 106802 (cit. on pp. 34, 90).

[158] T. Wakamura et al. “Spin-orbit interaction induced in graphene by transition metal dichalcogenides”. In: *Phys. Rev. B* 99 (2019), p. 245402 (cit. on pp. 34, 87, 90).

[159] Amir Muhammad Afzal et al. “Gate Modulation of the Spin-orbit Interaction in Bilayer Graphene Encapsulated by WS2 films”. In: *Scientific Reports* 8 (2018), p. 3412 (cit. on p. 34).

[160] Simon Zihlmann et al. “Large spin relaxation anisotropy and valley-Zeeman spin-orbit coupling in WSe_2/graphene/h-BN heterostructures”. In: *Phys. Rev. B* 97 (2018), p. 075434 (cit. on pp. 34, 86, 87, 90, 92, 103).

[161] Simon Zihlmann. “Spin and charge relaxation in graphene”. PhD thesis. Universität Basel, 2018 (cit. on pp. 34, 50).

[162] Jaroslav Fabian and Igor Zutic. “The standard model of spin injection”. In: *arxiv*: 0903.2500 (2009) (cit. on p. 34).

[163] A. K. Patra et al. “Dynamic spin injection into chemical vapor deposited graphene”. In: *Applied Physics Letters* 101 (2012), p. 162407 (cit. on p. 34).

[164] Zhenyao Tang et al. “Dynamically generated pure spin current in single-layer graphene”. In: *Phys. Rev. B* 87 (2013), p. 140401 (cit. on pp. 34, 35).

[165] S. Dushenko et al. “Gate-Tunable Spin-Charge Conversion and the Role of Spin-Orbit Interaction in Graphene”. In: *Phys. Rev. Lett.* 116 (2016), p. 166102 (cit. on p. 34).

[166] David Indolese et al. “Wideband and On-Chip Excitation for Dynamical Spin Injection into Graphene”. In: *Phys. Rev. Applied* 10 (2018), p. 044053 (cit. on pp. 34, 35).

[167] Yunqiu Kelly Luo et al. “Opto-Valleytronic Spin Injection in Monolayer MoS2/ Few-Layer Graphene Hybrid Spin Valves”. In: *Nano Lett.* 17 (2017), pp. 3877–3883 (cit. on p. 34).

[168] Ahmet Avsar et al. “Optospintronics in Graphene via Proximity Coupling”. In: *ACS Nano* 11 (2017), pp. 11678–11686 (cit. on p. 34).

[169] Williams Fernando Savero Torres et al. “Spin precession and the spin Hall effect in graphene/Pt nanostructures”. In: *2D Materials* 4 (2017), p. 041008 (cit. on p. 35).

[170] Nevill Francis Mott and Ralph Howard Fowler. “The electrical conductivity of transition metals”. In: *Proceedings of the Royal Society of London. Series A - Mathematical and Physical Sciences* 153 (1936), pp. 699–717 (cit. on p. 35).

[171] A. Fert and I. A. Campbell. “Two-Current Conduction in Nickel”. In: *Phys. Rev. Lett.* 21 (1968), pp. 1190–1192 (cit. on p. 35).

[172] S. Blundell. *Magnetism in Condensed Matter*. Oxford Master Series in Condensed Matter Physics. OUP Oxford, 2001 (cit. on p. 35).

[173] Jagadeesh S. Moodera, Joaquim Nassar, and George Mathon. “Spin-Tunneling in Ferromagnetic Junctions”. In: *Annual Review of Materials Science* 29 (1999), pp. 381–432 (cit. on p. 36).

[174] H. C. Torrey. “Bloch Equations with Diffusion Terms”. In: *Phys. Rev.* 104 (1956), pp. 563–565 (cit. on p. 37).

[175] C. Józsa et al. “Linear scaling between momentum and spin scattering in graphene”. In: *Phys. Rev. B* 80 (2009), p. 241403 (cit. on p. 37).

[176] T. Maassen et al. “Comparison between charge and spin transport in few-layer graphene”. In: *Phys. Rev. B* 83 (2011), p. 115410 (cit. on p. 37).

[177] Thomas Maassen. “Electron Spin Transport in Graphene–Based Devices”. PhD thesis. Rijksuniversiteit Groningen, 2013 (cit. on p. 37).

[178] Mark Johnson and R. H. Silsbee. “Interfacial charge-spin coupling: Injection and detection of spin magnetization in metals”. In: *Phys. Rev. Lett.* 55 (1985), pp. 1790–1793 (cit. on p. 37).

[179] Mariusz Ciorga et al. “Electrical spin injection and detection in lateral all-semiconductor devices”. In: *Physical Review B* 79 (2009), p. 165321 (cit. on p. 38).

[180] R. J. Elliott. “Theory of the Effect of Spin-Orbit Coupling on Magnetic Resonance in Some Semiconductors”. In: *Phys. Rev.* 96 (1954), pp. 266–279 (cit. on p. 39).

[181] Y. Yafet. “g Factors and Spin-Lattice Relaxation of Conduction Electrons”. In: *Solid State Physics 14*. Academic Press, 1963, pp. 1–98 (cit. on p. 39).

[182] D. Huertas-Hernando, F. Guinea, and Arne Brataas. “Spin-Orbit-Mediated Spin Relaxation in Graphene”. In: *Phys. Rev. Lett.* 103 (2009), p. 146801 (cit. on pp. 40, 41, 43).

[183] H. Ochoa, A. H. Castro Neto, and F. Guinea. “Elliot-Yafet Mechanism in Graphene”. In: *Phys. Rev. Lett.* 108 (2012), p. 206808 (cit. on p. 40).

[184] Dmytro Pesin and Allan H. MacDonald. “Spintronics and pseudospintronics in graphene and topological insulators”. In: *Nat Mater* 11 (2012), pp. 409–416 (cit. on p. 40).

[185] M.I. Dyakonov and V.I. Perel. “Spin orientation of electrons associated with the interband absorption of light in semiconductors”. In: *Soviet Physics JETP* 33 (1971), p. 1053 (cit. on pp. 40, 41).

[186] Oleg V. Yazyev and Lothar Helm. “Defect-induced magnetism in graphene”. In: *Phys. Rev. B* 75 (2007), p. 125408 (cit. on p. 41).

[187] Bruno Uchoa et al. “Localized Magnetic States in Graphene”. In: *Phys. Rev. Lett.* 101 (2008), p. 026805 (cit. on p. 41).

[188] Felix Yndurain. “Effect of hole doping on the magnetism of point defects in graphene: A theoretical study”. In: *Phys. Rev. B* 90 (2014), p. 245420 (cit. on p. 41).

[189] Kathleen M. McCreary et al. “Magnetic Moment Formation in Graphene Detected by Scattering of Pure Spin Currents”. In: *Phys. Rev. Lett.* 109 (2012), p. 186604 (cit. on p. 41).

[190] Héctor González-Herrero et al. “Atomic-scale control of graphene magnetism by using hydrogen atoms”. In: *Science* 352 (2016), pp. 437–441 (cit. on pp. 41, 69).

[191] T. O. Wehling et al. “Resonant Scattering by Realistic Impurities in Graphene”. In: *Phys. Rev. Lett.* 105 (2010), p. 056802 (cit. on pp. 41, 61, 76).

[192] Susanne Irmer et al. “Resonant scattering due to adatoms in graphene: Top, bridge, and hollow positions”. In: *Phys. Rev. B* 97 (2018), p. 075417 (cit. on pp. 41, 76).

[193] Denis Kochan et al. “Resonant Scattering by Magnetic Impurities as a Model for Spin Relaxation in Bilayer Graphene”. In: *Phys. Rev. Lett.* 115 (19 2015), p. 196601 (cit. on pp. 41, 43).

[194] M. Wojtaszek et al. “Absence of hyperfine effects in ^{13}C-graphene spin-valve devices”. In: *Phys. Rev. B* 89 (2014), p. 035417 (cit. on p. 42).

[195] Dinh Van Tuan et al. “Pseudospin-driven spin relaxation mechanism in graphene”. In: *Nature Physics* 10 (2014), p. 857 (cit. on p. 42).

[196] Nikolaos Tombros et al. “Electronic spin transport and spin precession in single graphene layers at room temperature”. In: *Nature* 448 (2007), pp. 571–574 (cit. on p. 42).

[197] T. Maassen et al. “Contact-induced spin relaxation in Hanle spin precession measurements”. In: *Phys. Rev. B* 86 (23 2012), p. 235408 (cit. on p. 42).

[198] H. Idzuchi, A. Fert, and Y. Otani. “Revisiting the measurement of the spin relaxation time in graphene-based devices”. In: *Phys. Rev. B* 91 (2015), p. 241407 (cit. on p. 42).

[199] Gordon Stecklein et al. “Contact-Induced Spin Relaxation in Graphene Nonlocal Spin Valves”. In: *Phys. Rev. Applied* 6 (2016), p. 054015 (cit. on p. 43).

[200] F. Volmer et al. “Role of MgO barriers for spin and charge transport in Co/MgO/ graphene nonlocal spin-valve devices”. In: *Phys. Rev. B* 88 (2013), p. 161405 (cit. on pp. 43, 44).

[201] F. Volmer et al. “Suppression of contact-induced spin dephasing in graphene/ MgO/Co spin-valve devices by successive oxygen treatments”. In: *Phys. Rev. B* 90 (2014), p. 165403 (cit. on p. 43).

[202] Frank Volmer et al. “Contact-induced charge contributions to non-local spin transport measurements in Co/MgO/graphene devices”. In: *2D Materials* 2 (2015), p. 024001 (cit. on pp. 43, 68, 73).

[203] Frank Volmer. “Einfluss der Oxid-Barriere auf den Spin- und Ladungstransport in Graphen/MgO/Co-Strukturen”. PhD thesis. RWTH Aachen, 2015 (cit. on p. 43).

[204] Wei Han et al. “Tunneling Spin Injection into Single Layer Graphene”. In: *Phys. Rev. Lett.* 105 (2010), p. 167202 (cit. on p. 43).

[205] Wei Han and R. K. Kawakami. “Spin Relaxation in Single-Layer and Bilayer Graphene”. In: *Phys. Rev. Lett.* 107 (2011), p. 047207 (cit. on p. 43).

[206] Wei Han et al. “Spin transport and relaxation in graphene”. In: *Journal of Magnetism and Magnetic Materials* 324 (2012), pp. 369–381 (cit. on p. 43).

[207] Marc Drögeler et al. “Nanosecond Spin Lifetimes in Single- and Few-Layer Graphene–hBN Heterostructures at Room Temperature”. In: *Nano Letters* 14 (2014), pp. 6050–6055 (cit. on p. 43).

[208] Ahmet Avsar et al. “Electronic spin transport in dual-gated bilayer graphene”. In: *NPG Asia Mater* 8 (2016), p. 274 (cit. on p. 43).

[209] M. H. D. Guimarães et al. “Controlling Spin Relaxation in Hexagonal BN-Encapsulated Graphene with a Transverse Electric Field”. In: *Phys. Rev. Lett.* 113 (2014), p. 086602 (cit. on p. 43).

[210] Simranjeet Singh et al. "Nanosecond spin relaxation times in single layer graphene spin valves with hexagonal boron nitride tunnel barriers". In: *Applied Physics Letters* 109, 122411 (2016), pp. - (cit. on p. 43).

[211] Johannes Christian Leutenantsmeyer et al. "Efficient spin injection into graphene through trilayer hBN tunnel barriers". In: *Journal of Applied Physics* 124 (2018), p. 194301 (cit. on p. 43).

[212] Dinh Van Tuan et al. "Spin dynamics and relaxation in graphene dictated by electron-hole puddles". In: *Scientific Reports* 6 (2016), p. 21046 (cit. on p. 43).

[213] Dorri Halbertal et al. "Imaging resonant dissipation from individual atomic defects in graphene". In: *Science* 358 (2017), pp. 1303–1306 (cit. on pp. 43, 78).

[214] N. Tombros et al. "Anisotropic Spin Relaxation in Graphene". In: *Phys. Rev. Lett.* 101 (2008), p. 046601 (cit. on p. 43).

[215] Bart Raes et al. "Determination of the spin-lifetime anisotropy in graphene using oblique spin precession". In: *Nat Commun* 7 (2016), pp. – (cit. on p. 43).

[216] Sebastian Ringer et al. "Measuring anisotropic spin relaxation in graphene". In: *Phys. Rev. B* 97 (2018), p. 205439 (cit. on pp. 43, 64, 68).

[217] Jan Bundesmann et al. "Theory of spin-orbit-induced spin relaxation in functionalized graphene". In: *Phys. Rev. B* 92 (2015), p. 081403 (cit. on p. 44).

[218] M. Wojtaszek et al. "Enhancement of spin relaxation time in hydrogenated graphene spin-valve devices". In: *Phys. Rev. B* 87 (2013), p. 081402 (cit. on pp. 44, 69).

[219] Magdalena Wojtaszek. "Exploring magnetism in graphene by electronic charge and spin transport". PhD thesis. University of Groningen, 2014 (cit. on p. 44).

[220] Talieh S. Ghiasi et al. "Large Proximity-Induced Spin Lifetime Anisotropy in Transition-Metal Dichalcogenide/Graphene Heterostructures". In: *Nano Letters* 17 (2017), pp. 7528–7532 (cit. on pp. 45, 81, 87, 92).

[221] L. Antonio Benítez et al. "Strongly anisotropic spin relaxation in graphene-transition metal dichalcogenide heterostructures at room temperature". In: *Nature Physics* (2017), pp. – (cit. on pp. 45, 81, 87, 92).

[222] L. Antonio Benítez et al. "Investigating the spin-orbit interaction in van der Waals heterostructures by means of the spin relaxation anisotropy". In: *APL Materials* 7 (2019), p. 120701 (cit. on p. 45).

[223] S. Omar, B. N. Madhushankar, and B. J. van Wees. "Large spin-relaxation anisotropy in bilayer-graphene/WS_2 heterostructures". In: *Phys. Rev. B* 100 (2019), p. 155415 (cit. on p. 45).

[224] M.I. Dyakonov and V.I. Perel. "Current-induced spin orientation of electrons in semiconductors". In: *Physics Letters A* 35 (1971), pp. 459–460 (cit. on p. 46).

[225] Jairo Sinova et al. "Spin Hall effects". In: *Rev. Mod. Phys.* 87 (2015), pp. 1213–1260 (cit. on pp. 46–48).

[226] M.I. Dyakonov. *Spin Physics in Semiconductors.* Springer Series in Solid-State Sciences. Springer, 2008 (cit. on pp. 46, 47, 90).

[227] Aires Ferreira et al. “Extrinsic Spin Hall Effect Induced by Resonant Skew Scattering in Graphene”. In: *Phys. Rev. Lett.* 112 (2014), p. 066601 (cit. on pp. 46, 49, 58).

[228] Nevill Francis Mott and Niels Henrik David Bohr. “The scattering of fast electrons by atomic nuclei”. In: *Proceedings of the Royal Society of London. Series A, Containing Papers of a Mathematical and Physical Character* 124 (1929), pp. 425–442 (cit. on p. 46).

[229] Jayakumar Balakrishnan et al. “Colossal enhancement of spin-orbit coupling in weakly hydrogenated graphene”. In: *Nat Phys* 9 (2013), pp. 284–287 (cit. on pp. 47–49, 53, 54, 57, 61, 69, 79).

[230] E. M. Hankiewicz et al. “Manifestation of the spin Hall effect through charge-transport in the mesoscopic regime”. In: *Phys. Rev. B* 70 (2004), p. 241301 (cit. on p. 47).

[231] D. A. Abanin et al. “Nonlocal charge transport mediated by spin diffusion in the spin Hall effect regime”. In: *Phys. Rev. B* 79 (2009), p. 035304 (cit. on pp. 48, 49).

[232] Jayakumar Balakrishnan et al. “Giant spin Hall effect in graphene grown by chemical vapour deposition”. In: *Nat Commun* 5 (2014), p. 4748 (cit. on p. 49).

[233] Ahmet Avsar et al. “Enhanced spin–orbit coupling in dilute fluorinated graphene”. In: *2D Materials* 2 (2015), p. 044009 (cit. on p. 49).

[234] A. Avsar et al. “Spin-orbit proximity effect in graphene”. In: *Nat Commun* 5 (2014), p. 4875 (cit. on p. 49).

[235] Jungmin Park et al. “Gate-dependent spin Hall induced nonlocal resistance and the symmetry of spin-orbit scattering in Au-clustered graphene”. In: *Phys. Rev. B* 95 (2017), p. 245414 (cit. on p. 50).

[236] S. O. Valenzuela and M. Tinkham. “Direct electronic measurement of the spin Hall effect”. In: *Nature* 442 (2006), pp. 176–179 (cit. on pp. 50, 70).

[237] C. K. Safeer et al. “Room-Temperature Spin Hall Effect in Graphene/MoS2 van der Waals Heterostructures”. In: *Nano Letters* 19 (2019), pp. 1074–1082 (cit. on p. 50).

[238] Talieh S. Ghiasi et al. “Charge-to-Spin Conversion by the Rashba-Edelstein Effect in Two-Dimensional van der Waals Heterostructures up to Room Temperature”. In: *Nano Lett.* 19 (2019), pp. 5959–5966 (cit. on p. 51).

[239] L. Antonio Benítez et al. “Tunable room-temperature spin galvanic and spin Hall effects in van der Waals heterostructures”. In: *Nature Materials* 19 (2020), pp. 170–175 (cit. on p. 51).

[240] Jose H. Garcia, Aron W. Cummings, and Stephan Roche. “Spin Hall Effect and Weak Antilocalization in Graphene/Transition Metal Dichalcogenide Heterostructures”. In: *Nano Letters* 17 (2017), pp. 5078–5083 (cit. on p. 51).

[241] Manuel Offidani et al. “Optimal Charge-to-Spin Conversion in Graphene on Transition-Metal Dichalcogenides”. In: *Phys. Rev. Lett.* 119 (2017), p. 196801 (cit. on p. 51).

[242] Franz Vilsmeier. “Studies on the Hydrogenation of Graphene”. Bachelor’s Thesis. University of Regensburg, 2015 (cit. on p. 53).

[243] Thomas Ebnet. “Optimierung der Wasserstoffanlagerung an Graphen”. Bachelor’s Thesis. University of Regensburg, 2015 (cit. on p. 53).

[244] Tobias Völkl et al. “Absence of a giant spin Hall effect in plasma-hydrogenated graphene”. In: *Phys. Rev. B* 99 (2019), p. 085401 (cit. on pp. 53, 74).

[245] Sunmin Ryu et al. “Reversible Basal Plane Hydrogenation of Graphene”. In: *Nano Letters* 8 (2008), pp. 4597–4602 (cit. on pp. 54, 57, 58).

[246] M. Wojtaszek et al. “A road to hydrogenating graphene by a reactive ion etching plasma”. In: *Journal of Applied Physics* 110 (2011), p. 063715 (cit. on pp. 54, 59).

[247] E. Zion et al. “Effect of annealing on Raman spectra of monolayer graphene samples gradually disordered by ion irradiation”. In: *Journal of Applied Physics* 121 (2017), p. 114301 (cit. on p. 55).

[248] Zhiqiang Luo et al. “Thickness-Dependent Reversible Hydrogenation of Graphene Layers”. In: *ACS Nano* 3 (2009), pp. 1781–1788 (cit. on p. 55).

[249] Alessio Paris et al. “Kinetic Isotope Effect in the Hydrogenation and Deuteration of Graphene”. In: *Advanced Functional Materials* 23 (2013), pp. 1628–1635 (cit. on pp. 55, 56).

[250] Thomas Zecho et al. “Adsorption of hydrogen and deuterium atoms on the (0001) graphite surface”. In: *The Journal of Chemical Physics* 117 (2002), pp. 8486–8492 (cit. on pp. 55, 56).

[251] A. Nourbakhsh et al. “Tuning the Fermi Level of SiO2-Supported Single-Layer Graphene by Thermal Annealing”. In: *J. Phys. Chem. C* 114 (2010), pp. 6894–6900 (cit. on p. 57).

[252] Yung-Chang Lin et al. “Graphene Annealing: How Clean Can It Be?” In: *Nano Letters* 12 (2012), pp. 414–419 (cit. on p. 57).

[253] Sung Oh Woo and Winfried Teizer. “The effect of electron induced hydrogenation of graphene on its electrical transport properties”. In: *Applied Physics Letters* 103 (2013), p. 041603 (cit. on p. 57).

[254] Jyoti Katoch et al. “Uncovering the dominant scatterer in graphene sheets on SiO_2”. In: *Phys. Rev. B* 82 (2010), p. 081417 (cit. on p. 58).

[255] Bernard R. Matis et al. “Surface Doping and Band Gap Tunability in Hydrogenated Graphene”. In: *ACS Nano* 6 (2012), pp. 17–22 (cit. on p. 58).

[256] Z. H. Ni et al. “On Resonant Scatterers As a Factor Limiting Carrier Mobility in Graphene”. In: *Nano Letters* 10 (2010), pp. 3868–3872 (cit. on p. 59).

[257] Bernard R. Matis, Brian H. Houston, and Jeffrey W. Baldwin. “Low-energy resonant scattering from hydrogen impurities in graphene”. In: *Phys. Rev. B* 88 (2013), p. 085441 (cit. on pp. 61, 69).

[258] G. Mihajlović et al. “Negative Nonlocal Resistance in Mesoscopic Gold Hall Bars: Absence of the Giant Spin Hall Effect”. In: *Phys. Rev. Lett.* 103 (2009), p. 166601 (cit. on p. 62).

[259] Sebastian Ringer et al. “Spin field-effect transistor action via tunable polarization of the spin injection in a Co/MgO/graphene contact”. In: *Applied Physics Letters* 113 (2018), p. 132403 (cit. on pp. 64, 68).

[260] Sebastian Ringer. “Anisotropic spinrelaxation in graphene”. PhD thesis. Universität Regensburg, 2018 (cit. on pp. 64, 67, 68).

[261] T.R. McGuire and R.I. Potter. “Anisotropic magnetoresistance in ferromagnetic 3d alloys”. In: *IEEE Transactions on Magnetics* 11 (1975), pp. 1018–1038 (cit. on p. 65).

[262] M. Getzlaff. *Fundamentals of Magnetism.* Springer, 2007 (cit. on pp. 65, 66).

[263] Mark Johnson and R. H. Silsbee. “Calculation of nonlocal baseline resistance in a quasi-one-dimensional wire”. In: *Phys. Rev. B* 76 (2007), p. 153107 (cit. on p. 67).

[264] F. L. Bakker et al. “Interplay of Peltier and Seebeck Effects in Nanoscale Nonlocal Spin Valves”. In: *Phys. Rev. Lett.* 105 (2010), p. 136601 (cit. on p. 67).

[265] David Soriano et al. “Spin transport in hydrogenated graphene”. In: *2D Materials* 2 (2015), p. 022002 (cit. on p. 69).

[266] Sadamichi Maekawa et al. *Spin Current.* Oxford University Press, 2012 (cit. on p. 70).

[267] Daniel Schiermeier. “Simulationen zum Spintransport mit räumlich veränderlichen Parametern”. Bachelors Thesis. University of Regensburg, 2018 (cit. on p. 73).

[268] Di Xiao, Wang Yao, and Qian Niu. “Valley-Contrasting Physics in Graphene: Magnetic Moment and Topological Transport”. In: *Phys. Rev. Lett.* 99 (2007), p. 236809 (cit. on p. 75).

[269] Di Xiao, Ming-Che Chang, and Qian Niu. “Berry phase effects on electronic properties”. In: *Rev. Mod. Phys.* 82 (2010), pp. 1959–2007 (cit. on p. 75).

[270] Michael Beconcini, Fabio Taddei, and Marco Polini. “Nonlocal topological valley transport at large valley Hall angles”. In: *Phys. Rev. B* 94 (2016), p. 121408 (cit. on pp. 75, 76).

[271] Mahmoud M. Asmar and Sergio E. Ulloa. “Symmetry-breaking effects on spin and electronic transport in graphene”. In: *Phys. Rev. B* 91 (2015), p. 165407 (cit. on p. 75).

[272] Xian-Peng Zhang, Chunli Huang, and Miguel A Cazalilla. “Valley Hall effect and nonlocal transport in strained graphene”. In: *2D Materials* 4.2 (2017), p. 024007 (cit. on p. 75).

[273] R. V. Gorbachev et al. “Detecting topological currents in graphene superlattices”. In: *Science* 346 (2014), pp. 448–451 (cit. on p. 75).

[274] C. R. Woods et al. “Commensurate-incommensurate transition in graphene on hexagonal boron nitride”. In: *Nature Physics* 10 (2014), pp. 451–456 (cit. on p. 75).

[275] Mengqiao Sui et al. “Gate-tunable topological valley transport in bilayer graphene”. In: *Nature Physics* 11 (2015), pp. 1027–1031 (cit. on p. 75).

[276] Y. Shimazaki et al. “Generation and detection of pure valley current by electrically induced Berry curvature in bilayer graphene”. In: *Nature Physics* 11 (2015), p. 1032 (cit. on p. 75).

[277] Jyoti Katoch et al. “Transport Spectroscopy of Sublattice-Resolved Resonant Scattering in Hydrogen-Doped Bilayer Graphene”. In: *Phys. Rev. Lett.* 121 (2018), p. 136801 (cit. on p. 75).

[278] Mahmoud M. Asmar and Sergio E. Ulloa. “Minimal geometry for valley filtering in graphene”. In: *Phys. Rev. B* 96 (2017), p. 201407 (cit. on p. 76).

[279] Xian-Peng Zhang, Chunli Huang, and Miguel A. Cazalilla. “Control of spin diffusion and suppression of the Hanle oscillation by the coexistence of spin and valley Hall effects in Dirac materials”. In: *Phys. Rev. B* 99 (2019), p. 245106 (cit. on p. 76).

[280] Jie Pan et al. “Berry Curvature and Nonlocal Transport Characteristics of Antidot Graphene”. In: *Phys. Rev. X* 7 (2017), p. 031043 (cit. on pp. 76–78).

[281] A. Cresti et al. “Charge, spin and valley Hall effects in disordered graphene”. In: *Rivista del nuovo cimento* 39 (2016), p. 587 (cit. on p. 78).

[282] J. Tworzydło et al. “Sub-Poissonian Shot Noise in Graphene”. In: *Phys. Rev. Lett.* 96 (2006), p. 246802 (cit. on p. 78).

[283] D. A. Abanin et al. “Giant Spin-Hall Effect Induced by the Zeeman Interaction in Graphene”. In: *Phys. Rev. Lett.* 107 (2011), p. 096601 (cit. on p. 78).

[284] D. A. Abanin et al. “Giant Nonlocality Near the Dirac Point in Graphene”. In: *Science* 332 (2011), pp. 328–330 (cit. on p. 78).

[285] Julien Renard, Matthias Studer, and Joshua A. Folk. “Origins of Nonlocality Near the Neutrality Point in Graphene”. In: *Phys. Rev. Lett.* 112 (2014), p. 116601 (cit. on p. 78).

[286] J. R. Williams et al. “Gate-controlled guiding of electrons in graphene”. In: *Nature Nanotechnology* 6 (2011), pp. 222–225 (cit. on p. 78).

[287] Peter Rickhaus et al. “Guiding of Electrons in a Few-Mode Ballistic Graphene Channel”. In: *Nano Lett.* 15 (2015), pp. 5819–5825 (cit. on p. 78).

[288] A. Marguerite et al. “Imaging work and dissipation in the quantum Hall state in graphene”. In: *Nature* 575 (2019), pp. 628–633 (cit. on p. 78).

[289] Tobias Völkl. “Spin-Hall Effect in Weakly Hydrogenated Graphene”. Master’s Thesis. Universität Regensburg, 2014 (cit. on p. 79).

[290] Julia Amann. “Gate-Modulation der Spin-Bahn-Kopplung in Graphen-WSe2-Heterostrukturen”. Master’s Thesis. University of Regensburg, 2020 (cit. on pp. 81, 83, 93).

[291] Kenji Watanabe, Takashi Taniguchi, and Hisao Kanda. “Direct-bandgap properties and evidence for ultraviolet lasing of hexagonal boron nitride single crystal”. In: *Nature Materials* 3 (2004), pp. 404–409 (cit. on p. 82).

[292] S. J. Haigh et al. “Cross-sectional imaging of individual layers and buried interfaces of graphene-based heterostructures and superlattices”. In: *Nature Materials* 11 (2012), pp. 764–767 (cit. on p. 82).

[293] Martin Drienovský. “Übergittereffekte in eindimensional moduliertem Graphen”. PhD thesis. University of Regensburg, 2018 (cit. on p. 82).

[294] Filippo Pizzocchero et al. “The hot pick-up technique for batch assembly of van der Waals heterostructures”. In: *Nature Communications* 7 (2016), p. 11894 (cit. on p. 83).

[295] Jangyup Son et al. “Atomically precise graphene etch stops for three dimensional integrated systems from two dimensional material heterostructures”. In: *Nature Communications* 9 (2018), p. 3988 (cit. on p. 83).

[296] Atindra Nath Pal, Vidya Kochat, and Arindam Ghosh. “Direct Observation of Valley Hybridization and Universal Symmetry of Graphene with Mesoscopic Conductance Fluctuations”. In: *Phys. Rev. Lett.* 109 (2012), p. 196601 (cit. on p. 84).

[297] P. A. Lee, A. Douglas Stone, and H. Fukuyama. “Universal conductance fluctuations in metals: Effects of finite temperature, interactions, and magnetic field”. In: *Phys. Rev. B* 35 (1987), pp. 1039–1070 (cit. on p. 85).

[298] M. B. Lundeberg, J. Renard, and J. A. Folk. “Conductance fluctuations in quasi-two-dimensional systems: A practical view”. In: *Phys. Rev. B* 86 (2012), p. 205413 (cit. on p. 85).

[299] Guillaume Froehlicher, Etienne Lorchat, and Stéphane Berciaud. “Charge Versus Energy Transfer in Atomically Thin Graphene-Transition Metal Dichalcogenide van der Waals Heterostructures”. In: *Phys. Rev. X* 8 (2018), p. 011007 (cit. on p. 86).

[300] Young-Jun Yu et al. “Tuning the Graphene Work Function by Electric Field Effect”. In: *Nano Lett.* 9 (2009), pp. 3430–3434 (cit. on p. 92).

[301] Kyounghwan Kim et al. “Band Alignment in WSe2–Graphene Heterostructures”. In: *ACS Nano* 9 (2015), pp. 4527–4532 (cit. on p. 93).

[302] Tobias Rockinger. “Magnetotransport-Messungen an Graphen/Wolframdisulfid-Heterostrukturen”. Master’s Thesis. Universität Regensburg, 2017 (cit. on p. 98).

[303] A. F. Young et al. “Spin and valley quantum Hall ferromagnetism in graphene”. In: *Nat Phys* 8 (2012), pp. 550–556 (cit. on p. 99).

[304] Jason Alicea and Matthew P. A. Fisher. “Graphene integer quantum Hall effect in the ferromagnetic and paramagnetic regimes”. In: *Phys. Rev. B* 74 (2006), p. 075422 (cit. on p. 99).

[305] M. O. Goerbig. “Electronic properties of graphene in a strong magnetic field”. In: *Rev. Mod. Phys.* 83 (2011), pp. 1193–1243 (cit. on p. 99).

[306] Tarik P. Cysne et al. “Quantum Hall effect in graphene with interface-induced spin-orbit coupling”. In: *Phys. Rev. B* 97 (2018), p. 085413 (cit. on p. 99).

[307] Ya-Wen Chuang et al. “Landau levels of bilayer graphene in a WSe_2/bilayer graphene van der Waals heterostructure”. In: *Phys. Rev. B* 100 (2019), p. 195402 (cit. on p. 99).

[308] Satoru Masubuchi et al. “Boundary Scattering in Ballistic Graphene”. In: *Phys. Rev. Lett.* 109 (2012), p. 036601 (cit. on p. 101).

[309] T. J. Thornton et al. “Boundary scattering in quantum wires”. In: *Phys. Rev. Lett.* 63 (1989), pp. 2128–2131 (cit. on p. 101).

[310] E. Ditlefsen and J. Lothe. “Theory of Size Effects in Electrical Conductivity”. In: *Philosophical Magazine* 14 (1966), pp. 759–773 (cit. on p. 101).

[311] Hengyi Xu, Thomas Heinzel, and Igor V. Zozoulenko. “Geometric magnetoconductance dips by edge roughness in graphene nanoribbons”. In: *Europhysics Letters* 97 (2012), p. 28008 (cit. on p. 101).

[312] Bowen Yang et al. “Effect of Distance on Photoluminescence Quenching and Proximity-Induced Spin–Orbit Coupling in Graphene/WSe2 Heterostructures”. In: *Nano Letters* 18 (2018), pp. 3580–3585 (cit. on p. 103).

[313] Weijie Zhao et al. “Evolution of Electronic Structure in Atomically Thin Sheets of WS_2 and WSe_2”. In: *ACS Nano* 7 (2013), pp. 791–797 (cit. on p. 103).

[314] Amin Azizi et al. “Freestanding van der Waals Heterostructures of Graphene and Transition Metal Dichalcogenides”. In: *ACS Nano* 9 (2015), pp. 4882–4890 (cit. on p. 103).

[315] Boris Grbić et al. “Strong spin-orbit interactions and weak antilocalization in carbon-doped p-type GaAs/$Al_xGa_{1-x}As$ heterostructures”. In: *Phys. Rev. B* 77 (2008), p. 125312 (cit. on p. 103).

[316] Klaus Zollner et al. “Purely interfacial and highly tunable spin-orbit torque operating field-effect transistor in graphene doubly proximitized by two-dimensional magnet $Cr_2Ge_2Te_6$ and WS_2”. In: *arxiv*: 1910.08072 (2019) (cit. on p. 106).

Fabrication details and recipes

Exfoliation of different materials

- Dicing of p^{++}-doped Si with 285 nm thick SiO_2 waver into 10 mm×9 mm sized chips or using prepared 4.5 mm×4.5 mm substrates with 5 nm Cr +60 nm Au thick coordinate system
- Standard cleaning of the Si chips with acetone, isopropanol and oxygen plasma (power 30 %, 5 min)
- Micromechanical exfoliation of natural graphite, hBN or WSe_2 onto the chips
- Identification of suitable flakes under an optical microscope

Hydrogenated graphene in H-bar design

Graphene hydrogenation

- Employing RIE chamber with hydrogen pressure of 40 mTorr, 30sccm gas flow and 2 W power for 20 s

Definition of the sample structure with RIE

- Spincoating chips with PMMA 950 k 5 % at 3000 rpm for 5 s and 6000 rpm for 30 s
- Bakeout of resist on hotplate at 150 °C for 4 min
- EBL with Auriga SEM: EHT=30 kV, aperture 20 µm, area dose 280 $\mu C/cm^2$
- Developing the resist in MIBK/isopropanol (1:3) for 90 s and isopropanol for 30 s
- Employing RIE with oxygen pressure of 30 mTorr, 20 sccm gas flow and 20 W power for 60 s
- Removing Etchmask in acetone and isopropanol

Deposition of metal contacts

- Spincoating chips with PMMA 200 k 9 % at 3000 rpm for 5 s and 6000 rpm for 30 s
- Bakeout of resist on hotplate at 150 °C for 4 min
- Spincoating chips with PMMA 950 k 5 % at 3000 rpm for 5 s and 6000 rpm for 30 s
- Bakeout of resist on hotplate at 150 °C for 4 min
- EBL with Auriga SEM: EHT=30 kV, aperture 20 µm, area dose 440 µC/cm^2 for fine wiring; aperture 120 µm, area dose 440 µC/cm^2 for coarse wiring
- Developing the resist in MIBK/isopropanol (1:3) for 90 s and isopropanol for 30 s
- Deposition of 0.5 nm Cr and 60 nm Au in Univex B
- Lift-off in acetone at T=60 °C for 1 hour

Hydrogenated graphene in spin injection design

Graphene hydrogenation

- Employing RIE chamber with hydrogen pressure of 40 mTorr, 30sccm gas flow and 2 W power for 20 s

Deposition of spin selective contacts

- Spincoating chips with CSAR 9 % at 3000 rpm for 5 s and 4000 rpm for 30 s
- Bakeout of resist on hotplate at 150 °C for 1 min
- EBL with Auriga SEM: EHT=30 kV, aperture 20 µm, area dose 180 µC/cm^2
- Developing the resist in AR 600-546 for 80 s and isopropanol for 40 s
- Insert samples into load lock of UHV-system, transfer to main chamber after load lock pressure reached $p < 10^{-7}$ mbar
- Store samples in main chamber for at least two days to allow the samples to degas
- Evaporation of Ti with closed shutter to reach base pressure of main chamber at $p \approx 10^{-10}$ mbar
- Deposition of “36 Hz” MgO, 50 nm Co and 10 nm Au
- Lift-off in AR 600-71 for 10 min at room temperature

Deposition of metal contacts

- Spincoating chips with PMMA 200 k 9 % at 3000 rpm for 5 s and 6000 rpm for 30 s
- Bakeout of resist on hotplate at 150 °C for 4 min
- Spincoating chips with PMMA 950 k 5 % at 3000 rpm for 5 s and 6000 rpm for 30 s
- Bakeout of resist on hotplate at 150 °C for 4 min
- EBL with Auriga SEM: EHT=30 kV, aperture 20 µm, area dose 440 $\mu C/cm^2$ for fine wiring; aperture 120 µm, area dose 440 $\mu C/cm^2$ for coarse wiring
- Developing the resist in MIBK/isopropanol (1:3) for 90 s and isopropanol for 30 s
- Deposition of 0.5 nm Cr and 80 nm Au in Univex B
- Lift-off in acetone at T=60 °C for 1 hour

Definition of the sample structure with RIE

- Spincoating chips with PMMA 950 k 5 % at 3000 rpm for 5 s and 6000 rpm for 30 s
- Bakeout of resist on hotplate at 150 °C for 4 min
- EBL with Auriga SEM: EHT=30 kV, aperture 20 µm, area dose 280 $\mu C/cm^2$
- Developing the resist in MIBK/isopropanol (1:3) for 90 s and isopropanol for 30 s
- Employing RIE with oxygen pressure of 30 mTorr, 20 sccm gas flow and 20 W power for 60 s
- Removing Etchmask in acetone and isopropanol

Graphene/WSe_2 heterostructures

Fabrication of heterostructures

- Dicing of p^{++}-doped Si with 90 nm thick SiO_2 waver into 20 mm×20 mm sized chips
- Spincoating these chips with PPC 15 % in Acetone at 1500 rpm for 50 s
- Bakeout of resist on hotplate at 150 °C for 8 min
- Exfoliating the top layer of the finished structure onto the PPC resist

- Identification of suitable flakes under an optical microscope
- Stamping a hole into a piece of sticky tape and placing the tape with the hole over the identified flake
- Peeling off the tape leaves a thin PPC membrane with the exfoliated flake
- Placing tape onto a metal ring glued onto a glass slide
- Inserting the glass slide face down into a transfer stage over the target chip with an exfoliated flake of the second material
- Aligning the two flakes and bringing them into contact
- Upon retrieving the PPC film, the created heterostructure sticks to the PPC
- Repeating the process to pick up a third material or placing the PPC film onto a traget chip with prepatterned coordinate system
- Placing the glass slide with the PPC film and the traget chip sticking to it onto a 150 °C hotplate allows to peel off the Si chip with the PPC film intact
- Removing the PPC in chloroform for 24 h and isopropanol for 30 s
- Annnealing of heterostrucutres for 1 h at 320 °C in vacuum and 1 h at 320 °C in forming gas

Definition of the sample structure with RIE

- Spincoating chips with PMMA 950 k 5 % at 3000 rpm for 5 s and 6000 rpm for 30 s
- Bakeout of resist on hotplate at 150 °C for 5 min
- EBL with Auriga SEM: EHT=30 kV, aperture 20 µm, area dose 280 $\mu C/cm^2$
- Developing the resist in MIBK/isopropanol (1:3) for 90 s and isopropanol for 30 s
- Employing RIE with CHF_3/O_2 pressure of 55 mTorr, 40/6 sccm gas flow and 35 W power for 30 s-2 min, depending on the heterostructure thickness
- Removing Etchmask in acetone and isopropanol

Deposition of metal contacts

- Spincoating chips with PMMA 200 k 9 % at 3000 rpm for 5 s and 6000 rpm for 30 s
- Bakeout of resist on hotplate at 150 °C for 5 min
- Spincoating chips with PMMA 950 k 5 % at 3000 rpm for 5 s and 6000 rpm for 30 s
- Bakeout of resist on hotplate at 150 °C for 5 min
- EBL with Auriga SEM: EHT=30 kV, aperture 20 µm, area dose 440 $\mu C/cm^2$ for fine wiring; aperture 120 µm, area dose 440 $\mu C/cm^2$ for coarse wiring
- Developing the resist in MIBK/isopropanol (1:3) for 90 s and isopropanol for 30 s
- Employing RIE etching chamber with oxygen pressure of 30 mTorr, 20 sccm gas flow and 20 W power for 30 s,
- Deposition of 5 nm Cr and 80 nm Au in Univex B
- Lift-off in acetone at T=60 °C for 1 hour

Topgate Fabrication

- Atomic layer deposition of 10 nm thick Al_2O_3 at 120 °C
- Spincoating chips with PMMA 200 k 9 % at 3000 rpm for 5 s and 6000 rpm for 30 s
- Bakeout of resist on hotplate at 150 °C for 5 min
- Spincoating chips with PMMA 950 k 5 % at 3000 rpm for 5 s and 6000 rpm for 30 s
- Bakeout of resist on hotplate at 150 °C for 5 min
- EBL with Auriga SEM: EHT=30 kV, aperture 20 µm, area dose 440 $\mu C/cm^2$ for fine wiring; aperture 120 µm, area dose 440 $\mu C/cm^2$ for coarse wiring
- Developing the resist in MIBK/isopropanol (1:3) for 90 s and isopropanol for 30 s
- Deposition of 5 nm Cr and 80 nm Au in Univex B
- Lift-off in acetone at T=60 °C for 1 hour

Acknowledgments

An dieser Stelle möchte ich all jenen danken, die zum Erfolg dieser Arbeit maßgeblich beigetragen haben:

- Jonathan Eroms, der mir die Arbeit an diesem Thema ermöglicht hat, für die hervorragende Betreuung. Für zahlreiche Gespräche, Erklärungen und Diskussionen, für die Freiheit eigene Ideen zu verfolgen und für die Untestützung bei Themen, die über das Gelingen der Doktorarbeit hinausgingen.

- Dieter Weiss, für die Aufnahme am Lehrstuhl, die Schaffung der ausgezeichneten Rahmenbedingungen und hilfreiche Anmerkungen zur Interpretation der Messergebnisse, Vorträgen und Veröffentlichungen.

- Jaroslav Fabian für die Zweitkorrektur dieser Arbeit.

- Denis Kochan, Tobias Frank und Jaroslav Fabian für Diskussionen zur Interpretation der Messergebnisse und der Zusammenarbeit bei der Veröffentlichung der Ergebnisse.

- Philip Nagler, Tobias Korn und Christian Schüller für die Durchführung der Ramanmessungen und Diskussionen zur Interpretation der Ergebnisse.

- Christoph Strunk und seiner Arbeitsgruppe für das Erlauben der ausgiebigen Benutzung der UHV-Aufdampfanlage und Thomas Haller für die Instandhaltung dieser Anlage und der schnellen Reparatur von auftretenden Problemen.

- Meinen Masterstudenten Tobias Rockinger und Julia Amann für die reibungslose Zusammenarbeit, deren Ergebnisse essentiell für diese Arbeit waren.

- Meinen Bachelorstudenten Franz Vilsmeier und Thomas Ebnet für die Charakterisierung des Wasserstoffplasma-Anlagerungsprozesses.

- Martin Drienovsky und Robin Huber, die mir die Transferprozesse gezeigt haben, die die Grundlage für die Fabrikation der van der Waals Heterostrukturen in dieser Arbeit darstellen.

- Sebastian Ringer für die erfolgreiche Zusammenarbeit bei der Entwicklung der Spininjektionskontakte.

- Allen Mitgliedern des Lehrstuhl Weiss, insbesondere der Graphen-Arbeitsgruppe, für die tolle Zusammenarbeit, den produktiven Wissensaustausch und die angenehme Arbeitsatmosphäre.

- Meinen Bürokollegen Tobias Preis, Johannes Ziegler und Wolfgang Himmler für die lockere Atmosphäre, gegenseitige Hilfe bei fachlichen Problemen und zahlreiche witzige Diskussionen.
- Michael Weigl, Daniel Pahl, Uli Gürster, Cornelia Linz und Thomas Haller, die mir bei technischen Fragen und Problemen immer zur Seite standen.
- Claudia Rahm und Elke Haushalter für die hervorragende und nette organisatorische Betreuung.
- Den Mitarbeitern der Heliumausgabe, der Mechanikwerkstatt und der Elektronikwerkstatt.
- Für das Korrekturlesen dieser Arbeit: Roland Völkl, Tobias Preis, Julia Amann und Katharina Meichelböck.
- Meinen Geschwistern Roland Völkl und Christina Hösl für ihre Unterstützung.